RADIO FREQUENCY STUDIES OF SURFACE RESISTANCE AND CRITICAL MAGNETIC FIELD OF TYPE I AND TYPE II SUPERCONDUCTORS

Thesis by

Tadashi Yogi

In Partial Fulfillment of the Requirements

for the Degree of

Doctor of Philosophy

California Institute of Technology

Pasadena, California

1977

(Submitted August 2, 1976)

To Aiko and Our Parents

ACKNOWLEDGMENT

I would like to express my sincere appreciation to the following persons who have made this work possible directly and/or indirectly.

Professor J. E. Mercereau for his patient advice and interest throughout the course of this research.

Drs. G. J. Dick and K. W. Shepard for their guidance and suggestions of the problem areas that were essential.

Dr. H. Notarys who was always there, ready to help in the laboratory and who even took the awesome task of correcting my uncorrectable English. I cannot thank him enough.

All the graduate student colleagues in the laboratory who created the "low temperature" atmosphere; particularly, J. R. Delayen and H. C. Yen whose cooperation in various phases of this study is greatly appreciated.

Mr. S. Santantonio for his willing help in the construction of the necessary equipment.

Mr. E. P. Boud for his technical assistance in the laboratory.

Ms. G. Kusudo for her general assistance in the office.

I am also thankful to Prof. L. B. Slichter (U.C.L.A.) for his patience and understanding while I was writing this dissertation.

I am grateful to the California Institute of Technology for financial assistance throughout my graduate study.

The fine typing of this dissertation is due to Mrs. R. Stratton.

Last, but not least, I would like to thank my wife for her patience and encouragement throughout the course of my graduate study.

ABSTRACT

The surface resistance and the critical magnetic field of lead electroplated on copper were studied at 205 MHz in a half-wave coaxial resonator. The observed surface resistance at a low field level below 4.2°K could be well described by the BCS surface resistance with the addition of a temperature independent residual resistance. The available experimental data suggest that the major fraction of the residual resistance in the present experiment was due to the presence of an oxide layer on the surface. At higher magnetic field levels the surface resistance was found to be enhanced due to surface imperfections.

The attainable rf critical magnetic field between 2.2°K and T_c of lead was found to be limited not by the thermodynamic critical field but rather by the superheating field predicted by the one-dimensional Ginzburg-Landau theory. The observed rf critical field was very close to the expected superheating field, particularly in the higher reduced temperature range, but showed somewhat stronger temperature dependence than the expected superheating field in the lower reduced temperature range.

The rf critical magnetic field was also studied at 90 MHz for pure tin and indium, and for a series of SnIn and InBi alloys spanning both type I and type II superconductivity. The samples were spherical with typical diameters of 1-2 mm and a helical resonator was used to generate the rf magnetic field in the measurement. The results of pure samples of tin and indium showed that a vortex-like nucleation of the normal phase was responsible for the superconducting-to-normal phase

transition in the rf field at temperatures up to about 0.98-0.99 T_c, where the ideal superheating limit was being reached. The results of the alloy samples showed that the attainable rf critical fields near T_c were well described by the superheating field predicted by the one-dimensional GL theory in both the type I and type II regimes. The measurement was also made at 300 MHz resulting in no significant change in the rf critical field. Thus it was inferred that the nucleation time of the normal phase, once the critical field was reached, was small compared with the rf period in this frequency range.

TABLE OF CONTENTS

Chapter I

INTRODUCTION

The superconducting state is a macroscopic quantum state characterized in a superconductor by the absence of dc electrical resistance (the perfect conductivity) and the expulsion of magnetic flux (the Meissner effect). Since its discovery in 1911 by Onnes (O2), the description of superconductivity remained largely phenomenological until a successful microscopic theory was formulated by Bardeen, Cooper and Shrieffer (henceforth BCS) in 1957 (B1). Coupled with advances in general experimental technique and materials processing, the last two decades have seen a rapid growth in both the basic understanding of the phenomenon and the applications ranging from small scale devices such as Josephson junctions to large scale generation of intense magnetic fields.

The field of high power rf superconductivity was initiated in the early 1960s with the proposal to use superconducting rf resonators for the acceleration of charged particles (B3,S3). Since then extensive investigations have been carried out in various laboratories in order to generate intense rf fields at frequencies ranging from 100 MHz up to 10 GHz. (Throughout this dissertation the radio frequency is loosely defined as this frequency range.)

As a result of these efforts, notably at Stanford and Karlsruhe (Germany), it has become possible to attain rf magnetic fields up to 1600 gauss (S4) and rf electric fields up to 70 MV/m (T2) in microwave resonant cavities. Also surface resistances which are 3 to 5 orders

of magnitude smaller than that of copper at 4°K are commonly achieved. This means, for example, that surface rf magnetic fields of 1,000 gauss can be sustained by a superconductor with a power dissipation per unit area of 0.03 watts/cm^2 as compared to 30 watts/cm^2 for a copper at the same temperature ($\sim$ 1 GHz).

The materials that have been considered and investigated in detail so far are two elemental superconductors, niobium and lead. They have been chosen because of their high transition temperatures (9.46°K for Nb and 7.18°K for Pb) and high critical magnetic fields (1944 gauss for Nb and 803 gauss for Pb at 0°K). More recently, studies have been started of high field alloys such as Nb_3Sn (P10). The material parameters that play an important role in the high power rf application are:

Transition temperature (T_c)

Surface impedance ($Z = R + iX$)

RF critical magnetic field (H_c^{rf})

Work function (ϕ, field emission property)

Thermal conductivity.

This dissertation deals with two of the above, the surface resistance and the rf critical magnetic field, with considerably more emphasis on the latter, in the frequency range between 90 and 300 MHz. Most of this work, particularly Chapter 3, is a direct product of the superconducting heavy ion accelerator project which began in 1969 at Caltech. The content of each chapter is as follows:

Chapter 2 reviews and summarizes the previous experimental results and the relevant theories of surface resistance and rf critical magnetic field.

Chapter 3 deals with the measurement of the surface resistance and the rf critical magnetic field of superconducting lead electroplated on copper at 205 MHz.

Chapter 4 reports the measurement of the rf critical fields of small samples of Sn, In, SnIn and InBi alloys.

The system of units used in this dissertation is the rationalized MKS units except where specified.

Chapter II

A REVIEW OF THE PAST EXPERIMENTAL RESULTS AND THE RELEVANT THEORIES

In the rf application of superconductivity, two of the most important parameters are the surface resistance, since it determines the power dissipation, and the critical magnetic field, since it limits the attainable electromagnetic field level. Because of their practical importance they have been studied quite extensively in terms of both experiment and theory. In the following sections the results of previous experiments and the pertinent theories are reviewed separately for the surface resistance and the critical magnetic field.

2.1 The Superconducting Surface Resistance

A brief historical survey is presented starting from the surface resistance of an ordinary metal, and leading up to the temperature dependence of the superconducting surface resistance based on the microscopic theory of superconductivity. The residual (non-superconducting) processes which, at low temperatures, give rise to an effective surface resistance are also discussed.

2.1.1 Surface Resistance of Normal Metals at Low Temperature

The response of a metal to an applied electromagnetic field is described by a surface impedance Z defined by

$$Z = R + iX = E_{||} / H_{||} \Big|_{surface} \tag{2.1}$$

where $E_{||}$ and $H_{||}$ are respectively the component of electric and magnetic field parallel to the surface of the conductor. Then the time-averaged

dissipation per unit area of the conductor is given by

$$P_d = \frac{1}{2} R H_{||}^2 \tag{2.2}$$

In a normal metal at room temperature, the Ohm's law

$$J = \sigma E \tag{2.3}$$

holds and the classical surface resistance at radio frequency is given by

$$R_{cl} = (\pi f \mu/\sigma)^{1/2} \tag{2.4}$$

where f is the frequency, μ the permeability of the metal, σ its electrical conductivity. We also have the expression for classical skin depth,

$$\delta_{cl} = (1/\pi f \mu \sigma)^{1/2} \tag{2.5}$$

When sufficiently pure metals are cooled to low temperatures, the number of electron-phonon collisions decreases and the mean free path of electrons, ℓ , increases. As ℓ becomes comparable and larger than the rf skin depth, the point relationship between the current and the electric field no longer holds and a non-local form of Eq. (2.3) must be used to take into account the field variation over the mean free path. This is called the anomalous skin effect and its theory was developed by Reuter and Sondheimer (R2). In the extreme anomalous limit. i.e., $\ell \to \infty$, they obtained the surface resistance for a diffuse reflection of electrons at the surface,

$$R_{\infty} = \left(\frac{\sqrt{3}\,\pi f^2 \mu^2}{4}\right)^{1/3} \left(\frac{\ell}{\sigma}\right)^{1/3} \qquad (2.6)$$

In this limit the surface resistance is independent of mean free path since the ratio ℓ/σ is a constant for a given metal. Measurements made by Chambers (C1) at 1.2 GHz showed that common metals with reasonable purity are in fact in the extreme anomalous limit at temperatures ranging from 14°K to 67°K.

2.1.2 Surface Resistance of Superconductors

Although the electrical resistance of a superconductor against dc transport current vanishes below T_c, the surface resistance in high frequency fields stays finite at a finite temperature. The first theory of superconducting surface resistance was given by H. London (L2) in 1934 based on the two-fluid model of a superconductor. In this picture, the conduction electrons are assumed to be composed of two components, the superfluid and the normal component. In dc fields the superfluid electrons carry all the current, shielding the applied electric field from the normal electrons, so that the electrical resistance vanishes. However, in high frequency fields the shielding of the electric field by supercurrent is incomplete due to the inertia of electrons, and as a result the normal electrons "feel" the electric field leading to dissipation. Since this dissipation is proportional to the density of normal electrons which is unity at T_c and smoothly goes to zero at 0°K, the surface resistance also varies continuously from normal state value at T_c to zero at 0°K. London's theory agreed qualitatively with the experimental results available at that time (L1).

With the realization that the anomalous skin effect was important at low temperatures, Pippard applied the idea to normal electrons and gave an approximate solution to the London equations for surface resistance (P5). In order to obtain better agreement with observed temperature dependence he later made a modification and gave what is now called the semi-empirical Pippard function f(t), which is the temperature dependent part of the surface resistance, as (P4)

$$f(t) = \frac{t^4(1-t^2)}{(1-t^4)} \qquad \text{for} \quad t < 0.9 \qquad (2.7)$$

where $t = T/T_c$ is the reduced temperature. In later years, more precise theory of anomalous skin effect was used by Maxwell et al. (M1) to treat the normal component of two-fluid model. Nevertheless, the overall situation still remained phenomenological until a microscopic theory of superconductivity was established in 1957.

2.1.3 Temperature Dependence of Superconducting Surface Resistance

In 1957 BCS published their theory of superconductivity in which a wide variety of equilibrium superconducting properties was explained. Based on this theory, the surface impedance of superconductors subjected to a weak alternating magnetic field was formulated independently by Mattis and Bardeen (MB) and Abrikosov et al. (A2). In these formulations, the surface impedance was evaluated as a function of temperature, frequency and a set of material parameters. The general expression, however, is quite complex and reduces to explicit forms only in very restricted limits of these parameters.

The first detailed comparison between experimental and theoretical surface impedance at microwave frequencies was made by Turneaure (T3). Based on the formulation by Mattis and Bardeen, he performed a numerical computation of surface impedance. The material parameters needed for the computation were

T_c: Transition temperature

λ_L: London penetration depth

v_F: Fermi velocity

ℓ : Mean free path of electrons in normal state

The values of these parameters were either measured or inferred from the surface resistance measurement in normal state. The results were compared with the surface impedance measurement made on lead and tin at 2.85 and 11.2 GHz. He obtained very good agreement for temperature dependence of the surface resistance. Also, the superconducting gap parameter at 0°K, $\Delta(0)$, which was deduced from the experimental data, agreed well with the values derived from other measurements. The absolute value of the surface resistance, however, did not agree with the theoretical value by a factor of up to ~ 2.

Later, Halbritter (H5) reexamined this problem using more accurate values of the material parameters which had become available in recent years. Using these revised material parameters, he showed that the agreement between theory and experiment, particularly for the absolute magnitude of the surface resistance, was improved for both niobium and lead to within experimental error. It was also established that the following simplified form describes the temperature dependence

of BCS surface resistance for frequencies much smaller than the gap frequency (= Δ/h, 2.6×10^{11} H_z for Pb at 0°K)

$$R_{BCS}(T) = \frac{A'}{T} e^{-\Delta(T)/kT} \quad \text{for} \quad T \lesssim T_c/2 \tag{2.8}$$

where $\Delta(T)$ is the temperature dependent gap parameter, k the Boltzmann constant. The factor A is independent of temperature but depends on the frequency and the material parameters in a non-trivial way so that a numerical computation is necessary to obtain an explicit value. This form was later shown (H1) to be proportional to the number of thermally excited quasi-particles which approximately corresponds to the normal fluid in London's two-fluid model.

In Chapter 3, this form will be used to compare the experimental values of surface resistance of lead at 205 MHz with the result of numerical computation for lead given in the literature.

2.1.4 Residual Surface Resistance

Since the superconducting surface resistance vanishes at 0°K, the quality factor, Q , of a superconducting resonator may be expected to increase indefinitely. In practice, however, this is not the case, and Q tends to a finite value as the temperature is reduced. This is due to other loss mechanisms only some of which are understood. This section describes briefly the residual loss mechanisms that have been studied up to the present.

Dielectric loss: This is due to the presence of an oxide layer on a metal surface and the dissipation is proportional to $\alpha \tan \delta$ where α is the fraction of the electric field in the dielectric and $\tan \delta$

is its loss tangent.

Loss due to trapped flux: When a superconductor is cooled through its transition temperature in the presence of an applied magnetic field, it tends to trap magnetic flux. Since the cores of the trapped flux are normal conducting, they will dissipate energy when rf current is applied to the surface. This effect has been studied in the past for its temperature dependence, frequency dependence, and dependence on applied magnetic fields (H4,P7,P9,V1).

Loss due to acoustic phonon coupling: When an electromagnetic wave is incident on the surface of a superconductor, there is a small but non-negligible tangential component of electric field within the penetration depth of the surface. This electric field acts on the lattice ions thus giving rise to the coupling between the electromagnetic field and the acoustic wave. This coupling is another loss mechanism which puts a lower limit on the surface resistance of a superconductor. Residual losses in some type of cavities were explained by this mechanism (H6). Passow (P8) compared the residual resistance attained experimentally with his theory based on this mechanism and found a good correlation at frequencies between 100 MHz and 10 GHz.

In the present study of low field surface resistance of a lead-plated copper resonator, the residual surface resistance was observed to be present, although every effort was made to avoid surface contamination and oxidations. Estimates for residual resistances due to the above mentioned mechanisms will be given in the discussion of temperature dependence of low field surface resistance (Chapter 3).

2.2 Critical Magnetic Field of Superconductors at Radio Frequencies

In the foregoing sections, we have discussed the superconducting surface resistance which is extremely small compared with the normal state surface resistance. Since the resistance vanishes in the limit of zero frequency we see that the smallness of the superconducting surface resistance at radio frequency is a consequence of the perfect dc conductivity, which is one aspect of the superconducting phenomenon. Another aspect of superconductivity is its ability to exclude an applied magnetic field from a superconducting body up to a certain field* called the thermodynamic critical magnetic field, H_c. This is called the Meissner effect and every superconductor has a well-defined thermodynamic critical field when measured in a static magnetic field.

However, when the magnetic field is changing as a function of time as in the present case at radio frequency, i.e.,

$$H(t) = H^{rf}\sin(\omega t)$$

it is not immediately obvious what will happen when the amplitude of the rf magnetic field becomes comparable in magnitude to the thermodynamic critical field H_c. To put it differently, we ask what is the critical magnetic field at radio frequencies, H_c^{rf}, at which the transition to normal state takes place. Our interest in this quantity is

---

*Strictly speaking, this statement is valid for type I superconductors. For type II superconductors H_c has to be replaced by the lower critical field H_{c1}. These two types are discussed in the following sections.

both practical and basic. That is, in the high power application of superconductivity H_c^{rf} will put the ultimate limit on the magnetic field level that can be achieved. Also, it is physically an interesting phenomenon and the study of rf critical fields may provide new information on the details of superconducting-to-normal phase transition.

With these motivations, the rf critical field was studied for two different systems:

(1) Lead electroplated on copper substrate which formed the walls of a resonant cavity (Chapter 3).

(2) Small samples of tin, indium and their alloys, where the necessary material parameters were well defined and measurable (Chapter 4).

In the following sections we review the basic theories which are important in explaining the present experimental results. Also previous rf measurements for different superconductors are reviewed and summarized toward the end of this chapter for later comparison.

2.2.1 General Remarks on Superconducting State

In 1933 Meissner and Ochsenfeld (M4) found that a magnetic field was expelled from an originally normal sample as it was cooled through its transition temperature. This property of perfect diamagnetism, now known as the Meissner effect, is another basic property of superconductor independent of perfect conductivity. A class of superconductors called type I (to be discussed soon) expels an applied magnetic field up to a critical field H_c which is thermodynamically related to the difference in free energy density g between normal and superconducting states in zero field,

$$g_{no}(T) - g_{so}(T) = \frac{1}{2}\mu_o H_c^2(T) \tag{2.9}$$

which is the so-called condensation energy. Here the subscripts no and so refer to the normal and superconducting states in zero applied field. Empirically, it has been found that $H_c(T)$ is quite well approximated by a parabolic temperature dependence,

$$H_c(T) \simeq H_o(1 - (T/T_c)^2) \tag{2.10}$$

where H_o is the critical field at 0°K and T_c is the transition temperature. The above form agrees with actual critical fields within 3% for most superconductors (L3, p.95).

When a superconductor excludes an applied magnetic field H_a from its body, its free energy density is raised by $\mu_o H_a^2/2$, i.e.,

$$g_n - g_s = \frac{1}{2}\mu_o(H_c^2(T) - H_a^2) \tag{2.11}$$

where it is assumed that the metal in normal state is non-magnetic. Once the free energy difference is given, the entropy difference between normal and superconducting state may be determined as

$$s_n - s_s = -\mu_o H_c(T) \frac{dH_c(T)}{dT} \tag{2.12}$$

and the heat capacity difference as

$$c_n - c_s = \mu_o T\, H_c(T) \frac{d^2H_c(T)}{dT^2} + \mu_o T\left(\frac{dH_c(T)}{dT}\right)^2 \tag{2.13}$$

In the absence of an external magnetic field the superconducting transition at T_c is of the second order, since the entropy is continuous

whereas there is a discontinuity in the heat capacity. In the presence of external magnetic field the transition takes place at a temperature below T_c and it is of the first order since the entropy is discontinuous, and there is a latent heat in the transition given by

$$L = T(s_n - s_s) = -\mu_o T\, H_c(T)\, \frac{dH_c(T)}{dT} \tag{2.14}$$

These results so far have been obtained thermodynamically without any reference to microscopic behavior of superconductors.

In the formal description of superconductivity, it has been found that two characteristic lengths play a basic role. They are the penetration depth and the coherence length.

Penetration depth: In an attempt to describe superconductivity, F. and H. London (L4) proposed two phenomenological equations governing the microscopic electric and magnetic fields. One of the equations which was designed to describe the Meissner effect was

$$\vec{h} = -\lambda_L^2 \frac{\partial \vec{j}_s}{\partial t} \tag{2.15}$$

with $$\lambda_L^2 = m/(\mu_o n_s e^2)$$

where h is the microscopic magnetic field, n_s is the number density of superconducting electrons which contribute the supercurrent density j_s, and m and e are the electron mass and charge respectively. When combined with the Maxwell equation

$$\nabla \times \vec{h} = \vec{j} \tag{2.16}$$

we obtain

$$\nabla^2 \vec{h} = \frac{1}{\lambda_L^2} \vec{h} \tag{2.17}$$

which implies that a magnetic field is exponentially screened from the interior of a sample within the length of λ_L. This is known as London penetration depth and it gives a characteristic length over which the magnetic field and current can vary within a superconducting body.

Coherence length: In the condensed state, it is found that there are strong correlations among superconducting electrons. The concept of coherence length, ξ_o, was first proposed by Pippard (P3) in order to account for the inadequacy of the London equations for certain superconductors.* Later Faber and Pippard (F1) estimated ξ_o from the uncertainty principle as follows: Only electrons within kT_c of the Fermi energy can play a major role in the phenomenon and these electrons have a momentum range of $\delta P \sim kT_c/v_F$ where v_F is the Fermi velocity. Then

$$\delta x \gtrsim \hbar/\delta P \simeq \hbar\, v_F/kT_c$$

so that they define

$$\xi_o = a\hbar v_F/kT_c \tag{2.18}$$

where a is a numerical constant of order unity. This form was later confirmed by the microscopic theory of BCS (B1) with a numerical constant $a = 0.18$.

In the next section it will be seen that this coherence length ξ_o is closely related to the characteristic distance over which a density

*Extreme type I superconductors such as aluminum, tin and indium.

of superconducting electrons can vary within a superconductor.

2.2.2 Ginzburg-Landau Theory

In 1950 Ginzburg and Landau proposed a "phenomenological" theory of superconductivity (henceforth GL theory) in which a pseudo-wavefunction $\psi(r)$ was introduced as a complex order parameter. In this theory $|\psi|^2$ was to represent the local density of superconducting electrons, $n_s(r)$. Upon minimizing the free energy density which was expanded in powers of $|\psi|^2$ and $|\nabla\psi|^2$, they obtained a pair of coupled differential equations for $\psi(r)$ and the vector potential $A(r)$. The "phenomenological" nature of the theory was later lifted in 1959 when Gor'kov (G2) showed that the GL theory was derivable as a limiting case of the microscopic theory. The GL theory has been successful in treating the macroscopic behavior of superconductors where the overall free energy is important. For example, it can successfully predict various critical fields and the spatial variation of $\psi(r)$ in nonuniform cases.

Ginzburg and Landau postulated that, if ψ is small and varies slowly in space, the free energy density f_s can be expanded in a series of the form*

$$f_s = f_{no} + \alpha|\psi|^2 + \frac{\beta}{2}|\psi|^4 + \frac{1}{2m^*}\left|\left(\frac{\hbar}{i}\nabla - \frac{e^*}{c}\vec{A}\right)\psi\right|^2 + \frac{h^2}{8\pi} \qquad (2.19)$$

where α and β are real coefficients in the expansion and e* and m* are the effective charge and mass of superconducting electrons. By minimizing the volume integral of f_s with respect to the variations in ψ and A, they obtained two differential equations (GL equations):

*cgs Gaussian units are used up to Eq. (2.27).

$$\alpha|\psi| + \beta|\psi|^2\psi + \frac{1}{2m^*}\left(\frac{\hbar}{i}\nabla - \frac{e^*}{c}\vec{A}\right)^2\psi = 0 \tag{2.20}$$

$$\vec{j} = \frac{c}{4\pi}\nabla \times \vec{h} = \frac{e^*\hbar}{2m^*i}\left(\psi^\dagger\nabla\psi - \psi\nabla\psi^\dagger\right) - \frac{e^{*2}}{m^*c}\psi^\dagger\psi\,\vec{A} \tag{2.21}$$

together with the boundary condition

$$\left(\frac{\hbar}{i}\nabla - \frac{e^*}{c}\vec{A}\right)\psi\Big|_{\text{normal}} = 0 \tag{2.22}$$

which ensures that no current passes through the surface (i.e., superconductor-insulator interface).

Two special and obvious solutions of the above equations are

(1) $\psi = 0$ describing the normal state;

(2) $\psi = \psi_\infty \equiv (-\alpha/\beta)^{1/2}$ describing the superconducting state in a bulk medium in the absence of field and gradient.

Also, two characteristic lengths of a superconductor and their ratio can now be introduced as follows:

Coherence length (ξ): We consider a special case where there is no external field, i.e., A = 0. Letting $f = \psi/\psi_\infty$ in Eq. (2.20) we obtain

$$\frac{\hbar^2}{-2m^*\alpha}\nabla^2 f + f - f^3 = 0 \tag{2.23}$$

where it is natural to define GL coherence length by

$$\xi(T) \equiv \sqrt{\frac{\hbar^2}{-2m^*\alpha(T)}} \tag{2.24}$$

as a characteristic length for the variation of order parameter. $\xi(T)$ thus defined turns out to be approximately the same as the Pippard

coherence length, ξ_0, for pure metal well away from T_c (T4, p.112).*

Penetration depth (λ): Taking the curl of j in Eq. (2.21) and assuming that the order parameter in weak field is not changed from zero field value, i.e., $\psi = \psi_\infty$ to first order, we obtain

$$\nabla \times \vec{j} = -\left(\frac{e^{*2}\psi_\infty^2}{m^*c}\right) \vec{h} \tag{2.25}$$

By combining with the Maxwell equation, (2.16), we have

$$\nabla^2\vec{h} = \left(\frac{4\pi e^{*2}\psi_\infty^2}{m^*c^2}\right)\vec{h}$$

$$\equiv \frac{1}{\lambda^2}\vec{h} \tag{2.26}$$

which is exactly the same result as obtained by using the London equation (Eq. 2.17) . Thus the penetration depth λ is a characteristic length for the variation of magnetic field and current density.

Ginzburg-Landau parameter (κ): The ratio of the penetration depth, $\lambda(T)$, to the coherence length, $\xi(T)$, is defined as the GL parameter

$$\kappa \equiv \frac{\lambda(T)}{\xi(T)} \tag{2.27}$$

---

*The comment on the same page is essential in distinguishing the GL coherence length from the electrodynamic coherence length in the more general case. See also, L3, p.47.

which is expected to remain constant of temperature* since both $\lambda(T)$ and $\xi(T)$ diverge as $(1 - (T/T_c))^{-1/2}$ near T_c.

Type I and Type II superconductors: In 1957 Abrikosov examined the magnetic properties of superconductors as a function of the GL parameter κ. He found that superconductors with $\kappa > 1/\sqrt{2}$ would admit magnetic flux in the form of quantized vortices without becoming entirely normal at a lower critical field H_{c1} and remain in this mixed state up to an upper critical field H_{c2} where it would become entirely normal. This behavior was quite contrasting to the superconductors with $\kappa < 1/\sqrt{2}$ which would become normal at a well defined critical field H_c. Since then, those superconductors with $\kappa > 1/\sqrt{2}$ are known as type II and those with $\kappa < 1/\sqrt{2}$ as type I.

The physical distinction between type I and type II behaviors is due to an interfacial energy (surface tension) which is contained in the wall separating a normal phase from a superconducting phase. To clarify this point we consider a simplified situation where superconducting and normal phases are separated by a plane interphase boundary. Also, we suppose that there is an applied magnetic field H parallel to the boundary. This magnetic field is constant within the normal phase and attenuated exponentially within the interphase boundary to reach zero within the superconducting phase. On the other hand, the order parameter (or density of superconducting electrons) "heals" from its zero value

---

*Although κ is presumed to be temperature independent, some dependence on temperature arises depending on the details of temperature dependence of $\lambda(T)$ and $\xi(T)$ away from T_c, which is discussed in Chapter 4.

within the normal phase to its undisturbed value within the superconducting phase. This healing length is just given by the coherence length $\xi(T)$. Then the energy of the interphase boundary (as compared to the situation where the two phases are sharply divided) is lowered by admitting the applied magnetic field within the penetration depth λ (i.e., $-\frac{\mu_o}{2} H^2\lambda$) but is raised by having to suppress the density of superconducting electrons over the coherence length (i.e., $+\frac{\mu_o}{2} H_c^2\xi$, where $\frac{\mu_o}{2} H_c^2$ is the condensation energy per unit volume of the superconductor). Therefore the boundary energy per unit area is*

$$\sigma \simeq \frac{\mu_o}{2} (\xi H_c^2 - \lambda H^2) \tag{2.28}$$

When the applied field is H_c, the above surface energy is

positive for $\xi > \lambda$, i.e., $\kappa < 1$ (type I)

negative for $\xi < \lambda$, i.e., $\kappa > 1$ (type II)

Thus, when there is a boundary separating two phases, type I superconductors try to minimize the interphase boundary area, whereas type II superconductors try to maximize the boundary area, resulting in a maximum possible boundary area when the normal phase exists only in the cores of quantized vortices. As mentioned previously, the exact separation between the two types is at $\kappa = 1/\sqrt{2}$.

So far, our discussions involved only thermodynamically stable states in static fields. In the actual process of magnetic phase

*A more thorough argument to arrive at this equation is given in reference G3 (p.382).

transition from initially superconducting to finally normal state, a boundary between the two phases must be created so that the boundary energy as obtained in the preceding paragraph can be expected to play an important role.

In particular, the positive surface energy for type I superconductors suggests a possible persistence of Meissner state above the thermodynamic critical field, since the surface energy vanishes only at an applied field H_{sh} such that

$$\sigma = \frac{\mu_o}{2} (\xi H_c^2 - \lambda H_{sh}^2) = 0$$

or

$$H_{sh} = \frac{1}{\sqrt{\kappa}} H_c \qquad \text{where} \quad \kappa = \lambda/\xi \tag{2.29}$$

We can immediately see that this field H_{sh} is higher than H_c for small κ (type I) and it has been generally called a (magnetic) superheating field (to be discussed in the next section). Noting that the volume contribution to the free energy above the thermodynamic critical field Eq. (2.11) favors the transition to the normal state, we see that the above field is only an upper limit to the (metastable) superheated state.

For type II superconductors it is also possible to have a similar situation in which the Meissner state persists above the lower critical field H_{c1}. This is generally discussed in terms of a "surface-barrier field" opposing the entrance of mgnetic flux at the surface and this barrier field was found to coincide with H_c in the limit of large κ (01).

For both types of superconductor the existence of superheated state was first theoretically predicted by Ginzburg (G4) and later ob-

served experimentally for tin by Garfunkel and Serin (G5).

2.2.3 One-Dimensional GL Superheating Theory

Ginzburg (G4) first analyzed the superheating field by solving the GL equations for the one-dimensional case where a half of the space was occupied by a superconductor. He performed a numerical integration to obtain the superheating field as a function of the GL parameter κ. He also examined two limiting behaviors for small and large κ and found the superheating field H_{sh} in terms of bulk critical field, H_c, as follows:

(1) For $\kappa \ll 1$, $H_{sh} \simeq \frac{0.89}{\sqrt{\kappa}} H_c$ * (extreme type I) (2.30)

(2) For $\kappa \gg 1$, $H_{sh} \simeq H_c$ (extreme type II) (2.31)

The same problem was later treated numerically for better accuracy by Matricon and St. James (M5).

The prediction of one-dimensional theory is considered to put an upper limit on the superheating field, since possible variations of the order parameter in other directions such as parallel to the surface may lower the actual superheating field. This problem has been studied in terms of the stability of the superheated Meissner state against spatial fluctuations of order parameter by various authors (F2,K2,K3). In particular, Kramer (K3) found that, for $\kappa \gtrsim 0.5$, another instability

* Later the numerical constant in this limit was shown to be $2^{-1/4} = 0.841$ rather than 0.89 by the Orsay group on superconductivity (O1).

occurred at a field, H_{s1}, lower than H_{sh}. For large κ limit he obtained

$$H_{s1} = 0.745\ H_c$$

His estimate of the field H_{s1} is shown in the phase diagram of Fig. 2.1 together with the prediction of one-dimensional GL theory as evaluated by Matricon and St. James (M5). In this phase diagram all the critical fields are reduced by the thermodynamic critical field H_c and shown as a function of GL parameter $\kappa = \lambda/\xi$. Thus we have type I superconductors for $\kappa < 1/\sqrt{2}$ where two thermodynamically stable phases (Meissner and normal states) are separated by the line $H/H_c = 1.0$. For $\kappa > 1/\sqrt{2}$ we have type II superconductors which go from Meissner to mixed state at $h_{c1} = H_{c1}/H_c$ and into normal state above $h_{c2} = H_{c2}/H_c$. This phase diagram will be found convenient in discussing the present experimental results in Chapters 3 and 4.

2.2.4 Previous RF Critical Field Measurements

In going from superconducting to normal state, the surface resistance of a metal changes by several orders of magnitude. Thus if a small fraction of surface area becomes normal while a high rf magnetic field is being sustained, it can lead to a thermal runaway situation where the power dissipated into the normal region heats up the surrounding area above the transition temperature which, in turn, drives more area normal. This runaway process is generally called "magnetic-thermal breakdown" and the field at which this process is initiated is called the breakdown field or rf critical field.

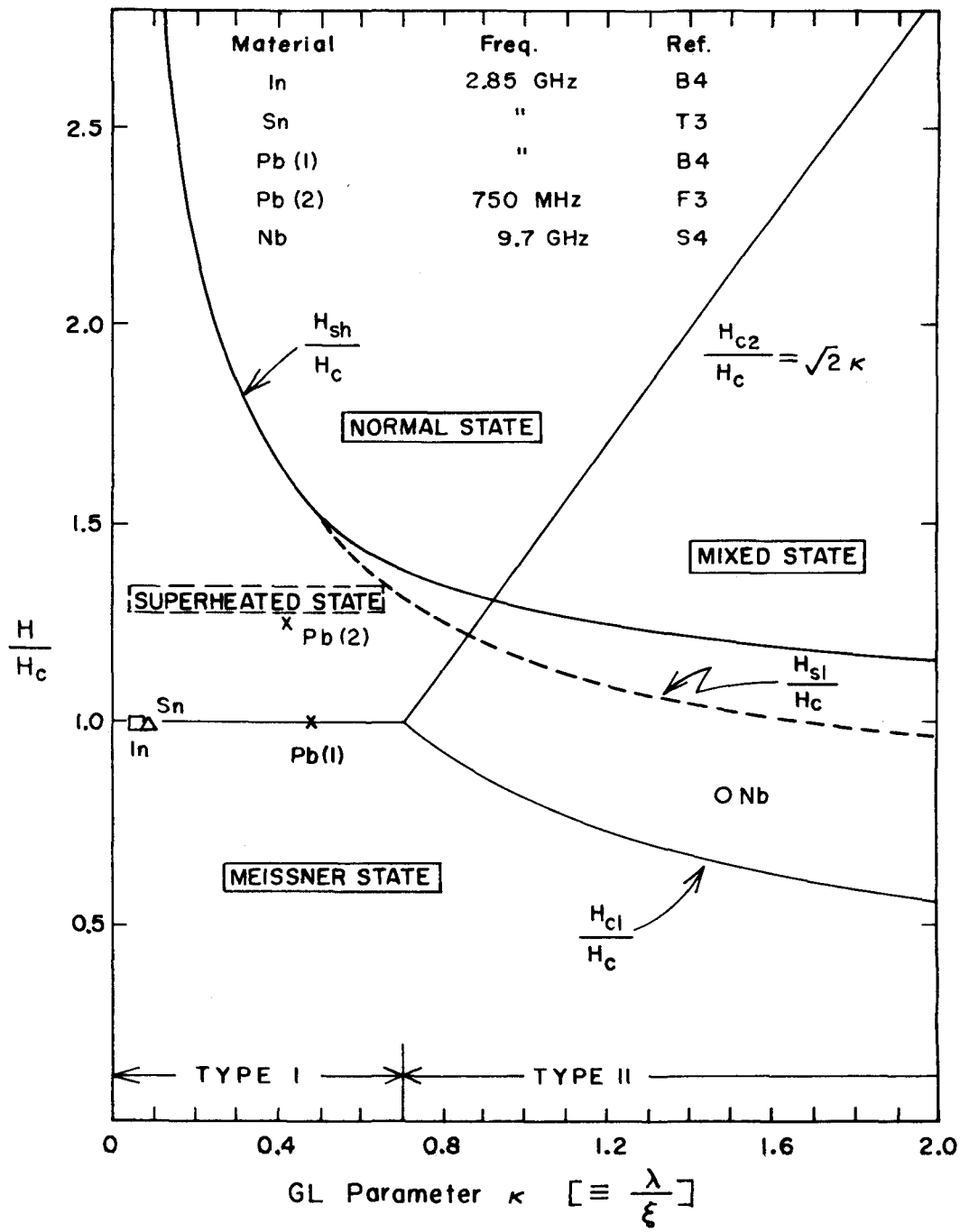

Fig. 2.1 Phase Diagram of Superconductors: All fields are normalized to thermodynamic critical field and shown as a function of Ginzburg-Landau parameter κ. RF critical fields previously measured for Sn, In, Pb and Nb are also shown. H_{sh} was evaluated in M5, H_{sl} in K3 and H_{cl} in H11.

Most of the previous measurements of critical magnetic field at radio frequencies were performed on the walls of resonant cavities. Among the elemental superconductors studied, tin, indium and lead belong to type I superconductors and niobium (colombium) to type II superconductors. Turneaure (T3) measured the critical field of electroplated tin in 2.85 GHz resonator and found that the rf critical field, H_c^{rf}, was close to the dc critical field. Similar results were later found for electroplated indium and lead at 2.85 GHz (B4). For lead it was also reported by Flecher et al. (F3) that the rf magnetic field higher than the dc critical field by 25% at 4.2°K was observed at 750 MHz. To the author's knowledge, this is the only reported observation of superheating at radio frequencies for type I material. For niobium Schnitzke et al. (S4) recently attained rf critical field higher than the first critical field, H_{c1}, as a result of improved material processing technique. Also, more recent work on type II alloys such as Nb_3Sn (P10,H9) and $Nb_{0.4}Ti_{0.6}$ (G7) show that H_c^{rf} is not limited by H_{c1} in type II materials. These previous rf critical field results are summarized in the phase diagram of Fig. 2.1.

Concurrently with the above efforts in measurements and improvements in materials processing, there have been phenomenological attempts to determine what limits the rf magnetic field which can be attained in superconducting resonators. Factors that have been considered to be important in determining the rf critical field include the thermal stability of cavity surfaces (S5), the power dissipation in a single isolated fluxoid on the resonator surface (M6) and the magnetic boundary

energy between superconducting and normal phases (H10).

Theoretical treatment of phase transition from superconducting to normal state in radio frequency field has been extremely scarce. Only a very limited qualitative argument has been used in "predicting" the rf critical field. Halbritter (H10) used a surface energy argument similar to the one given in Section 2.2.2 to arrive at the same result as the superheating field obtained by Ginzburg (G4). Then it may be expected that the superheating field will put an intrinsic limit on the rf magnetic field that can be reached. Prior to the present study, there has been only one instance of the observation of rf magnetic field higher than the thermodynamic critical field for type I superconductors (F3). For type II superconductors the rf critical field has been shown to be somewhat higher than H_{c1}.

In the present study it was found that indeed the superheating field puts an upper limit on the rf critical field in the frequency range between 100 and 300 MHz. This was initially found for lead at 205 MHz as shown in Chapter 3. Also, by resorting to material whose GL parameters could be varied, a similar conclusion was found for κ up to about 1.8, which is well into the type II region.

2.3 Summary

The rf surface resistance of superconductors was reviewed for its physical origin and for its historical background. There is now good agreement between the past rf experiments and the theoretical surface resistance based on microscopic theory, provided that the rf

magnetic field is small compared with the thermodynamic critical field. At low temperatures, there are other loss mechanisms that give rise to an effective surface resistance, only some of which are understood.

The magnetic behavior of superconductors in a static magnetic field is well understood in terms of various critical fields. However, the situation involving rf magnetic fields is rather uncertain in that there has been no definite proof, either experimentally or theoretically, as to what limits the attainable rf magnetic field. It was once thought (up to about 1971-1972) that the rf critical magnetic field was given by the thermodynamic critical field for type I superconductors and by the lower critical field, H_{c1}, for type II superconductors. More recent experiments suggest that the above statement does not hold for type II superconductors. A large portion of the present investigation is directed to answering experimentally the question of the rf critical magnetic field for both type I and type II superconductors.

Chapter III

SURFACE RESISTANCE AND RF CRITICAL MAGNETIC FIELD OF LEAD AT 205 MHz

3.1 Introduction

Lead is one of the superconductors whose superconducting properties have been studied quite extensively in the past. It is an attractive material for potential rf applications, not only because of its high critical field (803 gauss at 0°K) and relatively high transition temperature (7.2°K), but also because of its wide availability and ease in handling. In particular, low frequency rf resonant cavities, which are often geometrically complex, can easily be coated with lead by such means as electroplating on a copper substrate. The rf superconducting properties of such lead have been studied previously in the frequency range of 1-10 GHz. However, no systematic study has been undertaken in the lower frequency range ($\sim$ 100 MHz) where there are possible practical rf applications such as the acceleration of heavy ions using recently developed rf resonant structures. Thus the present study, whose results are presented in this chapter, was designed to investigate the current carrying properties of lead electroplated on copper in terms of its surface resistance and rf critical magnetic field at this lower end of radio frequencies.

3.2 Experimental Method

The use of rf resonant cavities is a convenient means commonly employed in the measurement of very low surface resistance as well as in the generation of high rf magnetic fields. For the present investigation

a coaxial resonator was designed so that the surface resistance of lead could be determined and at the same time a high rf magnetic field comparable to the thermodynamic critical field of lead could be generated in a well-defined area. This resonator is described in the next section where it is also shown how surface resistance is related to the characteristic quantities of the resonator. In subsequent sections general experimental procedures are given, followed by a description of how the characteristic quantities of the resonator are determined from the measured quantities and then related to the quantities of present interest: the surface resistance and the magnetic field level within the resonator.

3.2.1 Half-Wave Coaxial Resonator at 205 MHz

In order to study the surface resistance and rf critical magnetic field of superconducting lead electroplated on copper, a coaxial resonator was constructed from OFHC (Oxygen Free High Conductivity) copper as shown in Fig. 3.1. The resonator consisted of four parts: the outer conductor, the center conductor and the two end plates. The midsection of the center conductor was constricted as shown. The reason for this was twofold. One was to lower the resonant frequency to the desired range. The other, more important, was to enhance the surface magnetic field as well as to localize the high magnetic field region to a well-defined area. The center conductor was supported from both ends by the sapphire rods with low loss tangent (Y1).

The electromagnetic field distribution in the resonator was evaluated analytically using transmission line and lumped parameter approximations. In this approximation, the resonant frequency, the electric

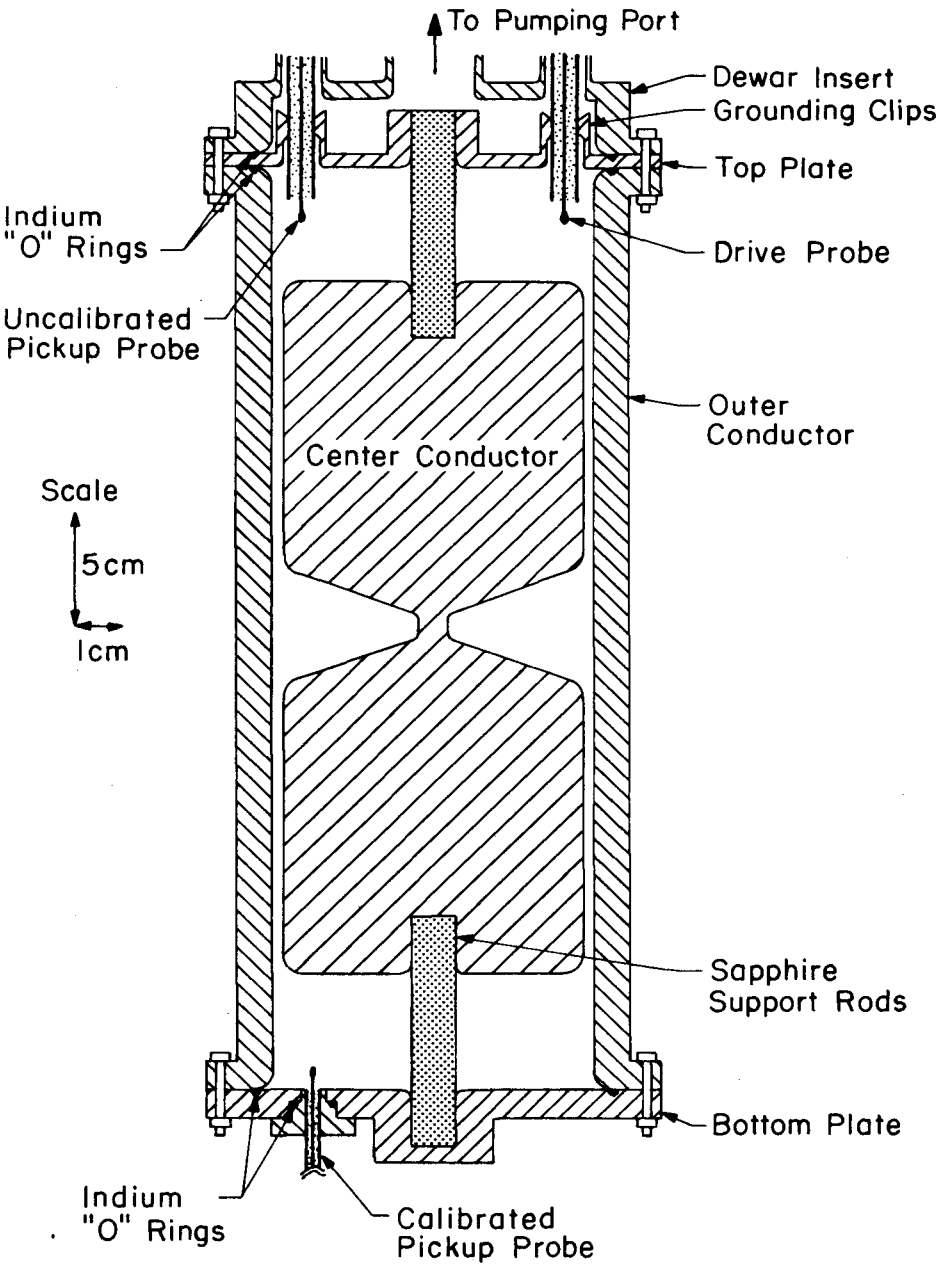

Fig. 3.1 The half-wave 205 MHz coaxial resonator: The center conductor is supported by two sapphire rods so that it makes no direct electrical connection to other parts. The resonator is coupled to the outside rf system by three coupling probes as shown. Note the difference in the vertical and horizontal scales.

and magnetic field distributions, the total energy content and the geometrical factor of the resonator were evaluated. The resonant frequency thus determined agreed with measurement within 1%, indicating that this approximation serves well for the present purpose. The relative radial electric field, E_ρ, and the azimuthal magnetic field, H_ϕ, on the surface of the center conductor are shown in Fig. 3.2.

The total energy content, W , of a resonator at resonance is given by (P407,B2)

$$W = \frac{1}{2} \int_V \left(\frac{\varepsilon}{2} E^2 + \frac{\mu}{2} H^2\right) dV \qquad (3.1)$$

where the time averaging has been performed. E and H are the spatial part of the electric and the magnetic field, respectively. ε and μ are, respectively, the permittivity and the permeability within the volume V of the resonator. Since the time-average electric and magnetic energies are equal at resonance (Ibid), W can be expressed in terms of either the electric or the magnetic field distribution. Using the field distribution as obtained above, it was found for this resonator

$$W = 7.32 \times 10^{-7} H_{max}^2 \qquad \text{(joule)}$$

$$\equiv g^{-1} H_{max}^2 \qquad (3.2)$$

where H_{max} is the (amplitude of the)* magnetic field at the midsection

*Throughout this dissertation all rf fields (electric and magnetic) are represented by their amplitude so that, for example, the full expression for the magnetic field at the midsection of the center conductor is $H_{max}\sin(\omega t)$ where ω is the rf angular frequency.

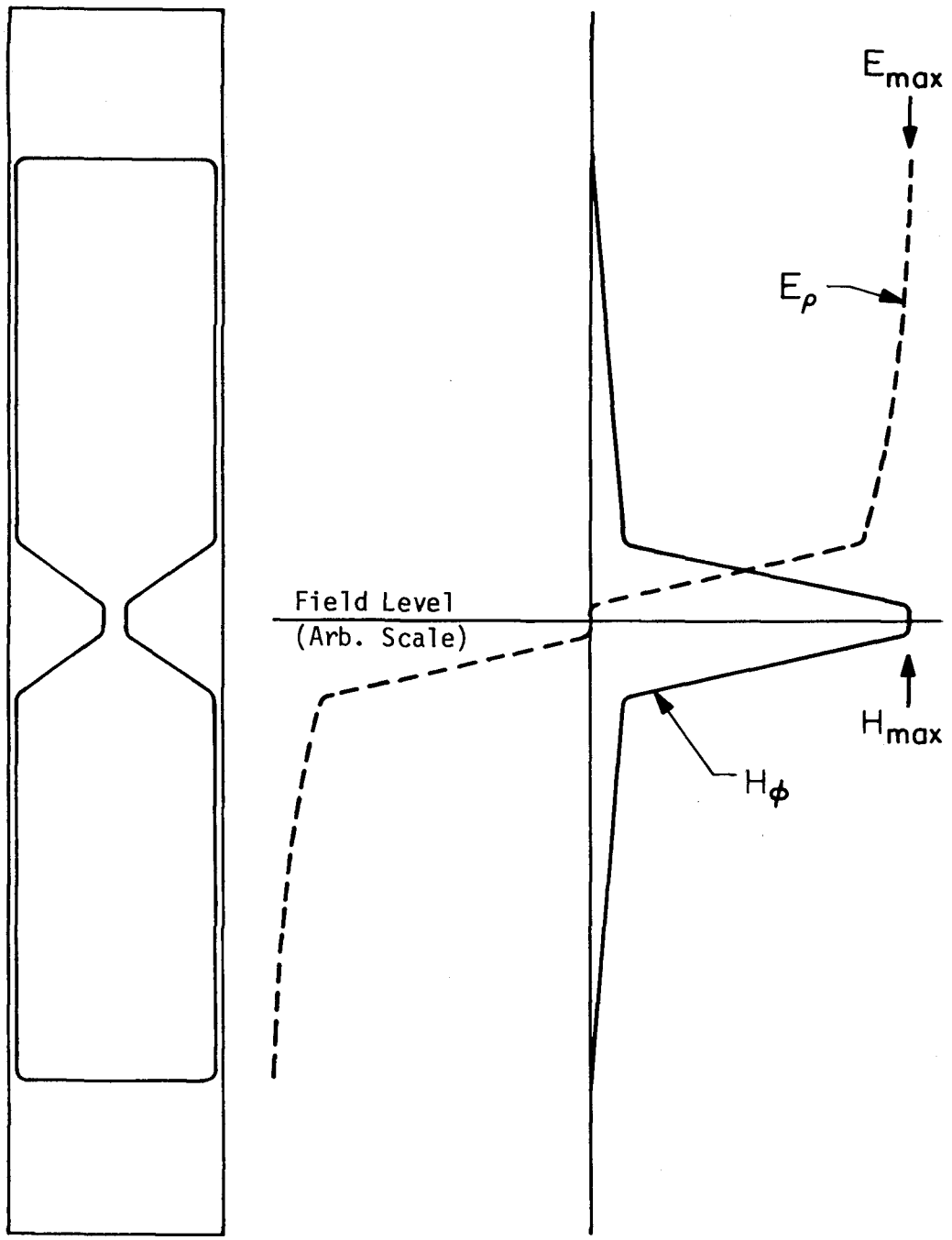

Fig. 3.2 The radial electric field, E_ρ , and the azimuthal magnetic field, H_ϕ , at the surface of the center conductor are shown in arbitrary scale. The vertical scale is the same as in the resonator shown on the left side where the center conductor is 30.5 cm in length from one end to the other.

of the center conductor in gauss, and g is defined as H_{max}^2/W. It can also be expressed as

$$W = 3.71 \times 10^{-9} V_{max}^2 \qquad \text{(joule)}$$

$$\equiv d^{-1} V_{max}^2 \tag{3.3}$$

where V_{max} is the rf voltage at the end of the center conductor in volts, and d is defined as V_{max}^2/W. Both of the above expressions will be useful in the discussion of calibration (Sec. 3.2.6).

Another quantity of practical importance is the ratio of maximum magnetic field to maximum electric field within the resonator. The locations of their occurrence are shown clearly in Fig. 3.2. This ratio was found to be

$$H_{max}/E_{max} = 190 \text{ gauss/(MV/m)} \tag{3.4}$$

The geometrical factor of a resonator is a quantity which is very useful in dealing with resonant cavities in general. This is related to the quality factor of a resonator which is a measurable quantity and defined by

$$Q_o \equiv 2\pi f \, W/P_{diss} \tag{3.5}$$

where W is the total energy of the cavity whose resonant frequency is f and P_{diss} is the average power dissipated within the resonator. W is obtained by integrating the energy density over the volume of the cavity as in Eq. (3.1). Assuming there is only resistive dissipation

due to the surface current, P_{diss} is given by

$$P_{diss} = \frac{1}{2} \int_S R_s H^2 \, dS \tag{3.6}$$

where R_s is the surface resistance of the wall, S , enclosing the cavity volume, V . Then

$$Q_o = 2\pi f \frac{\frac{1}{4} \int_V (\varepsilon E^2 + \mu H^2) \, dV}{\frac{1}{2} \int_S R_s H^2 dS}$$

Or

$$Q_o R_s = \pi f \frac{\int_V (\varepsilon E^2 + \mu H^2) \, dV}{\int_S H^2 \, dS} \equiv \Gamma \tag{3.7}$$

Since the right hand side is dependent only on the geometry of the resonator, it is a constant for a given normal mode and defined as the geometrical factor Γ .

For the present resonator, using the known field distribution, the geometrical factor was evaluated to be

$$Q_o R_s = 7.00 \ \Omega$$

This was verified within experimental error ($\pm$ 3%) by measuring the Q of copper (unplated) resonator at room, liquid nitrogen, and liquid helium temperatures, where R_s was determined independently from the dc

resistivity of the same material (Chamber's interpolation formula (C1) was used to take into account the anomalous skin effect below room temperature).

3.2.2 Preparation of the Surface

Once the parts of the resonator were machined, all the surfaces were polished with emery papers of decreasing grain size (320, 400, 600) and finally with levigated alumina polishing compound (grain size = 1-3μ). After the mechanical polishing all the surfaces were electroplated with lead to a typical thickness of 1.5 - 3μ . Since the general electroplating procedure and problems are discussed elsewhere (G6, P11, T3) only a brief description of the procedure is given below.

There are three main steps in obtaining the lead layer on copper by this method:

1) Cleaning. The first step was to remove the oxide on the copper surface. This was done by electrically polishing the copper surface in an electropolishing solution* followed by a thorough rinsing with deionized water.
2) Electroplating. As soon as the electropolishing solution was rinsed away, the copper piece was placed in an electroplating solution**

---

*The electropolishing solution was a mixture of 1 part Electro-Glo "200" (supplied by Electro-Glo Co., Chicago) and 3 parts 85% phosphoric acid by volume.

**At the time of this study, it was found that the addition of "Shinol LF-3" (supplied by Harstan Chem. Corp., Brooklyn, N.Y.) in place of the usual animal glue to lead fluoborate solution gave an improved surface finish.

with appropriately shaped electrodes which were made from 99.9% purity lead foil. Initially a few pulses of very short duration ($\sim$ 1 sec) were applied at a current density of 80 mA/cm^2 in order to obtain a uniform thin lead layer as a "starter". Then the plating continued at a current density of 8 mA/cm^2 until the desired thickness was obtained.

3) Rinsing and drying. After plating, the surface was rinsed in running deionized water to remove the plating solution. This was followed by rinsing with absolute ethanol and then blown dry in a stream of dry nitrogen.

3.2.3 Cryogenic Apparatus

After all the parts were plated, the resonator was assembled and attached to a dewar insert. Indium "O" rings were used where parts were joined in order to obtain vacuum tight seals as well as current carrying joints* (see Fig. 3.1). The dewar insert, shown schematically in Fig. 3.3, consisted of four long stainless steel tubes leading up to the top of the dewar at room temperature. One of the tubes was used as a pumping line to pump on the resonator, the two others to guide coaxial lines into the cavity resonator for rf coupling and the last one to feed helium gas into the resonator when necessary.

Immediately after the assembly, the resonator was pumped down to about 10 μHg through the dewar insert so as to avoid any possible oxidation of the freshly plated surfaces due to exposure to the atmosphere. The resonator was then filled with gaseous helium** which had been filtered

*No observable loss was introduced by these joints since they carried only a negligible fraction of the total oscillating current.

**Purity 99.995% (Gardner Cryogenics, Glendale, California).

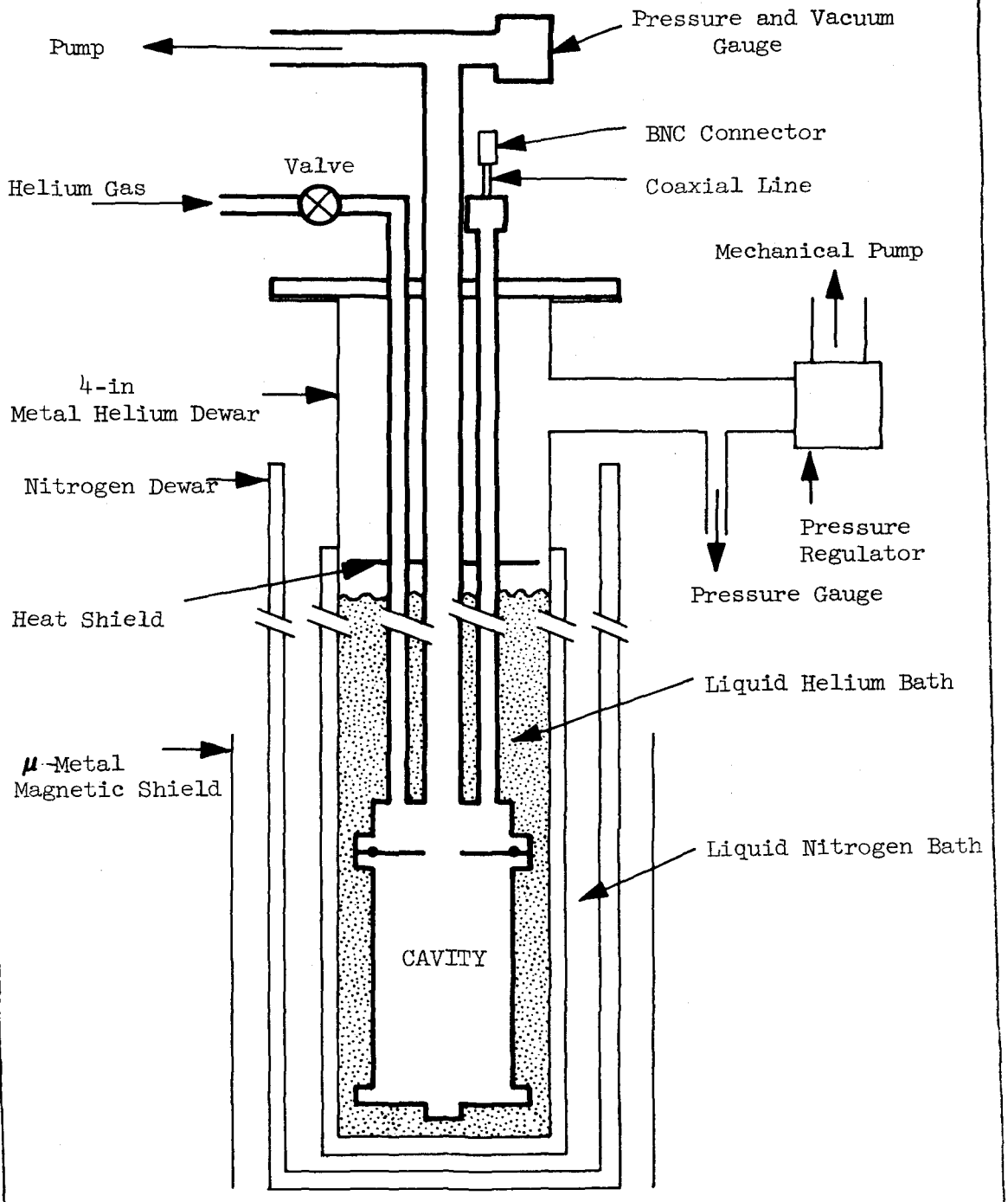

Fig. 3.3 The dewar insert (in bold lines) and cryogenic equipment are shown schematically. The pressure within the resonator could be varied by either feeding helium gas or pumping by a small mechanical pump. The temperature of the helium bath in the dewar was varied by pumping with a large mechanical pump through the pressure regulator.

through a liquid nitrogen cold trap. Once it was full, the resonator was pumped again and this process of "flushing" with gaseous helium was repeated several times in order to get rid of impurities that might condense on the cavity surfaces at liquid helium temperatures.

For the low temperature experiment, a 4-inch metal dewar was used in conjunction with standard cryogenic equipment shown in Fig. 3.3. The earth's magnetic field was reduced by a mu-metal shield to below 15 milligauss over the entire experimental space. The typical working temperature range was between 4.2 and 2°K. The temperature of the helium bath was varied by pumping with a mechanical pump and a pressure regulator. The vapor pressure of the helium bath was read on a Wallace and Tiernan pressure gauge and related to temperature using the 1958 He^4 scale of temperatures (D3).

In order to make a thermal contact to the cavity center conductor, the resonator was filled with helium exchange gas at a pressure of about 100μ Hg while low power measurements were made. For high power measurements, the resonator was filled with liquid helium then pressurized to 5-15 psi above the atmospheric pressure with gaseous helium. The pressurization was necessary in order to avoid spark discharging that took place within the resonator at lower vapor pressures of helium.

3.2.4 RF Instrumentation

Because a superconducting resonator has an extremely high Q (on the order of 10^8 at 205 MHz in the present case) the excitation of such a resonator by a conventional rf oscillator poses a special problem.

This is because the resonator bandwidth is much smaller than the frequency stability of the oscillator. The following two methods are conventionally used to overcome this problem:

1) Phase-lock operation. In this mode of operation the resonator is driven by an external voltage controlled oscillator (VCO) whose frequency and phase are adjusted to those of the resonator by means of a feed-back.
2) Self-resonating loop operation. If an amplification loop is closed through the resonator of interest, then a spontaneous oscillation takes place when the gain and the phase of the loop are optimized.

Throughout this investigation the phase-lock operation was used more extensively because of its ease in making measurements. The block diagram of the rf instrumentation used for the phase-lock operation is shown in Fig. 3.4. For a stable oscillation of the resonator, the driving signal out of VCO had to be at proper phase and frequency. This condition was achieved in the following manner. The field within the resonator was sampled through one of the pickup probes. The phase difference between this sampled signal and the VCO signal was detected by a mixer (here used as a phase detector), then amplified by a dc amplifier and fed into the frequency control input of the VCO. As a result, the external oscillator (VCO) was "locked" to the resonator once the phase shifter in the loop was adjusted properly at the beginning of operation.

In order to avoid impedance matching problems, all the electronics used, including coaxial cables and transmission lines to the resonator, had a characteristic impedance of 50 ohms.

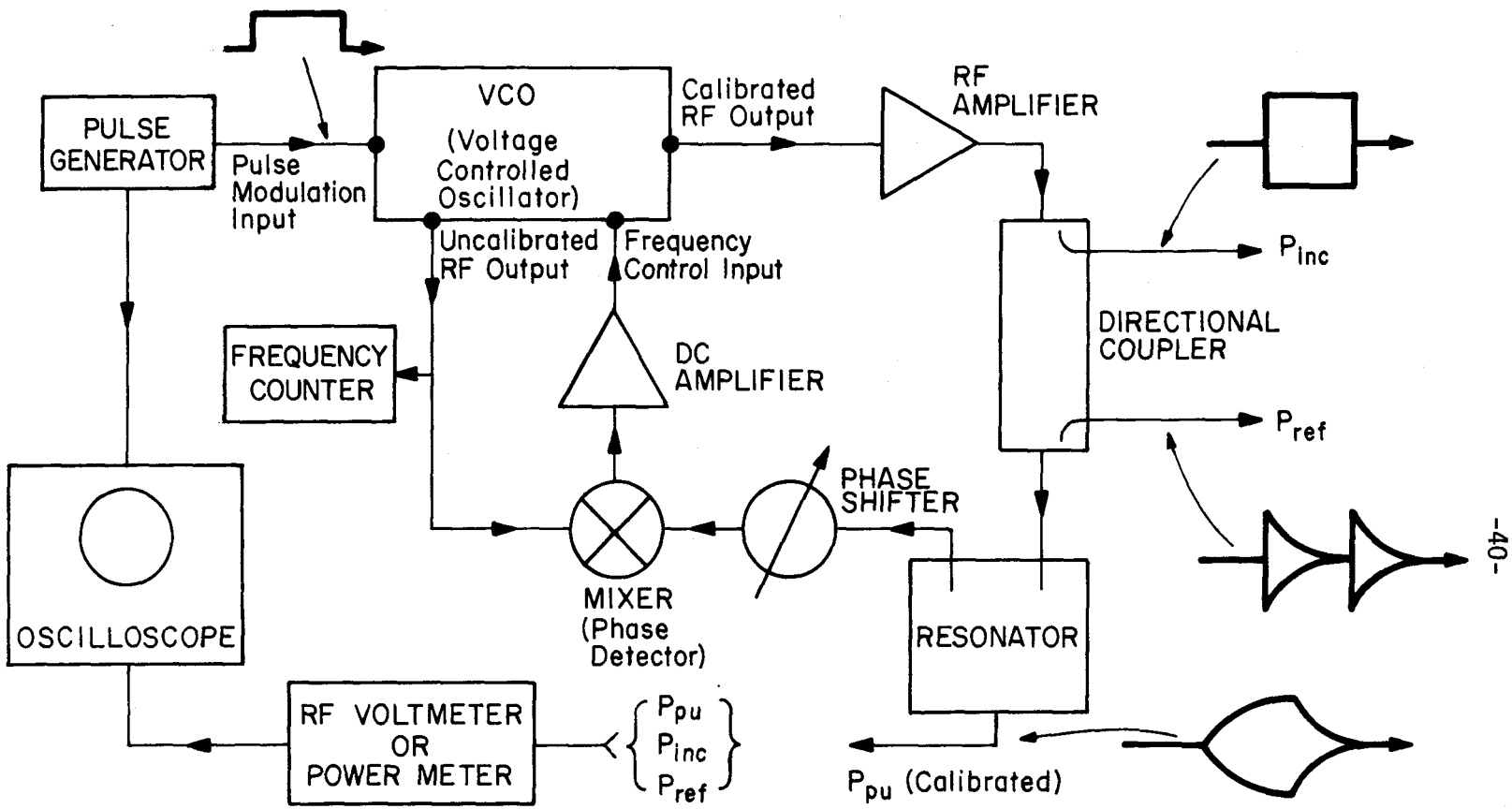

Fig. 3.4 The block diagram of the rf instrumentation used in the phase-lock operation of the superconducting resonator. The external voltage controlled oscillator is "locked" to the resonator by means of a feedback. Approximate rf envelopes of the incident, reflected, and pickup voltages are also shown.

3.2.5 General Theory of Measurement

In this section it is shown how a set of experimentally measured quantities are related to the characteristic quantities of a resonant cavity. In particular, we are interested in the following two characteristic quantities of a resonator:

1) the total energy content of the resonator, W (to be related to H_{max}
2) the intrinsic quality factor, Q_o.

The system of a resonant cavity with two coupling ports may be looked at as a four-terminal passive device. The coupling ports at frequencies on the order of 100 MHz are normally coaxial lines whose ends are coupled either capacitively or inductively to the electromagnetic fields of the cavity. Measurements are made by sending an rf signal into one port and looking at a signal picked up through the other port (see Fig. 3.5a). The measured quantities are the incident power, P_{inc}, the reflected power, P_{ref}, the power picked up, P_{pu}, and their time variations. In the following we assume that every quantity has been averaged over an rf period.* Balancing the power flow into the system, we have

$$P_{inc}(t) - P_{ref}(t) = P_{diss}(t) + P_{pu}(t) + dW(t)/dt \qquad (3.8)$$

where P_{diss} is the power dissipated into the cavity itself and dW/dt is the time rate of change of the total energy content of the cavity,

*The time dependence we are dealing with here is on the scale of characteristic decay time of the resonator ($\sim$ 100 msec as compared to the rf period of 5×10^{-9} sec).

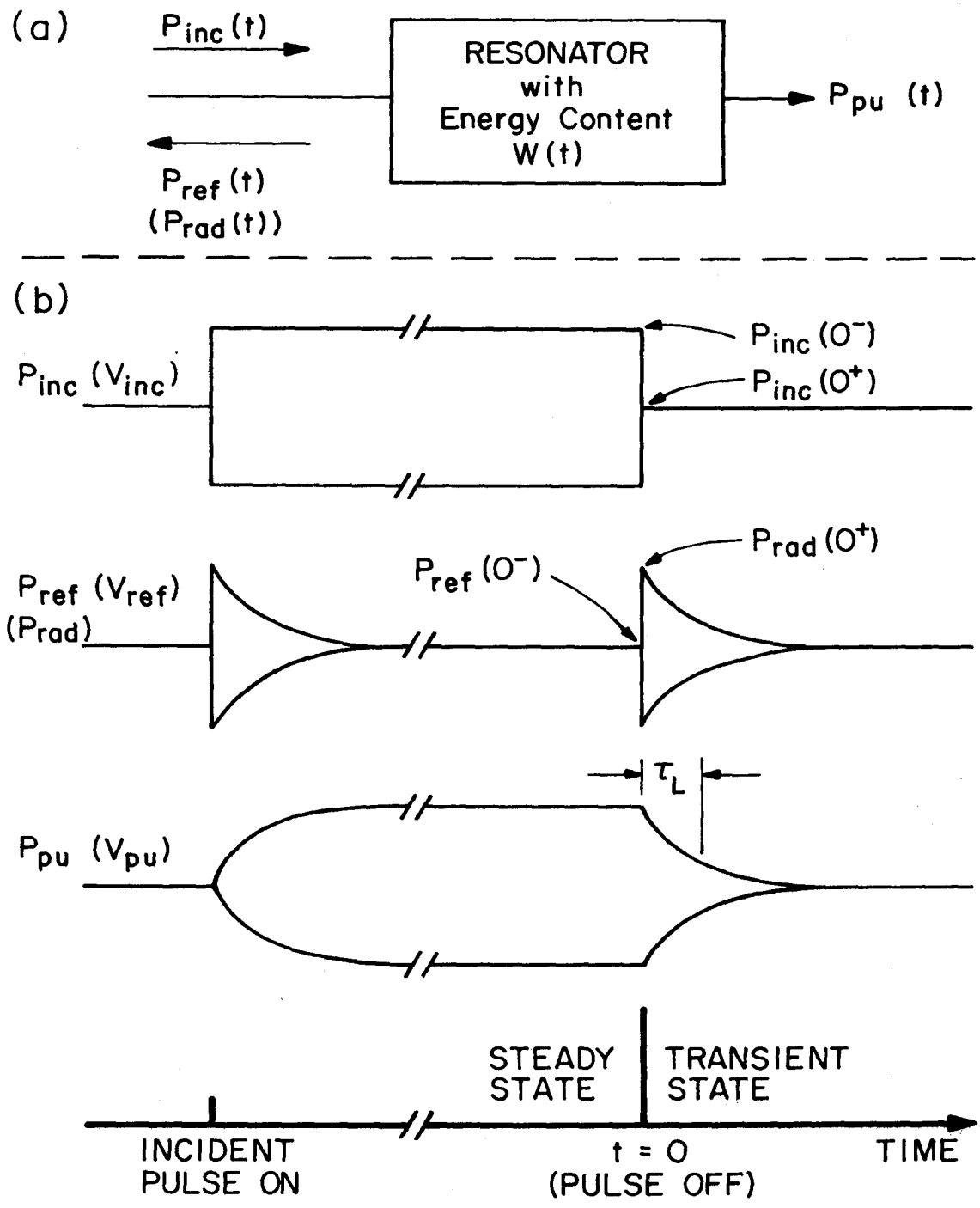

Fig. 3.5 (a) The power flow into and out of the resonator is shown. (b) Typical rf envelopes of the rf voltages when in the pulsed mode are shown for the case where the incident port is critically coupled to the resonator. P_{pu} is proportional to the energy content of the resonator.

W. By definition, the intrinsic (or unloaded) quality factor is given by

$$Q_o = \omega W / P_{diss} \tag{3.9}$$

where ω is the angular resonant frequency. For a fixed pickup coupling, P_{pu} is proportional to the energy content, i.e.,

$$P_{pu} = \alpha^{-1} W \tag{3.10}$$

where α is the coupling constant to be determined. Then the reciprocal of Q_o can be expressed as

$$Q_o^{-1} = \frac{1}{\omega\alpha}\left[\frac{P_{inc} - P_{ref}}{P_{pu}} - 1 - \alpha \frac{\ln P_{p-u}}{dt}\right] \tag{3.11}$$

In order to determine α, we consider a situation where the rf incident power has been on for a long time and is turned off at $t = 0$ (see Fig. 3.5b). Then at $t = 0^-$ (just before P_{inc} is turned off) the system is in steady state so that $dP_{pu}/dt = 0$. Thus,

$$Q_o^{-1}(t=0^-) = \frac{1}{\omega\alpha}\left[\frac{P_{inc}(0^-) - P_{ref}(0^-)}{P_{pu}(0^-)} - 1\right] \tag{3.12}$$

When the incident power is turned off at $t = 0$, the cavity loses its stored energy with the characteristic time of the loaded cavity, τ_L, which can be directly measured. For $t \geq 0$ then we have

$$P_{inc} = 0$$

$$P_{ref}(t) = P_{rad}(0^+)\, e^{-t/\tau_L}$$

$$P_{pu}(t) = P_{pu}(0^+)\, e^{-t/\tau_L} \tag{3.13}$$

where $P_{ref}(t)$ is now the power radiated into the incident port. Therefore,

$$Q_o^{-1}(t=0^+) = \frac{1}{\omega\alpha}\left[\frac{-P_{rad}(0^+)}{P_{pu}(0^+)} - 1\right] + \frac{1}{\omega\tau_L} \tag{3.14}$$

Since the intrinsic cavity Q is the same whether the system is in steady state or transient state, we can equate the above equation to Eq. (3.12). Using $P_{pu}(0^-) = P_{pu}(0) = P_{pu}(0^+)$ we obtain

$$\alpha = \tau_L \frac{P_{inc}(0^-)}{P_{pu}(0)}\left[1 + \frac{P_{rad}(0^+) - P_{ref}(0^-)}{P_{inc}(0^-)}\right] \tag{3.15}$$

Since all the quantities on the right hand side are measured, this determines the coupling constant, α , which can then be used in Eq. (3.10) to determine the energy content of the cavity, or in Eq. (3.11) for general Q measurement.

The special case of experimental interest is shown in Fig. 3.5b where the incident port is critically coupled to the resonator so as to give $P_{ref}(0^-) = 0$. In this case the coupling constant is given as

$$\alpha = \tau_L \frac{P_{inc}(0^-)}{P_{pu}(0)}(1 + \beta) \tag{3.16}$$

where

$$\beta = P_{rad}(0^+)/P_{inc}(0^-)$$

So far we have dealt with resonant cavities in general. Now in order to relate the field level within the resonator to the measured

quantities we need the field distribution within the particular resonator. The relationship between the energy content and the field within the present resonator was obtained in Sec. 3.2.1. Then using Eq. (3.2) and (3.10) we obtain

$$H_{max} = (gW)^{1/2}$$

$$= (\alpha g\, P_{pu})^{1/2} \tag{3.17}$$

So, the measurement of P_{pu} directly gives the surface magnetic field at the midsection of the center conductor once the coupling constant α is determined. Also, the intrinsic quality factor at any field level is given by Eq. (3.11), which holds for a general time dependent case. If the resonator is in a steady state, then

$$Q_o^{-1} = \frac{1}{\omega\alpha}\left[\frac{P_{inc} - P_{ref}}{P_{pu}} - 1\right] \tag{3.18}$$

3.2.6 Measurement, Calibration and Error Estimation

The resonator was coupled capacitively to the outside rf system by way of three probes attached to coaxial transmission lines. Two probes at the top of the cavity (see Fig. 3.1) were coupled to the resonator field and their coupling strength was variable. One of them was used to drive the resonator at any desired coupling strength. The other one was always coupled weakly and was used only to sample the field of the resonator for the phase-lock operation. The third or pickup probe at the bottom of the resonator was fixed to the end plate and used solely for the purpose of field level determination upon calibration.

The calibration of the resonator field level was of basic importance in this study. For the present coaxial resonator two independent calibration procedures were employed.

1) The first method was to use the procedure as outlined in the general theory of measurement (Sec. 3.2.5). In this procedure, the magnetic field level of interest, H_{max}, was related to the measured quantity P_{pu} by Eq. (3.17),

$$H_{max} = (\alpha g P_{pu})^{1/2}$$

Thus it was only necessary to determine the coupling constant α since g was evaluated with the known field distribution as given in Sec. 3.1.1. The coupling constant was normally determined by critically coupling the drive probe so that from Eq. (3.16)

$$\alpha = \tau_L \frac{P_{inc}(0^-)}{P_{pu}(0)} (1 + \beta) \quad \text{with} \quad \beta = \frac{P_{rad}(0^+)}{P_{inc}(0^-)}$$

Therefore α was determined by measuring four quantities: τ_L on the scope, $P_{inc}(0^-)$, $P_{pu}(0)$ and $P_{rad}(0^+)$ by the rf voltmeter. (Note that only the ratios of these powers are needed here.)

2) In the second method the coupling constant α was determined by a direct application of an rf voltage to the cavity in the following manner (Details of this method are discussed in D2). An rf voltage was applied between the center and outer conductor at one end of the resonator by lowering the drive probe until its tip touched the end face of the center conductor (see Fig. 3.1). This applied voltage, V_a,

is related to the voltages measured at the incident and the reflected port of the directional coupler (Fig. 3.4), V_{inc} and V_{ref} respectively, by (D2) $V_a = (V_{inc}V_{ref})^{1/2}$ under an assumption that the resonator is an open circuit at resonance in this configuration.

Then by measuring the resultant voltage, V_{pu}, at the pickup probe (the bottom probe in Fig. 3.1) we can express V_a in terms of the measured ratio $r = (V_{inc}V_{ref})^{1/2}/V_{pu}$ as

$$V_a = r\, V_{pu}$$

Now the magnetic field at the midsection of the center conductor, H_{max}, can be related to the voltage at the end of the center conductor by combining Eqs. (3.2) and (3.3). Thus we obtain

$$H_{max} = (g/d)^{1/2}\, V_{max}\ ^*$$

or, since V_{max} is just the applied voltage at the end of the center conductor,

$$H_{max} = (g/d)^{1/2}\, r\, V_{pu}$$

Finally, expressing V_{pu} in terms of the power at the pickup probe, P_{pu} (i.e., $P_{pu} = V_{pu}^2/2R$ where R = 50 ohms), we have

---

*Previously this relationship was verified experimentally (Y1) within about 5% in a similar resonator by applying an rf voltage in the same manner as described here and measuring the magnetic field at the midsection of the resonator.

$$H_{max} = ((2Rr^2/d)g\ P_{pu})^{1/2} \qquad (3.19)$$

Therefore, the coupling constant α in this scheme is given by

$$\alpha = 2Rr^2/d$$

which can be determined by the measurements of V_{inc}, V_{ref} and V_{pu} since d is a numerical constant given previously.

The fields determined by the above two methods typically agreed within 6%. Once their agreement was established, the first method was routinely used to determine α in different low temperature experiments on the same resonator, since it was operationally simpler.

The sources of error in the determination of H_{max} and Q_o were:
1) In the determination of τ_L. An oscilloscope trace of the decaying pick-up voltage was photographed and its readings as a function of time were plotted on a semi-log scale to determine the slope τ_L. The error in τ_L thus determined was estimated to be less than 3%.

2) In the measurements of P_{inc}, P_{ref} and P_{pu}. In the CW mode their values were read on a power meter and the reading error was less than 1%. In the pulsed mode, their corresponding voltages were displayed on an oscilloscope and read within 1.5%, so that the errors in power determination in the pulsed mode were estimated to be 3% or less.

Combining these errors, we estimate the total errors, Δ , in the quantities of present interest to be as follows:

	Absolute	Relative
$\Delta H_{max}/H_{max}$	$\leq$ 6%	$\sim$ 3%
$\Delta Q_o/Q_o$	$\leq$ 10%	$\sim$ 1.5% for low field CW measurement $\sim$ 4% for high field pulsed measurement

The errors in temperature determination (which were relatively unimportant for the present measurement and could be neglected for all practical purposes) were typically 1 m°K at 4.2°K and increased monotonically to about 10 m°K at 2.0°K.

3.3 Experimental Results and Discussions

In low temperature experiments for a given lead surface the following quantities of interest were typically measured.

(1) The resonator Q_o as a function of temperature at low field level,

(2) The resonator Q_o as a function of the magnetic field, H_{max}, at two or more different temperatures (typically at 4.2 and 2.2 °K),

(3) The rf critical field, H_c^{rf}, as a function of temperature.

The results are discussed in the following three sections.

3.3.1 Surface Resistance of Superconducting Lead at Low Field Level

The quality factor, Q_o, of the resonator was measured as a function of the helium bath temperature, T , below 4.2°K. A typical rf magnetic field level in the resonator during this measurement was kept

below 5 gauss* which is less than 1% of the thermodynamic critical field of lead at these temperatures. The surface resistance, $R_{exp}(T)$, is related to Q_o by Eq. (3.7) as

$$R_{exp}(T) = \Gamma/Q_o(T) \tag{3.21}$$

where Γ is the geometrical factor defined previously and is 7.00 for this resonator. The error in the absolute determination of R_{exp} was estimated to be less than 10% and the relative error at different temperatures was less than 1.5%.

The following expression was used to analyze the temperature dependence of the surface resistance:

$$R(T) = \frac{A'}{T} e^{-\Delta(T)/kT} + R_{res} \qquad (T/T_c \lesssim 0.5)$$

$$= R_{BCS}(T) + R_{res} \tag{3.22}$$

where the first term is the BCS surface resistance (Eq. (2.8)) discussed in Chapter 2. Here $\Delta(T)$ is the temperature dependent gap parameter and R_{res} is a constant term to describe the residual surface resistance due to nonsuperconducting loss mechanisms. The temperature dependent gap parameter can be approximated by (S2)

$$\Delta(T)/\Delta(0) = [\cos(\pi t^2/2)]^{1/2}$$

$$\equiv \delta(t) \tag{3.23}$$

---

*At this field level nonlinear behavior in Q_o to be described in the next section was never observed.

where t is the reduced temperature T/T_c. Using the above expression for $\Delta(T)$ we have

$$R(T) = \frac{A}{t} e^{-\frac{\Delta(0)}{kT_c}\frac{\delta(t)}{t}} + R_{res} \qquad (3.24)$$

Then a set of experimental data $(R_{exp}(T),T)$ was fitted to the above equation by a least-squares fit with three adjustable parameters: A, $\Delta(0)/kT_c$ and R_{res}. A typical data set, together with the result of the fit, is shown in Fig. 3.6. The three parameters thus obtained are compared with the existing calculations and previous measurements as follows.

BCS Surface Resistance at 4.2°K (A and $\Delta(0)/kT_c$)

Based on the BCS theory the surface resistance of lead was numerically evaluated by Halbritter (H5) as a function of frequency for two different mean free paths of the electrons. His results show a weak dependence on the mean free path, ℓ , and the values he obtained at 205 MHz were

$$R(4.2°K) = 2.8\times10^{-8}\Omega \quad \text{for} \quad \ell = 10^{3}\text{Å}$$

and

$$4.3\times10^{-8}\Omega \quad \text{for} \quad \ell = 10^{5}\text{Å}$$

The mean free path of the present surfaces was estimated to be typically $(1.02\text{-}1.29)\times10^{4}$Å on the basis of their normal state surface resistance measurements (between 7.2 and 10°K). Thus, interpolating* the calculated

*The approximate functional dependence of the surface resistance on the mean free path is logarithmic when ℓ is such that $0.01 \lesssim \xi_0/\ell \lesssim 1.0$ where ξ is the coherence length. Since ξ_0 = 1130Å for lead, this condition is satisfied (H5).

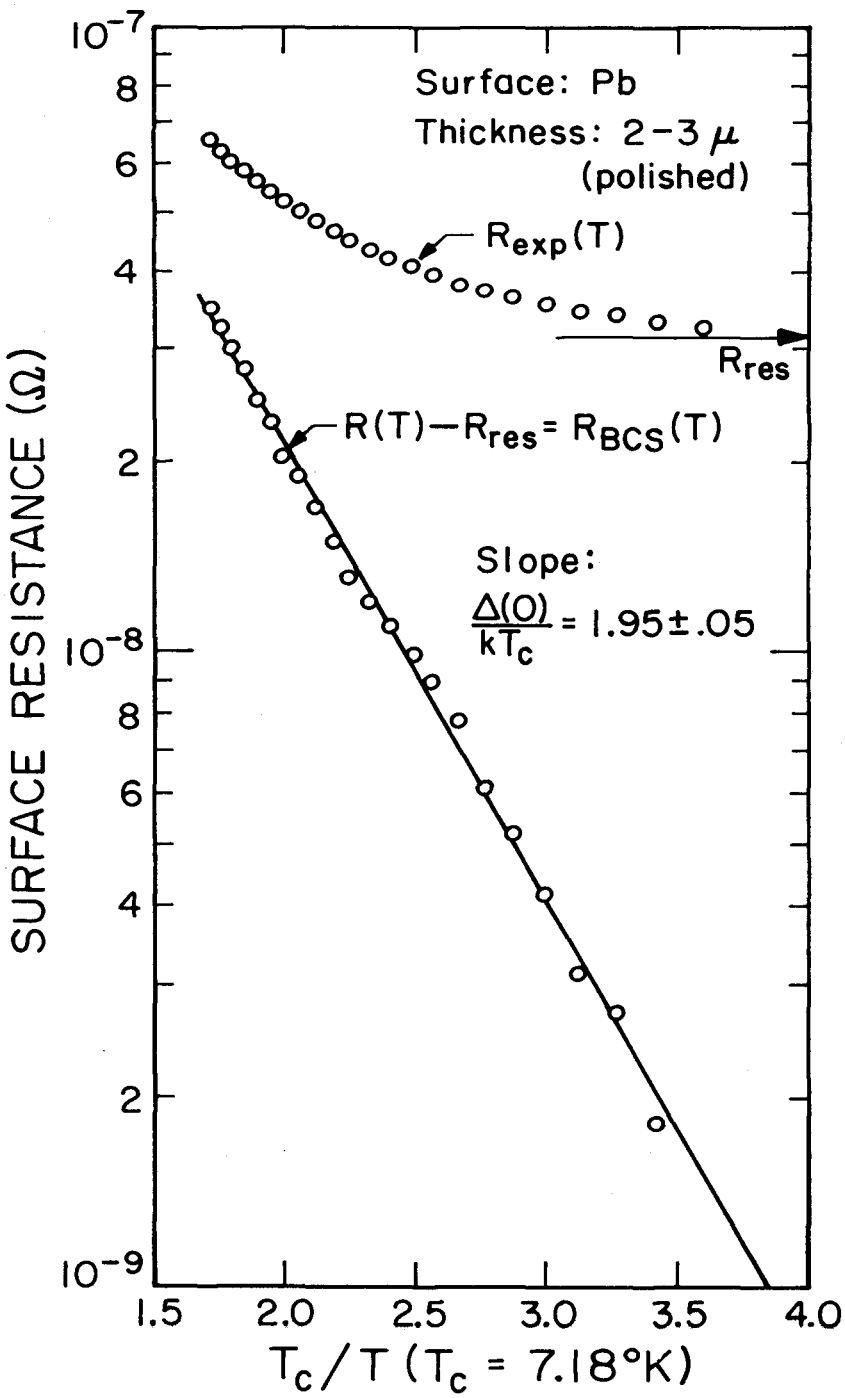

Fig. 3.6 The surface resistance data, $R_{exp}(T)$ (the upper circles), are shown as a function of the inverse reduced temperature. After subtracting a constant residual term, R_{res}, the result of a least-squares fit to $R_{exp}(T)$ is shown by the solid line (R_{BCS}) together with $R_{exp}(T)$ - R_{res}(the lower circles).

surface resistance for the estimated mean free path, we obtain

$$R(4.2°K) = 3.6 \times 10^{-8}\Omega \qquad \text{for} \quad \ell \simeq 10^4 \text{ Å}$$

which compares very well with the present value of

$$R(T) - R_{res} = \frac{A}{t} \exp -\left[\frac{\Delta(0)}{kT_c} \frac{\delta(t)}{t}\right] \Bigg|_{t=0.58}$$

$$= (3.47 \pm 0.17) \times 10^{-8}\Omega$$

where A and $\Delta(0)/kT_c$ were determined by the fit. Considering the uncertainties in material parameters that go into the numerical calculation, this good agreement may be somewhat fortuitous.

Energy Gap at 0°K ($\Delta(0)/kT_c$)

In the BCS theory of superconductivity, the ratio of the energy gap at 0°K to the transition temperature, $\Delta(0)/kT_c$, is a universal constant given by (B1)

$$\Delta(0)/kT_c = 1.75$$

This value depends on their assumption of a weak electron-phonon interaction. However, a number of superconducting elements such as lead and mercury were found to have a stronger electron-phonon interaction, giving rise to a higher value of $\Delta(0)/kT_c$ than the above. They are thus called the strong coupling superconductors.

In this study the ratio for lead was found to be

$$\Delta(0)/kT_c = 1.95 \pm .05$$

as shown in Fig. 3.6. This value is well within the range of values determined previously by different experimental techniques, some of which are summarized below (taken from H7)

Method	$\Delta(0)/kT_c$
Microwave absorption	2.03 - 2.13
Infrared transmission	2.0
Infrared absorption	2.05 - 2.19
Tunneling	2.09 - 2.19
Ultrasonic absorption	1.8
Thermodynamic measurement	1.98

A typical value of $\Delta(0)/kT_c$ deduced from the surface resistance measurement made in the GHz region is (H5)

$$\Delta(0)/kT_c = 2.05 \pm .05$$

which is about 5% higher than the present result. This discrepancy is on the borderline of the experimental error and it could have been caused by a relatively large value of R_{res} which becomes increasingly difficult to avoid at lower frequencies such as used in the present investigation.

Residual Surface Resistance (R_{res})

The observed residual surface resistance, R_{res}, varied from surface to surface and typically it was in the range

$$2 \times 10^{-8} \leq R_{res} \leq 5 \times 10^{-8} \Omega$$

which is comparable in magnitude to the BCS surface resistance at 4.2°K. Although we do not yet understand all the residual loss mechanisms that may be involved, estimates can be made for particular types of loss mechanisms which are discussed in Sec. 2.1.4 (the dielectric loss, the trapped flux loss, and the acoustic phonon generation loss).

An estimate for the dielectric loss was made from the result of an independent measurement made by J. R. Delayen in the Caltech laboratory on a similarly prepared lead surface in a highly re-entrant resonator (D1). In such a cavity the quality factor was found to be limited by a thin dielectric layer on the surface (T1). If the dissipation due to the presence of the dielectric layer is properly scaled to give an equivalent surface resistance, R_ε, in the coaxial resonator used in this study, we obtain

$$R_\varepsilon \simeq 3 \times 10^{-8} \Omega$$

which is in the range of the observed residual surface resistance.

The residual resistance may also be caused by trapped flux if a cavity is cooled through its transition temperature in the presence of a static magnetic field. Since the shielding of the earth's magnetic field in an experimental space is not always complete, the surface resistance due to trapped flux, R_H, is of some practical importance and it was studied in some detail in the course of this investigation (see Appendix A). The results show that the typical R_H for the surfaces under investigation is given by

$$R_H(t) = 1.13 \times 10^{-7} \left(\frac{H_{dc}}{1 - t^2}\right)^{3/2} \Omega \quad \text{for} \quad H_{dc} \lesssim 2 \text{ gauss}$$

where H_{dc} is the static magnetic field present during cooling and is expressed in gauss. The remnant magnetic field in the present experimental space was measured to be less than 15 milligauss so that

$$R_H(t) \leq 2 \times 10^{-10} \Omega$$

which is much too small compared with the observed residual resistance.

Another possible source of residual resistance is due to the acoustic phonon generation. A previous theoretical estimate (P8) gives for lead at 205 MHz

$$R_{phonon} \simeq 1 \times 10^{-8} \Omega$$

which may explain a part of the observed residual resistance.

In summary, the above estimates suggest that the major fraction of R_{res} comes from the dielectric loss caused by a layer of dielectric on the surface of the electroplated lead. Also the phonon generation may account for a part of the residual surface resistance.

3.3.2 Surface Resistance at High RF Magnetic Field

In the application of superconducting resonators to the production of high electromagnetic field levels, the surface resistance at high rf magnetic field is of practical importance, since it is one of the main parameters that determine the power dissipation in a low temperature bath. Although a considerable amount of previous work has gone into improving the performance of superconducting resonators at high power

levels, our basic understanding of the surface resistance at high magnetic field is still very limited both theoretically and experimentally. The main reason for our lack of theoretical understanding is that the perturbation approach, such as used in the Mattis and Bardeen formulation of surface resistance, is not adequate when the rf magnetic field becomes comparable to the thermodynamic critical field. Experimentally, the difficulty lies in the fact that even a very small number of surface defects, when normal, can greatly enhance the average surface resistance, since the surface resistance typically changes by more than four orders of magnitude in going from the superconducting to the normal state.

In the present investigation the surface resistance of lead was studied also for the situation when the rf magnetic field amplitude was comparable to the thermodynamic critical field. The resonator Q_o was measured as a function of the rf magnetic field level. A typical example of the reciprocal of Q_o, which is proportional to the surface resistance, as a function of the rf magnetic field level within the resonator is shown in Fig. 3.7. The main features that can be noted in this figure are as follows.

(1) The surface resistance rises slowly below a certain field level which, for convenience, we call H_{tr} ("tr" for transition from one behavior to another).

(2) Above H_{tr} the surface resistance rises very sharply, particularly near the thermodynamic critical field, H_c (shown by an arrow in the figure.)

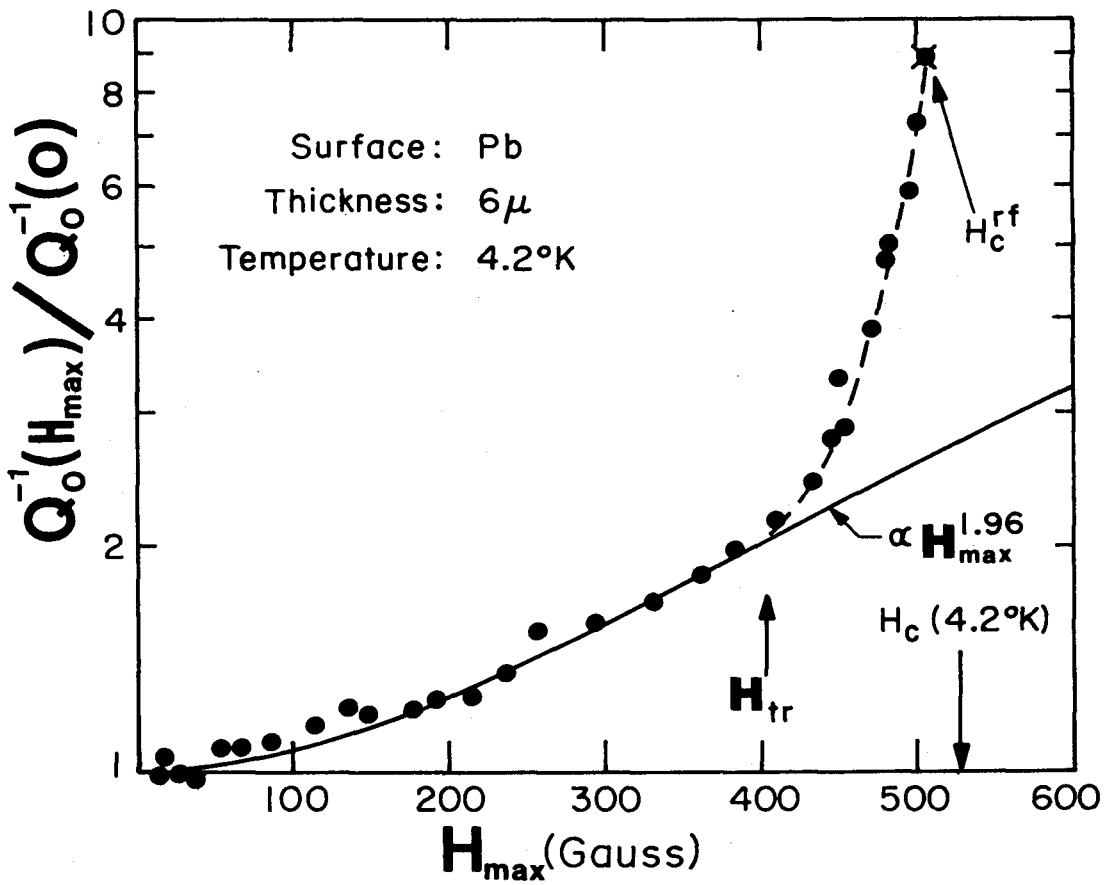

Fig. 3.7 A typical example of the reciprocal of Q_o, normalized to its low field value, is shown as a function of the magnetic field, H_{max}, at the constricted section of the center conductor. The solid line shows a fit of the form aH_{max}^n to the experimental data below the transition field, H_{tr}.

In order to find the possible causes of the above behavior, the surface resistance as a function of the field level was studied for lead surface thicknesses ranging from 0.3 to 14 microns. The details of this study are given in Appendix B. All the observations made in this study point to the following conclusions:

1) There is a field at which the increase in surface resistance changes its character. We call this field H_{tr} and it was observed for all the surfaces examined.

2) Below H_{tr} the increase in surface resistance is approximately proportional to the square of the rf field level. This portion of the increase in surface resistance seems to be caused by heating at localized defects.

3) Above H_{tr} surface structures of the electroplated lead surface (protrusions and spikes) are most likely to be responsible for the sharp rise in the dissipation. Also this rise was found to be approximately exponential in the magnetic field level.

These conclusions are necessarily qualitative because of the practical complications involved in the experiment, such as surface structures of the lead surface and a heating effect. In view of the experimental difficulties, as well as the absence of any reasonable theory for comparison, this topic is still largely an open question. More work will be necessary to determine the intrinsic dependence of surface resistance upon rf magnetic field.

3.3.3 RF Critical Magnetic Field of Lead at 205 MHz

As the resonator is driven to a higher field level, eventually a point is reached where a small fraction of surface area is driven normal. Owing to the increased joule dissipation within such an area, once it is created the normal area quickly spreads by heating the surrounding area above the transition temperature. This process shows itself as a sudden reduction in the resonator Q_0 on a time scale much shorter than the characteristic decay time of the superconducting resonator. This entire process is generally called the "magnetic-thermal breakdown" and the field at which this process is initiated is called the breakdown field or the rf critical magnetic field.

For the present half-wave resonator this breakdown process was observed to be initiated at a well defined field level where the resonator Q_0 decreased typically by a factor of 100 or more within about 10 microseconds. The resultant Q_0 after the breakdown was found to be such that the entire constricted section of the center conductor (see Fig. 3.1) was normal conducting.

All the measurements at high field levels were obtained by pulsing the incident power so as to avoid an excessive heating of the cavity surface. Consequently the field level within the resonator responds in time as shown in Fig. 3.8a, where the breakdown process can be seen as a break in the slope of the field level within the resonator, followed by a steep negative slope. The surface resistance just prior to the breakdown was found to be equivalent to approximately 1-3% of the area of the constricted section of the center conductor being normal.

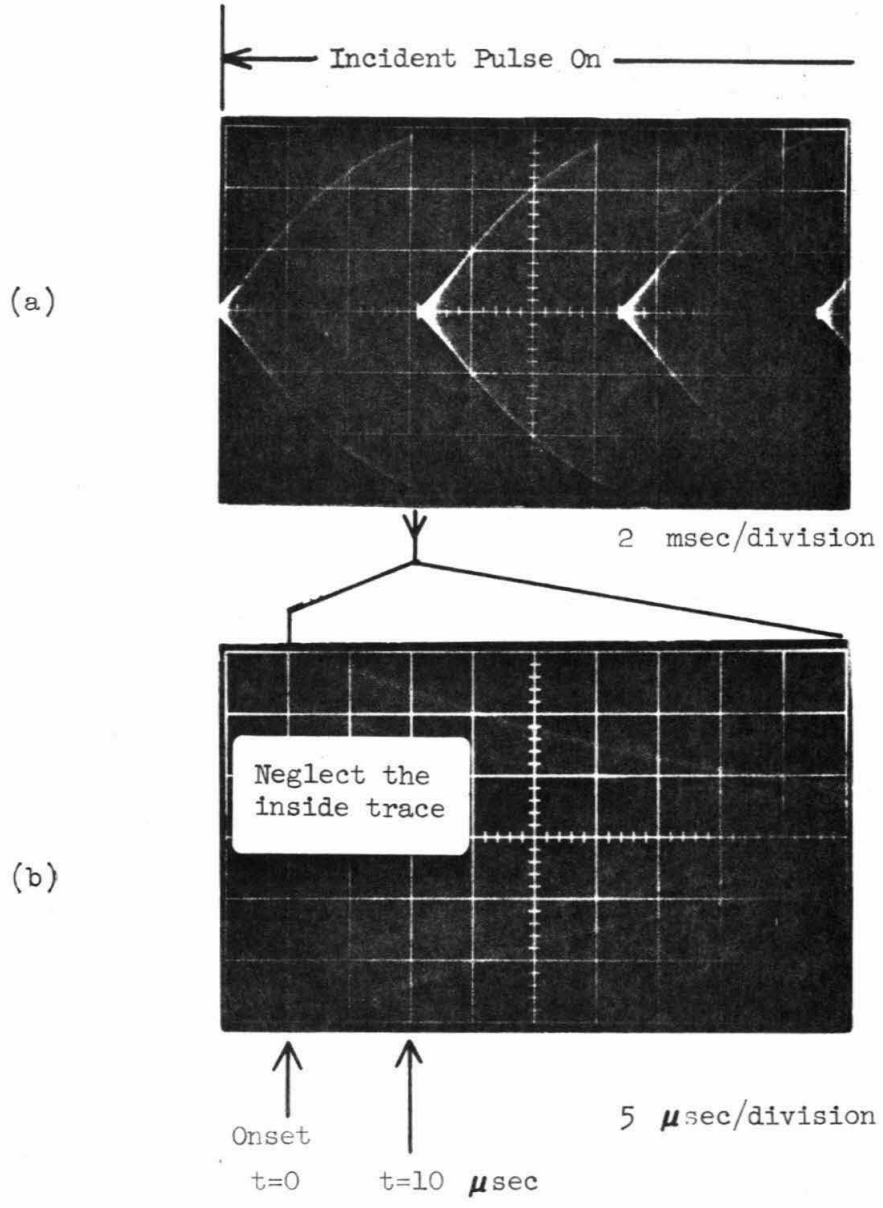

Vertical Scale: 655 Gauss Full Scale for both (a) and (b)

Data: 0.3 micron Pb Surface at 4.2 ^{o}K

Fig. 3.8 The envelope of the rf field level within the resonator is shown as seen on an oscilloscope. (a) When the incident power is kept constant the field level within the resonator reaches the breakdown field at which all the stored energy is dissipated quickly and the entire process repeats itself. (b) The cavity field level immediately following the onset of breakdown on a much finer time scale than in (a).

Once the transition is initiated, the normal region spreads by thermally driving the surrounding area normal at the expense of the energy stored in the cavity. Thus by measuring the cavity Q_o as a function of time, it was possible to infer how much area was being driven normal at any instant of time following the initiation of the breakdown. To do so we look at the time dependent Q_o of the cavity (Eqs. (3.8) and (3.9))*

$$Q_o(t) = \omega \frac{W(t)}{P_{net}(t) - dW(t)/dt} \tag{3.25}$$

where ω is the resonant frequency, W(t) is the total energy content of the cavity, and $P_{net}(t)$ is the net power flowing into the cavity. Here all the quantities are assumed to have been averaged over an rf period as before.

In the photographs of Fig. 3.8 the envelope of the rf voltage at the pickup probe is shown, and this voltage is proportional to $(W(t))^{1/2}$ (see Eq. (3.10)). So the cavity $Q_o(t)$ in the above equation can be determined by measuring the pickup voltage as a function of time on such photographs as shown in Fig. 3.8b. $P_{net}(t)$ can also be measured in the same manner.

When the field level reaches the critical field, we have dW/dt=0 (this is just an operational definition of the rf critical field in the present measurement). Once the breakdown is initiated dW/dt in the denominator of Eq. (3.25) takes over P_{net} rapidly, and in a short time

---

*Assuming that the pickup probe is weakly coupled. For all measurements of this type the power picked up was much less than 1% of P_{net} or dW/dt.

($\sim$ 10μsec) the cavity Q_o attains the value corresponding to the situation where the constricted section of the center conductor is normal conducting. The asymptotic approach to this Q_o value is shown as a function of time in Fig. 3.9. Since the high field region is well localized within the constricted section which is thermally "anchored" to the massive tapered section, the normal region does not spread beyond the edge of the constricted section.

The rf critical field, $H_c^{rf}(T)$, was measured for electroplated lead films of different thicknesses (0,3, 1.45, 6.0 and 14 microns) at different temperatures. The results are shown in Fig. 3.10 for two temperatures where H_c^{rf} is shown as a function of the incident power, P_{inc}, used to drive the resonator. By increasing the incident power, the time needed to reach a given field level could be shortened, thus minimizing the possibility of heating the entire wall of the resonator.

As can be seen in the figure, H_c^{rf} was found to depend on both the incident power and on the thickness of the plated layer. The dependence on the incident power is relatively small compared with the dependence on the thickness and could have been caused by a localized heating of the lead surface where the initial normal area was nucleated. From the observed change in H_c^{rf} as a function of P_{inc} and the temperature dependence of H_c^{rf}, we can estimate the temperature rise, due to such local heating at the nucleation site, to be 0.35°K for 6 and 14 micron surfaces and 0.10°K for 0.3 micron film, in the range of P_{inc} used in the measurement. Thus it is relatively unimportant for thinner films.

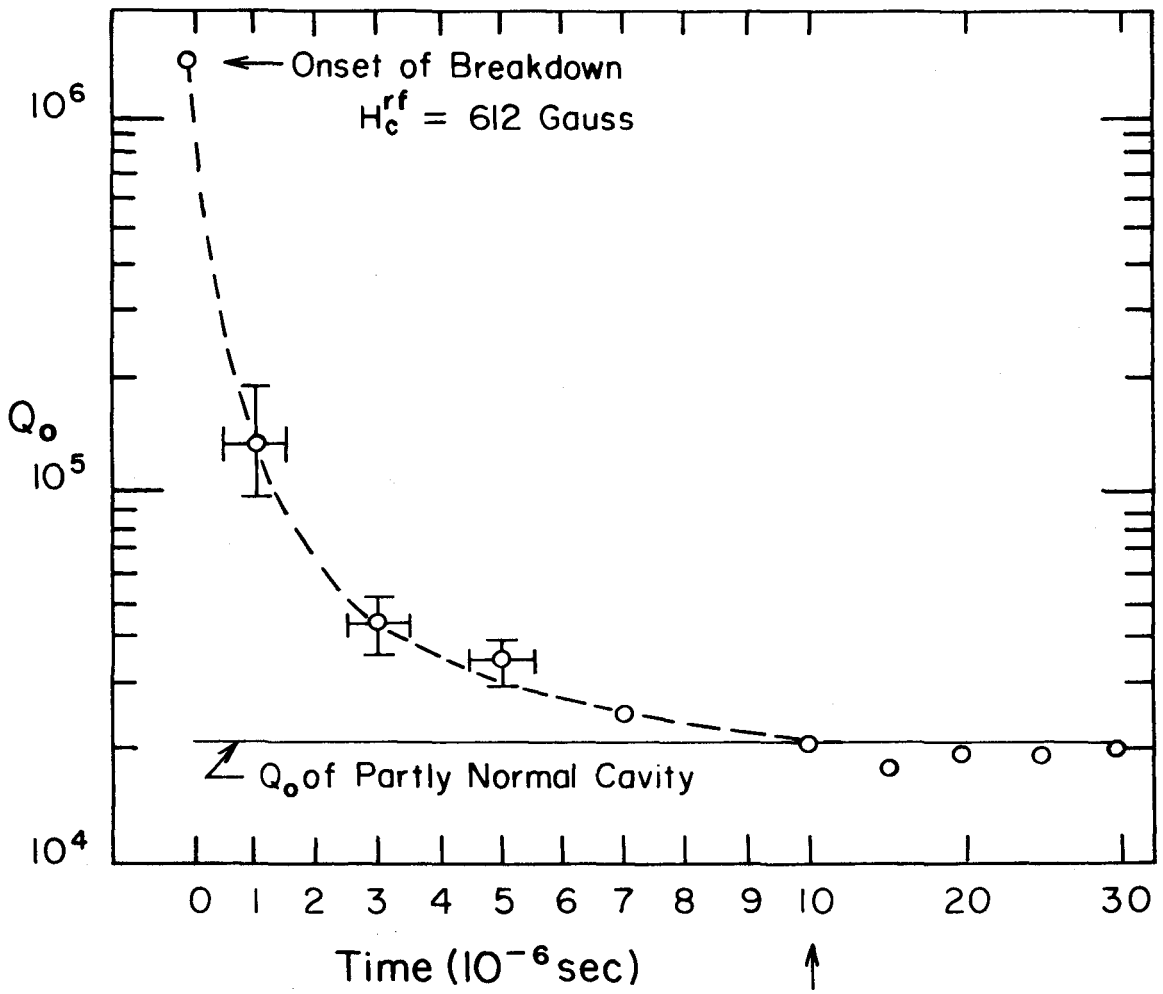

Fig. 3.9 The resonator Q is shown as a function of time immediately following the onset of breakdown. The resonator Q_o decreases until the entire constricted section becomes normal. Note the change in time scale at 10 μsec.

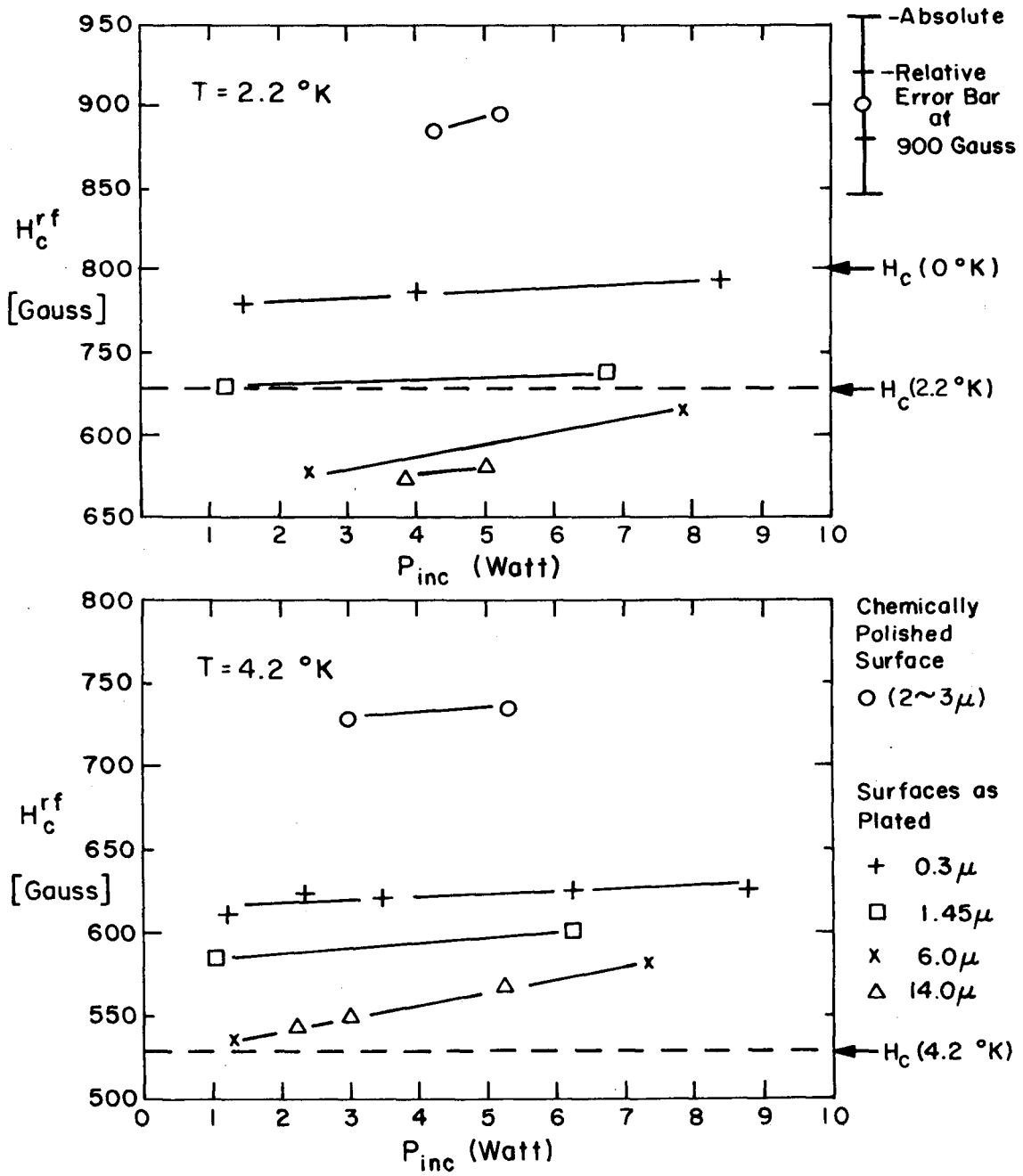

Fig. 3.10 The critical rf magnetic field, H_c^{rf}, is shown as a function of the incident power used to drive the half-wave resonator. The measurements were made for various thicknesses of lead layer. The highest fields were attained for a surface prepared by chemical polish method (see text).

On the other hand, the dependence of H_c^{rf} on the thickness of the lead film was more pronounced, increasing as the thickness decreased. This dependence was attributed to the surface structures on the lead surface (protrusions and sharp corners of the crystal grains of lead) which tended to develop as the thickness of the electroplated layer was increased.* Since the surface magnetic field could be locally enhanced at such surface structures, the field at which the initial normal area was created would be lower for the surfaces with more surface structures, i.e., for thicker films.

The above interpretation was later verified when a new surface preparation technique involving a chemical polishing of the lead surface to remove the surface structures was developed in this laboratory.** The lead surface prepared in this manner was found to have superior field emission properties compared with ordinary electroplated surfaces (D1)***, which indicated that there were many fewer sharp corners and spikes. The corresponding rf critical fields were improved by a significant amount as can be seen in Fig. 3.10, where the highest H_c^{rf} at a given temperature was obtained for a chemically polished surface.

---

*This point is also discussed in Appendix B.

**This preparation technique was developed by G. J. Dick in the low temperature physics group at Caltech.

***The surface electric field at which field emission electron loading began was improved from 15 MV/m to above 25 MV/m by this preparation (D1).

As discussed in Sec. 2.2.4, there is a possibility of magnetic superheating in the transition from the superconducting-to-normal state in rf magnetic fields, i.e., the superconducting surface can remain in a metastable Meissner state above the thermodynamic critical field. Throughout the present study for lead, various amounts of superheating were observed. In Fig. 3.10 the thermodynamic critical fields at the respective temperatures are shown by the dashed lines. For example, at 4.2°K the rf magnetic field could be as high as 40% above the thermodynamic critical field.

In order to study further this rf superheating behavior in lead, the rf critical fields were measured between 2.2°K and T_c. The results were then compared with the expected superheating field deduced in the following manner. As discussed in Sec. 2.2.3, the superheating field was previously evaluated (M5) as a function of the GL parameter (see Fig. 2.1). Smith et al. (S6) experimentally determined the GL parameter, κ , of lead by the observation of supercooling.* They found that the κ for lead varied from 0.515 at 0°K to 0.240 at T_c, and can be expressed by the empirical relation

$$\kappa(t) = 0.514 - 0.274\ t^2 \qquad \text{for Pb}$$

where t is the reduced temperature.

Then, combining the above GL parameter for lead and the results of the one-dimensional GL theory, we obtain the expected superheating

*The (magnetic) supercooling is a persistence of the normal state below the thermodynamic critical field in a decreasing magnetic field. Experimentally it has been found to be readily observable, in contrast to the case of superheating. Supercooling was also analyzed theoretically by Ginzburg (G4).

field, h_{sh}, as a function of temperature. This field and the measured rf critical field are shown in Fig. 3.11 where both fields are normalized by the thermodynamic critical field, i.e., h_{sh} $(=H_{sh}/H_c)$ and $h_c^{rf} = (H_c^{rf}/H_c)$.*

In this figure, the rf critical field can be seen to have a very similar but somewhat stronger temperature dependence than the superheating field. The rf critical field tends to approach the superheating field at higher temperatures (near T_c, however, the errors in h_c^{rf} due to uncertainty in the temperature determination make the absolute comparison between h_c^{rf} and h_{sh} difficult). The experimental observation of the expected superheating in dc field for lead has been found to be generally difficult, presumably due to surface defects** which would ease the nucleation of the normal phase. The present behavior of h_c^{rf} may have been caused by the flaws on the surface of the electroplated lead such as grain boundaries and surface structures, which lowers the field at which the normal phase is nucleated. Also, there is a possibility that the nucleation of the normal phase in different dimensional forms (to be discussed fully in Chapter 4) gives rise to a stronger temperature dependence of h_c^{rf} compared with h_{sh}. (In the language of Chapter 4, the present rf results for lead fall between the plane nucleation field and the line nucleation field.)

All the high field measurements were performed by pulsing the

---

*In the normalization of the rf critical field, the form $H_c(T) = H_0(1-(T/T_c)^2)$, was used, together with the accepted values of $H_0 = 803$ gauss and $T_c = 7.18°K$.

**H. Parr (private communication). Even when the superheating fields in lead were observed (S6,S7), they tended to have somewhat erratic temperature dependence at lower temperatures.

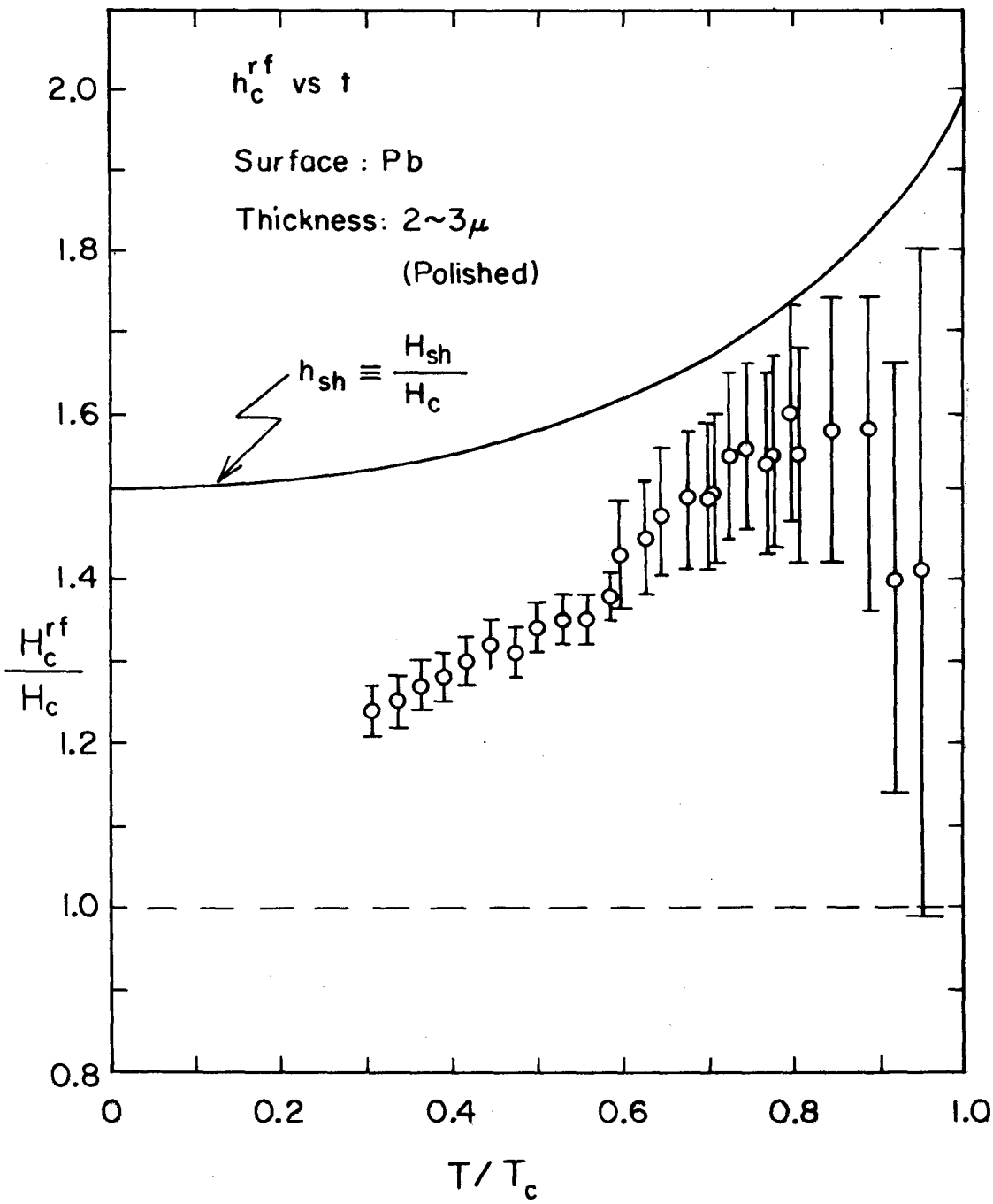

Fig. 3.11 The measured rf reduced critical fields of lead are shown as a function of reduced temperature. The solid curve shows the expected superheating field deduced from the temperature dependence of the Ginzburg-Landau parameter of lead measured by Smith et al. (S1).

incident power flowing into the cavity. Below 4.2°K the temperature was fixed by regulating the helium bath temperature. Above 4.2°K no such regulation was available and the resonator was freely warmed up at the rate of approximately 0.35°K/hr. Since typical critical field data could be obtained in less than 5 min, the temperature drift during the measurement was kept below 30 m°K. The temperature of the resonator above 4.2°K was determined by two carbon-resistor thermometers* located at the top and bottom of the outer conductor. The two thermometers generally indicated the temperature within 50 m°K so their average value was used as the temperature of the resonator. Overall error in temperature above 4.2°K was then estimated to be less than 0.1°K, which did not give rise to an excessive error except very close to the transition temperature as may be seen in Fig. 3.11.

The error in temperature may also be caused by the heat dissipation from the power density involved in driving the resonator at high magnetic field. The rise in temperature of the cavity surface due to heat dissipation was estimated under a simplifying assumption that the high field region of the resonator (constricted section of the center conductor) was thermally anchored to the massive adjoining section (tapered section). Then using the thermal conductivity of OFHC copper** and the measured power dissipation, the temperature rise was estimated to be less than 0.5°K at 2.2°K and less than 0.2°K at 4.2°K and above.

---

*Allen-Bradley carbon composite resistors, 100Ω, 1/10 Watt.

**Thermal conductivity was estimated from the measured electrical resistivity of the OFHC copper by using the Wiedemann-Franz law. The resistivity ratio of copper was 63.

The errors in reduced rf critical fields due to these temperature rises were relatively insignificant in the representation of Fig. 3.11.

3.4 Conclusions

The surface resistance and the rf critical magnetic field of lead electroplated on copper were studied at 205 MHz in a half-wave coaxial resonator. The observed surface resistance at low field level could be well described by the BCS surface resistance with the addition of a temperature independent residual resistance, R_{res}. Good agreement was found between the present result and the result of previous numerical calculation, once R_{res} was subtracted. The sources of R_{res} are not all known but the available experimental data and other estimates suggest that the major fraction of R_{res} in the present experiment was due to the presence of an oxide layer on the surface.

At higher rf magnetic field levels the surface resistance was found to depend heavily on the surface condition of the electroplated layer, which made it difficult to determine the intrinsic dependence of the surface resistance on the rf magnetic field.

The attainable rf critical magnetic field of lead was found to be limited not by the thermodynamic critical field, but rather by the superheating field predicted by the one-dimensional Ginzburg-Landau theory. The observed rf critical field was very close to the superheating field but showed somewhat stronger temperature dependence than the superheating field.

Chapter IV

RF CRITICAL FIELD OF SN-IN AND IN-BI ALLOYS AT 90 and 300 MHz

4.1 Introduction and Description of Overall Scheme

In Chapter 3 it was found that the rf critical field of lead at 205 MHz approached the superheating field but was always somewhat smaller, particularly at lower temperatures. The disadvantages of working with lead were:

(1) It was not possible to make accurate measurements near T_c (7.18°K) where the GL theory was presumably more valid and comparison between experiment and theory more meaningful.

(2) The dc critical field of the same cavity surface could not be directly determined because of its geometry.

(3) Due to the high field level involved, it was necessary to use relatively high power which might have raised the temperature of the cavity surface making the exact temperature somewhat uncertain.

Thus alternative schemes were sought by which we could look at the rf critical field of superconductors and its relation to other critical fields, particularly the superheating field, while avoiding the above-mentioned difficulties for lead. Since the superheating is caused mainly by the boundary energy which is a function of the Ginzburgh-Landau parameter, κ , and which changes quite drastically in the low κ range (see Fig. 2.1), it is desirable to measure the rf critical field over a range of κ .

It is well established that the κ of a superconductor can be changed by alloying since the reduction in the mean free path of the electrons causes changes in the penetration depth and coherence length in such a way as to increase $\kappa (\equiv \lambda/\xi)$. Thus by starting with a pure metal which is an extreme type I superconductor, we can obtain a series of alloys which span a range of κ. After looking into several possible metals and their alloy combinations, it was eventually decided that two alloy systems, tin-indium and indium-bismuth, be used. Some of the considerations that dictated the above choices were:

(1) The transition temperature, T_c, should be lower than 4.2°K (normal boiling point of helium) so that it would be possible to work near T_c.

(2) The magnetic properties in the dc field should be reasonably well known so that results obtained by relatively simple dc measurements could be checked against previous measurements.

(3) Forms of the samples should be such that both dc and rf measurements could be made on the same set of samples.

(4) A reasonable range of κ should be available.

These requirements were satisfied by the above alloys as listed below.

Alloy System	κ Range	T_c Range
SnIn	.09 - 1.0	3.7 - 3.6°K
InBi	.06 - 1.8	3.4 - 4.4°K

It should be noted that the systems span a κ range in both type I and type II regimes. A range of κ was duplicated in order to be able to discern possible anomalies, if any, of a particular system.

Both the dc and rf critical fields were measured for direct comparison on spherical samples prepared from these alloys, whereas the GL parameter was determined independently by measuring the resistivity of cylindrical samples of the same set of alloys. The results show that the measured rf critical field near T_c agrees very closely with the superheating field as predicted by the one-dimensional GL theory.

4.2 Experimental Method

For both alloys, concentration ranges were chosen so that the resultant alloys were homogeneous solid solutions of one metal in another. This range was 0-6 at.% of In in Sn (B5) and 0-4 at.% of Bi in In (H12). About ten alloys were made for each system within these concentration ranges. The entire experiment consisted of three major stages: sample preparation, measurements in dc field, and measurements in rf field. They are discussed in the following four sections.

4.2.1 Sample Preparation

Starting metals* were first chemically etched to remove the surface oxide. For each concentration, appropriate quantities of each metal were weighed out on a microbalance. They were then combined in a hot bath of glycerin contained in a glass test tube. Once molten, the metal was thoroughly mixed using a glass rod. Then samples were prepared in two shapes: spheres and cylinders.

---

*Indium (5N purity, 1/8-in. dia. wire, supplied by Indium Corporation of America, New York.)
Tin (5N purity, shots, Electronic Space Products, Inc., Los Angeles)
Bismuth (6N purity, ingot, Electronic Space Products, Inc., Los Angeles)

Spherical Samples. The molten metal was withdrawn by suction into one end of a long and thick-walled glass capillary tube. Once the desired amount of metal was within the capillary, the glass tube was taken out of the glycerin bath. When the molten metal was ejected slowly out of the capillary tube and allowed to fall about 3 cm into a bath of cold glycerin (at room temperature), the metal formed a sphere under its own surface tension and retained the spherical shape as it froze in falling through the cold glycerin. The sample formed this way was spherical within about 5% of its mean radius. The surface was generally smooth except at the top end where the last stage of solidification took place, showing either a concave surface or an irregular surface structure. These defects were usually confined within a small area at the pole and their effects were minimized in the measurement by aligning the sample with respect to the applied field direction so that they were in the region of minimum field. The spherical samples were the primary samples on which both dc and rf critical fields were measured. The typical dimension of the spheres was 1-2 mm in diameter.

Cylindrical Samples. For the determination of the GL parameter (to be described in the next section) it was necessary to measure the resistivity of each alloy sample. This was done on a cylindrically shaped sample which was made by a similar method as above. The molten metal was withdrawn by suction into a thin-walled and slightly-tapered glass capillary tube. The metal was allowed to freeze within the tube, which was then broken at the edge to remove the solidified cylindrical sample. The typical sample dimensions were 1 mm in diameter and 2.5 cm in length.

4.2.2 Determination of the GL Parameter by Resistivity

Gor'kov-Goodman Equation. As discussed previously in Sec. 2.2.2, the Ginzburg-Landau parameter, $\kappa (= \lambda/\xi)$, plays an essential role in determining the magnetic properties of a superconductor. When a superconductor is alloyed with an impurity, the mean free path of the electrons is reduced, which in turn reduces the coherence length and increases the penetration depth at the same time. The net effect of alloying, then, is that κ increases with increasing impurity concentration. In the present case the starting metals, tin and indium, are in the extreme type I region ($\kappa = 0.06 - 0.1$). By alloying with indium and bismuth, respectively, they cross the boundary between the type I and type II regions ($\kappa = 1/\sqrt{2}$) and finally κ up to about 1.8 which is well into the type II regime.

The expression for the Ginzburg-Landau parameter of alloys was first derived by Gor'kov (G8) for extreme type II alloys and later generalized by Goodman (G9). It is now known as the Gor'kov-Goodman equation and given simply as

$$\kappa = \kappa_o + \kappa_i$$

$$= \kappa_o + 7.5 \times 10^3 \gamma^{1/2} \rho \qquad (4.1)$$

where the GL parameter, κ, of an alloy at T_c is expressed as a sum of the GL parameter of the pure metal, κ_o, and the change in the parameter due to the alloying, κ_i. κ_i is given in terms of the residual resistivity in the normal state, ρ (ohm-cm), and the Sommerfeld constant for the electronic specific heat, γ (erg/(cm^{3}deg^2)).

The GL parameters of alloys determined by the above equation were found to agree within a few percent with those obtained from various features of the magnetization curves near T_c (K4)* for InBi alloys of the same composition range as used in the present study.

Resistivity Measurement. The residual resistivity of cylindrical samples of alloys was measured between 4.2°K and the transition temperature by a conventional 4-point probe measurement with a lock-in amplifier as a detector. Initially, all the alloy samples, except the most dilute ones, were found to have a broadened transition temperature, indicating inhomogeneity within the sample. Thus, they were subsequently annealed at 5-10°C below their melting temperature (solidus temperature) for 20-100 hrs, depending on their concentration.** After the annealing treatment the alloy samples showed, generally, a well-defined transition temperature above which the resistance was constant up to 4.2°K (the width of T_c will be discussed in the next section in connection with the T_c of the spherical samples). For those samples with T_c above 4.2°K (two samples at the high concentration end of InBi alloys) the resistivity was measured while the sample was driven normal by an applied magnetic field.

---

*Kinsel et al. (K4) assumed $\kappa = 0.112$ for indium from the supercooling result of Faber (F5). However, the supercooling field was later shown to be given by H_{c3} rather than H_{c2} (S8). So their value of κ should be modified to $\kappa = 0.066$. This does not change their results by more than 6%.

**Spherical samples of the same concentration were annealed at the same time as the cylindrical samples.

The GL parameters of pure samples of tin and indium could not be determined by resistivity measurements. However, for both metals, previous κ_0 values were measured to be in the extreme type I region. The typical values of κ_0 determined by supercooling observations (S7) are

$\kappa_0 = 0.087$ for tin

$\kappa_0 = 0.060$ for indium

The GL parameters of the present alloys were then evaluated using the above values of κ_0 and the measured values of resistivity. The electronic specific heat constant, γ , of pure tin and indium (B6)* was used in the expression instead of the γ of the alloys.**

The κ values thus determined for the present samples are tabulated in Table 4.1 and compared with previously measured values of κ in Fig. 4.1. Very good agreement was found for SnIn alloys between the present results and the results of Smith et al. (S7) as shown in Fig. 4.1a. For InBi alloys, the values obtained by Kinsel et al. (K4) show a general agreement in Fig. 4.1b. The present results for both alloys show a good linear relationship between κ and the alloy concentration ($\propto \rho$) as expected for dilute alloys.

4.2.3 DC Critical Fields of Tin, Indium and Their Alloys

It was desired that both dc and rf critical fields be measured on the same set of samples for a direct comparison. For this purpose,

---

*$\gamma = 1.80 \pm 0.02$ mJ/(mole deg^2) for Sn and $1.60 \pm .02$ mJ/(mole deg^2) for In.

**Kinsel et al. (K4) found that using the κ values of the alloys did not change the κ values by more than 5% for their InBi alloys.

Table 4.1

The residual resistivities, $\rho(4.2°K)$, of cylindrical samples of SnIn and InBi alloys are shown with the resulting values of the GL parameter, κ , determined from the Gor'kov-Goodman equation. The values of κ_0 obtained by Smith et al. (S7) are assumed. The mean free path of electrons, ℓ , is also listed.

SnIn Alloys

At.% In	ρ(4.2°K) $\mu\Omega$-cm	κ_i (a)	κ (b)	Type	ℓ_0 (c) Å
0	$< 6.82 \times 10^{-3}$	<.002	0.087	I	$> 12 \times 10^4$
0.10	4.34×10^{-2}	0.0108	0.098	I	1.89×10^4
0.20	9.07×10^{-2}	0.0226	0.110	I	9,040
0.27	0.151	0.038	0.125	I	5,430
0.62	0.347	0.086	0.173	I	2,360
1.05	0.642	0.160	0.247	I	1,277
1.74	1.31	0.326	0.413	I	626
2.95	1.84	0.458	0.545	I	446
4.21	2.29	0.570	0.657	I	358
4.96	3.00	0.747	0.834	II	273
6.26	3.65	0.909	0.996	II	225

InBi Alloys

0	3.25×10^{-3}	7.8×10^{-4}	0.060	I	27×10^4
0.25	0.423	0.101	0.161	I	2,100
0.52	0.907	0.217	0.277	I	981
0.99	1.710	0.409	0.469	I	524
1.43	2.38	0.569	0.629	I	374
1.49	2.58	0.617	0.677	I	345
1.63	2.78	0.664	0.724	II	320
1.99	3.36	0.803	0.863	II	299
2.80	4.60	1.099	1.159	II	193
3.42	6.06	1.448	1.508	II	147
3.94	7.08	1.692	1.752	II	126

(a) $\kappa_i = 7.5 \times 10^3 \gamma^{1/2} \rho$ where γ values were taken from (B6).
(b) $\kappa = \kappa_o + \kappa_i$ where κ_o values in (S7) were used.
(c) $\rho\ell = 0.82 \times 10^{-11} \Omega cm^2$ for Sn (S7).
(d) $\rho\ell = 0.89 \times 10^{-11} \Omega cm^2$ for In (B4).

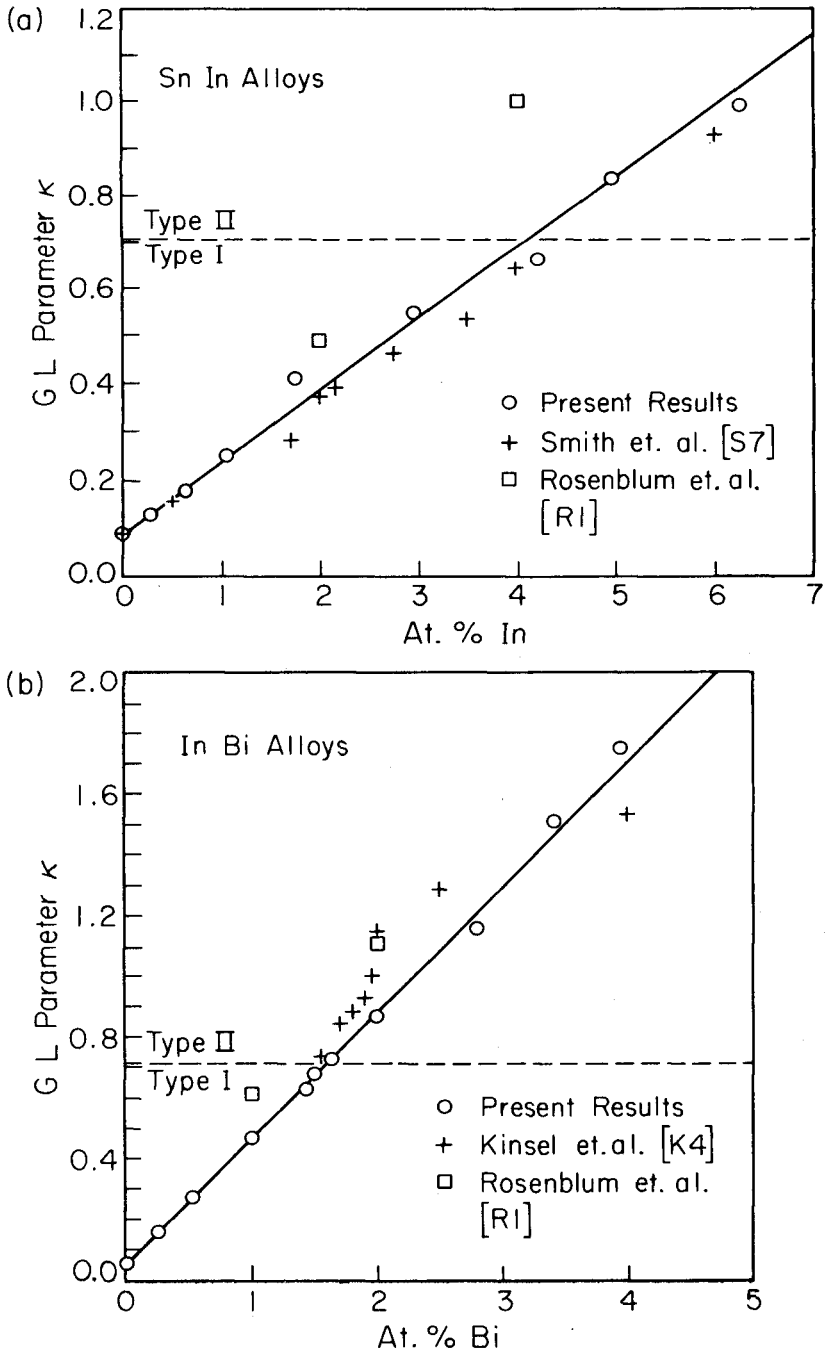

Fig. 4.1 The Ginzburg-Landau parameter (κ) of alloys is shown as a function of the solute concentration. The present values were determined from the Gor'kov-Goodman equation using the measured resistivity of the samples in the normal state. They are compared with previously determined values in the limit of T_c for (a) SnIn alloys by the observation of supercooling (S7), and (b) InBi alloys by resistivity as well as various features of magnetization (K4). The results obtained by surface superconductivity observations in R1 are also shown.

the spherical samples of tin, indium, and their alloys were made as described in Sec. 4.2.1 and annealed in the same manner as the cylindrical samples. The dc critical fields were determined by measuring the low frequency ac susceptibility of the spherical samples in a slowly varying magnetic field.

In this measurement the dc (or slowly varying) magnetic field was applied by a solenoid* located in the liquid nitrogen bath outside the helium dewar as shown in Fig. 4.2 where the experimental arrangement is shown schematically. For the measurement of susceptibility, a small (less than 50 mgauss in amplitude), low frequency (100-1000 Hz) magnetic field was superimposed on the applied magnetic field by means of a drive coil. This ac component was detected and amplified by a phase-sensitive detector (PAR lock-in amplifier). The amplified signal was then displayed as a function of the applied magnetic field on the X-Y recorder.

Typical examples of the susceptibility thus determined are shown in Fig. 4.3 for a pure type I sample (a) and a type II alloy sample (b). Particular features of the transition that have been found to be important in the determination of the bulk critical field are discussed separately for both types. Other susceptibility features involving the surface superconductivity (H_{c3}), upper critical field (H_{c2}), ideal supercooling field (H_{sc}) and ideal superheating field (H_{sh}) are not

---

*The solenoid was wound on a lathe from heavy copper wire. The field was calculated from the known geometry and the field of an approximately infinite solenoid. An overall error in the absolute determination of magnetic field was estimated to be less than 3%.

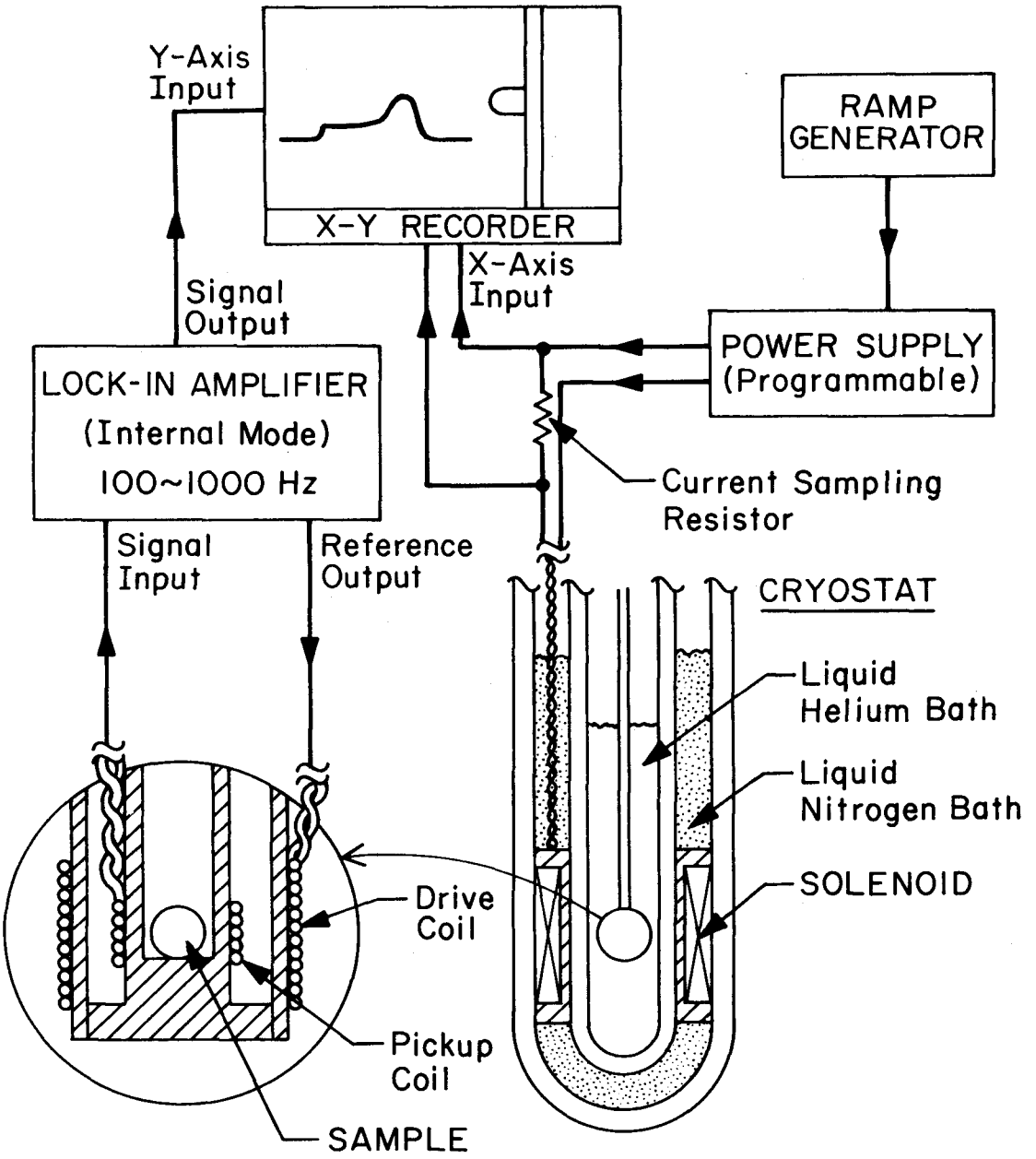

Fig. 4.2 The experimental arrangement for the measurement of low frequency ac susceptibility is shown schematically.

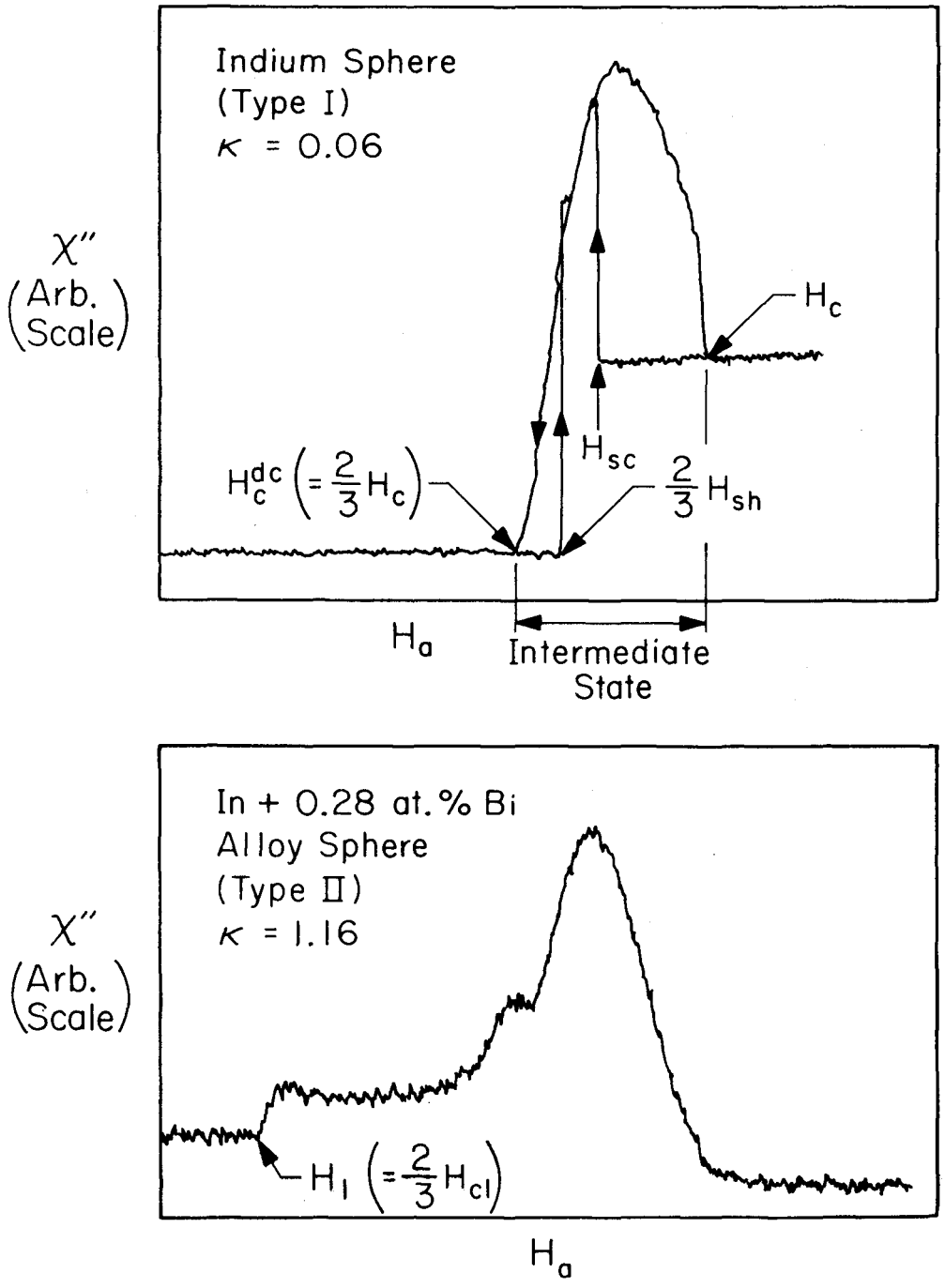

Fig. 4.3 The imaginary component of the low frequency ac susceptibility of a sphere is shown for (a) an indium sphere, and (b) an alloy sphere (κ = 1.16) as a function of the applied magnetic field.

discussed here. Discussions on such characteristics may be found in S7.

Type I Case:

An ideal type I superconducting sphere is expected to remain in the Meissner state up to an applied field, H_a, of $(2/3)H_c$ at which it goes into the intermediate state and does not become completely normal until the applied field is equal to H_c.* In Fig. 4.3a the imaginary component of susceptibility (non-inductive component) for an indium sphere is shown. For pure samples both superheating and supercooling were generally observed to be present to some extent. The extent of these metastabilities depended mostly on the exact condition of the spherical samples. For this particular sample they are shown by arrows as $2/3\ H_{sh}$ (superheating field) in an increasing magnetic field and as H_{sc} (supercooling field) in a decreasing field. However, there was no difficulty in identifying the field at which the intermediate state began, H_c^{dc}(= $2/3\ H_c$ for a perfect sphere), and the field at which the sample became entirely normal, H_c, both of which are shown in the figure. For other type I alloy samples this field (H_c^{dc}) was also well defined since the superheating and supercooling tended to disappear as soon as the pure metals were alloyed.

---

*This is generally known as the demagnetization effect and for simple geometries such as an ellipsoid of revolution, the problem is effectively dealt with by the use of the demagnetization coefficient D . For a sphere D = 1/3 and the field at the equator (polar axis being along the applied field) is given as $H_{eq} = H_a/(1-D) = 1.5\ H_a$ (L3, p.23).

Type II Case:

In an increasing field a type II spherical sample is expected to remain in the Meissner state up to 2/3 H_{c1} at which it goes into the mixed state. For type II alloy samples this field was identified as the first field, H_1, at which there was a distinct change in the imaginary component of the susceptibility in an increasing field. This is shown by an arrow in Fig. 4.3b. The ratio of H_{c1} to H_c was evaluated previously by Harden and Arp (H11) as a function of the GL parameter κ. Thus the bulk critical field of the present spherical samples, H_c^{dc}, can be obtained by using the values of κ determined by the resistivity measurement (preceding section).

For the spherical samples of both types, the susceptibility data were obtained in the reduced temperature range $0.9 \leq t \leq 1.0$.* The resultant critical field, H_c^{dc}, as a function of temperature was fitted to the parabolic expression,

$$H_c^{dc}(T) = H_o^{dc}(1 - (T/T_c)^2)$$

to determine H_o^{dc} and T_c to be used later for the comparison with rf measurements.** The results of the fit showed that the deviation of the

*Extending the measurement down to $t = 0.80$ did not alter significantly the determination of H_o^{dc} and T_c. In the rf measurements, the temperature range of concern was $0.8 \leq t \leq 1.0$.

**The demagnetization effect of the sphere was not included in H_c^{dc}, i.e., the actual critical field would be $H_c = 1.5\ H_c^{dc}$ if the sample was a perfect sphere. Since the rf critical field will be defined in the same way, the demagnetization factor drops out when H_c^{rf} is normalized by H_c^{dc}.

experimental points from the fit was typically within ∿3% and no more than 5% in the worst case. The values of H_o^{dc} and T_c thus obtained are tabulated in Table 4.2. They were found to be in satisfactory agreement with the existing data when available: H_c data for InBi (K4,K6), T_c data for InBi (K4,K6), and T_c data for SnIn (S7,M7).

The transition temperature and its width for the spherical samples were also determined by measuring the inductive component of the susceptibility as the temperature of the sample was reduced. The temperatures at which the transition from the normal to superconducting state were initiated and completed, defined as T_{c2} and T_{c1}, respectively, were determined. The transition width ΔT (= $T_{c2} - T_{c1}$) was found to be reasonably narrow, i.e., typically 2-30 m°K with only a few exceptions. They are also listed in Table 4.2. The transition temperatures determined by the extrapolation of H_c^{dc} data as described in the preceding paragraph were in good agreement with these direct measurements.

4.2.4 RF Measurement

Once the dc properties of the alloy samples were determined and verified against the existing data, the rf measurements were carried out on the spherical samples by using a helical resonator constructed for this purpose as shown in Fig. 4.4. The helical resonator was chosen primarily for two reasons:

(1) It was possible to generate rf magnetic fields which were uniform over the size of the spherical samples.

Table 4.2

The critical field of spherical samples, $H_c^{dc}(T)$, was expressed as $H_c^{dc}\ (1 - (T/T_c)^2)$ where H_0^{dc} and T_c were determined by a least-squares fit. The transition widths, $\Delta T = T_{c2} - T_{c1}$, are also listed where T_{c2} is the onset and T_{c1} the completion of the normal to superconducting transition.

SnIn Alloys

At.% In	κ	$H_c^{dc}(0)$** gauss	T_c^* °K	T_{c_1} °K	T_{c_2} °K	ΔT_c
0	0.087	188 ± 1.4	3.715	3.715	3.717	.002
0.10	0.098	195.5 ± 1.4	3.695	3.695	3.705	.010
0.20	0.110	194.6 ± 1.2	3.685	3.685	3.693	.008
0.27	0.125	188 ± 1.1	3.676	3.676	3.699	.023
0.62	0.173	186 ± 1.3	3.653	3.656	3.693	.037
1.05	0.247	188 ± 1.6	3.643	3.641	3.650	.009
1.74	0.413	182 ± 1.2	3.623	3.625	3.629	.005
2.95	0.55	202 ± 2	3.611	3.608	3.641	.033
4.21	0.66	200 ± 2	3.613	3.614	3.648	.034
4.96	0.83	233 ± 2	3.614	3.614	3.683	.069
6.26	1.00	261 ± 3	3.626	3.610	3.703	.093

InBi Alloys

0	0.06	172 ± 2	3.405	3.404	3.406	.002
0.25	0.16	181 ± 3	3.410	3.408	3.416	.008
0.52	0.28	188 ± 2	3.466	3.463	3.470	.007
0.99	0.47	204 ± 2	3.593	3.586	3.599	.013
1.43	0.63	209 ± 2	3.710	3.703	3.722	.019
1.49	0.68	206 ± 4	3.726	3.720	3.728	.008
1.63	0.72	209 ± 2	3.762	3.780	3.799	.019
1.99	0.86	224 ± 2	3.856	3.835	3.866	.031
2.80	1.16	249 ± 2	4.041	4.022	4.053	.033
3.42	1.51	322 ± 2	4.249	4.236	4.269	.033
3.94	1.75	310 ± 3	4.411	N.A.***	N.A.	N.A.

*Absolute determination of T_c is estimated to be within ± 4 m°K.

**$H_c^{dc}(0) \equiv \frac{2}{3} H_c(0)$ for a perfect sphere.

***Not available.

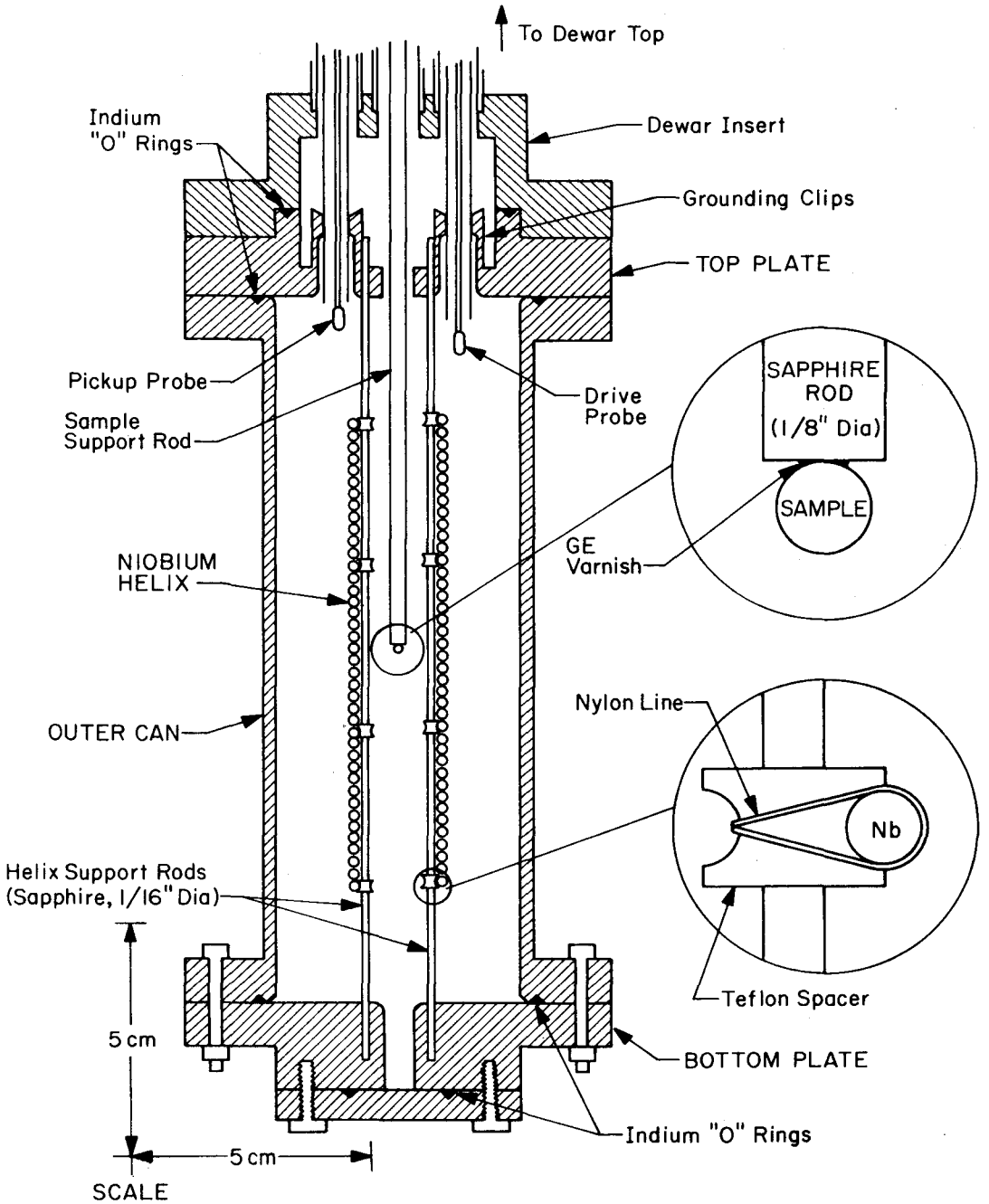

Fig. 4.4 General construction of the helical resonator is shown. The resonator consists of the niobium helix, outer can and two end plates. The outer can (copper) and the two end plates (brass) were electroplated with lead. The schemes of supporting the sample and the helix are shown in the expanded views.

(2) There were multiple modes in the resonator so that the measurement could be made at different frequencies.

The resonator consisted of a helical wire supported by two sapphire rods, an outer can and two end plates. The helix was wound from a mechanically polished niobium wire of 2 mm diameter. It was then annealed in a quartz tube under pressure of less than 2×10^{-5} mm Hg for three hours at temperature 1200-1350°C by means of induction heating in order to remove the internal stress. After annealing treatment, the helix was chemically etched in a mixture of HF and HNO_3 acids to expose a fresh surface. Then the helix was secured to the sapphire rods (1/16-inch diameter) and Teflon spacers with a fine nylon line (fishing line) as shown in the expanded view within the figure. The outer can and two end plates were made of copper and brass, respectively, and all the inside surfaces were electroplated with lead (Sec. 3.1.2). The current carrying vacuum seals were made with indium "O" rings at the top and bottom of the can as described previously (Sec. 3.1.3).

For the low temperature measurement the spherical sample was attached to one end of the sapphire support rod (1/8-inch diameter) with a small amount of varnish (see expanded view in the figure). This was done by spreading a thin layer of GE varnish (No. 7031) on the end face of the sapphire rod and then placing the spherical sample on it. The sample rod was then attached to a long stainless steel rod leading up to the top of the dewar system so that the sample could be moved into and out of the resonator at will.

Exactly the same rf instrumentation and cryogenic apparatus were used as in Secs. 3.1.3 through 3.1.5. However, a new calibration scheme was devised in order to determine the rf magnetic field at the site of the sample. This was necessary since the exact calculation of the field distribution in such a helical resonator* would be extremely difficult if not impossible.

Calibration

Presently we are interested in the determination of the rf magnetic field level at the site of the spherical sample placed within the resonator. This can be related to the measurable quantities of the resonator and sample as follows.

When a metallic sphere (in the normal state) is placed in an rf magnetic field, the field is shielded from the interior of the sphere by the skin effect. The current and magnetic field distribution on the surface of the sphere can be calculated with the assumption that the sphere is diamagnetic as far as the rf field is concerned. This gives the surface field as

$$H_{surface} = \frac{3}{2} H_s \sin\theta \sin(\omega t) \qquad (4.2)$$

where H_s is the applied magnetic field at the site of the sample, and θ

---

*For a calculation of field distributions in a helical resonator based on a simplified model, see, for example, S9.

**This is exactly the same problem as a superconducting sphere in a static magnetic field, except the rf skin depth is replaced by the superconducting penetration depth (see, for example, L5, p.34).

is the polar angle (the polar axis being along the direction of the applied field). Then the time-average power dissipation over the entire sample, P_s, can be evaluated as

$$P_s = 3\pi\, r^2 R_n H_s^2 \tag{4.3}$$

where r is the radius of the spherical sample and R_n is its normal state surface resistance. In the above derivation it is assumed that the rf skin depth is much smaller than the radius of the sphere*.

Recalling the definition of the quality factor of the resonator (Eq. (3.9))

$$Q_o^{-1} = \frac{P_{diss}}{\omega_o W} \tag{4.4}$$

where P_{diss} is the power dissipated in the resonator itself, W is its energy content and ω_o is the resonant frequency. Generalizing it for a loaded resonator (in this case with the spherical sample) we have

$$\begin{aligned} Q_L^{-1} &= \frac{P_{total}}{\omega W} \\ &= \frac{P_{diss} + P_s}{\omega W} \\ &= Q_o^{-1} + \frac{P_s}{\omega W} \end{aligned} \tag{4.5}$$

where Q_L is the quality factor of the loaded resonator, ω is its resonant frequency**, and P_s is the power dissipated due to the spherical

---

*The rf skin depth for the present samples was less than 14μ, whereas the radius of the samples was 0.5-1.0 mm.

**The shift in resonant frequency, $\Delta\omega = \omega - \omega_o$, due to loading by the sample is assumed to be small. In the experiment $\Delta\omega$ was $\sim$0.3 MHz at 90 MHz, most of which was due to the sample support rod.

sample.

Combining Eq. (4.3) and Eq. (4.5) we have

$$\frac{H_s^2}{W} = \frac{1}{3\pi r^2 R_n}\left(\frac{\omega}{Q_L} - \frac{\omega}{Q_o}\right) \equiv g \tag{4.6}$$

where g is defined in an exact analogy with Eq. (3.2).

All the quantities in g can be determined experimentally: Q_L and Q_o from the measurement of the cavity decay time ($Q = \omega\tau$) and R_n from the dc resistivity, ρ , of the same alloy samples by using the expression for the classical surface resistance, Eq. (2.4)*

$$R_n = (\pi f \mu_o \rho)^{1/2} \tag{4.7}$$

According to Eq. (4.6), the measurement of the resonator Q when a spherical sample is placed anywhere in the resonator gives the local magnetic field at the site of the sample. Then, by moving the sample along the axis of the helix, the axial magnetic field profile can be determined. The magnetic field distribution thus obtained is shown in Fig. 4.5 where the field can be seen to be sufficiently uniform over the dimension of the sample diameter (also shown) for the two modes (first and fourth modes) used in the measurement. Also the measured field distribution enabled us to identify the positions of the peaks in magnetic field where the g-factor in Eq. (4.6) was to be determined.

---

*For the majority of the alloy samples used, the rf skin depth, δ , was much larger than the mean free path of electrons, ℓ , (typically $100 \leq \delta/\ell \leq 1{,}100$). Therefore the use of the classical expression was well justified.

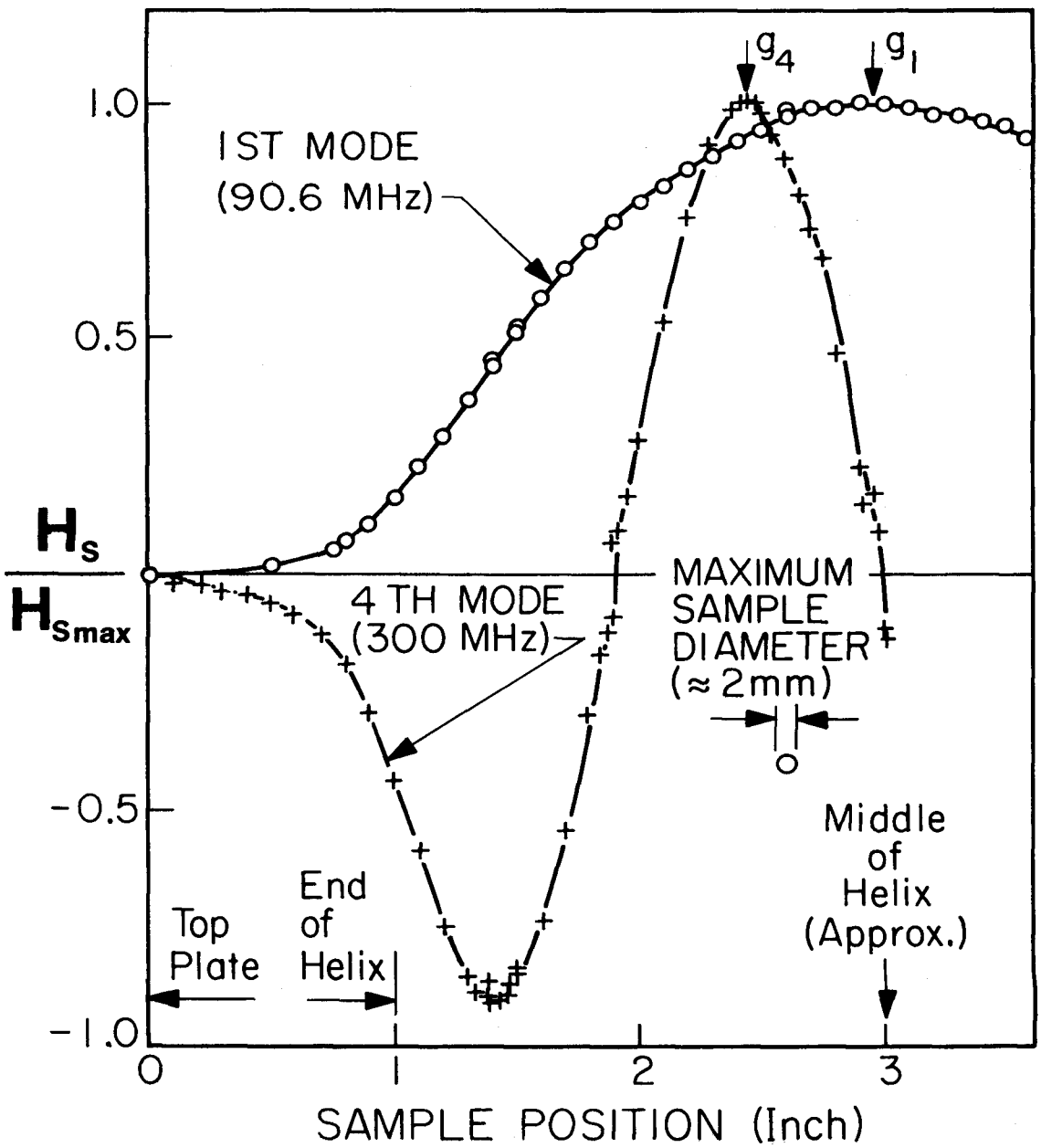

Fig. 4.5 The magnetic field distribution along the axis of the helix was determined by moving the spherical sample along the axis and measuring the resonator Q at each position. The magnetic field along the axis is normalized by the maximum field at which the g-values were determined (shown by arrows). Here the first and fourth modes which were used in the rf critical field measurements are shown.

Combining Eqs. (4.6) and (4.7), g is expressed as

$$g = \frac{1}{3\pi^{3/2}\mu_o^{1/2}\, r^2 (f\rho)^{1/2}} \left(\frac{1}{\tau_L} - \frac{1}{\tau_o}\right) \tag{4.8}$$

where τ_L and τ_o are respectively the loaded and intrinsic decay times of the resonator. The measurement of τ_L when the sample was located at the peak of the magnetic field distribution determined g values for the different modes. For the first mode (90.6 MHz), g-values were determined for 20 alloy samples, all of which agreed within $\pm$ 6%. Thus their average was used throughout the measurement as g_1

$$g_1 = 0.140 \pm .008 \quad (10^8 \text{gauss}^2/\text{joule})$$

Similarly, for the fourth mode (300 MHz) with four samples we obtained

$$g_4 = 0.090 \pm .005 \quad (10^8 \text{gauss}^2/\text{joule})$$

Once g-factors are determined as above (noting that Eq. (4.6) is equivalent to Eq. (3.2) for the half wave resonator) the rest of the measurement proceeds in exactly the same manner as in Sec. 3.2.4. Then the magnetic field at the site of the sample, H_s, is related to the measured power at the pickup probe, P_{pu}, as

$$H_s = (\alpha g\, P_{pu})^{1/2} \tag{4.9}$$

where the coupling constant α is determined in the same way as before.

The resulting errors, Δ , in the determination of the magnetic field at the sample site were estimated to be

$$\Delta H_s/H_s \leq 10\%$$

for the absolute error in H_s at a given frequency, and

$$\Delta H_s/H_s \leq 6\%$$

for the relative error between different samples at the same frequency. Also the relative error in the determination of magnetic fields at two different frequencies for a single sample was estimated to be

$$H_s/H_2 \leq 12\%$$

Sources of error are the same as those discussed in Sec. 3.2.6.

RF Critical Field Measurement

The determination of the rf critical field was carried out in the same manner as in Sec. 3.3.3. The quality factor of the resonator-sample system when the sample was normal was dominated by the dissipation due to the sample, whereas below T_c it was determined by the intrinsic dissipation inside the resonator itself* (the intrinsic Q of the resonator was typically 2-4 x 10^7). For the measurement of the rf critical field, the incident power was pulsed as before in order to avoid excessive heating of the sample. Upon reaching the critical field of the sample, the resonator Q was reduced by an amount proportional to the dissipation due to the normal sample. This change in Q at the transition depended on the sample and varied between a factor of about 10

*The loss due to the sample essentially vanished within a narrow temperature range below T_c, reaching less than a few percent of the normal state value at 0.99 T_c.

and 100 (the alloy samples being more dissipative than pure samples of the same size).

The observed pulse shapes are shown in Fig. 4.6 where the envelopes of the rf voltage at the pickup probe (proportional to the field level within the resonator) are shown. When the rf magnetic field at the site of the sample is small, the sample stays in superconducting state throughout the pulse duration. In this case the resonator is driven by the incident power, while the incident power is on, and after the power is off it dissipates the stored energy with the intrinsic characteristic time of the resonator itself as shown in the upper trace of Fig. 4.6a. As the incident power is increased, eventually a point is reached where the rf critical field is reached at the equator of the sample and the entire sample is driven normal by thermal propagation as can be seen in the lower trace of Fig. 4.6a.

Further increase in the incident power results in a shorter driving time to reach the critical field as shown in Fig. 4.6b. Looking at the breakdown field on a much finer time scale (Fig. 4.7a and b) the entire process of the "magnetic-thermal" breakdown can be seen to take place on a time scale much shorter than the characteristic decay time of the resonator. Thus this field at which there was a break in the slope of the energy content of the resonator was operationally defined as the rf critical field H_c^{rf}.

As mentioned previously, H_c^{rf} was defined as the magnitude of the rf critical magnetic field at the site of the sample (i.e., the demagnetization factor was not included so that the actual magnetic field at

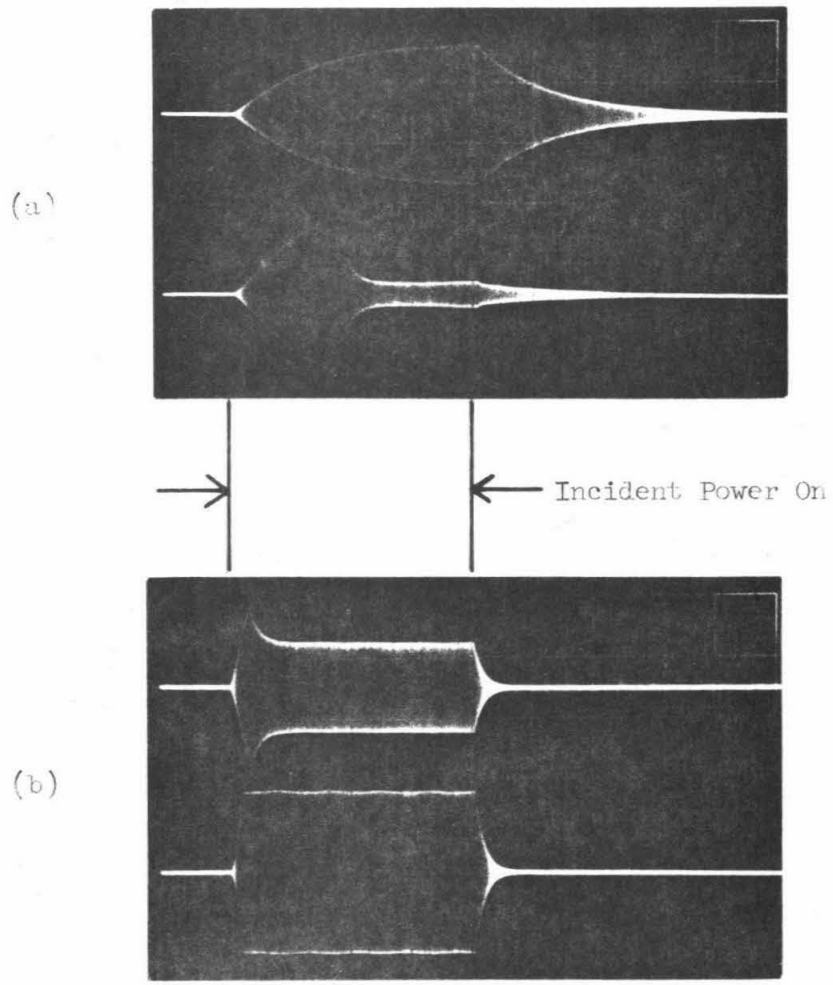

Fig. 4.6 The envelopes of the rf voltage proportional to the field level within the resonator are shown. (a) The upper trace shows no breakdown. As the incident power is increased, the rf critical field is reached where the sample becomes normal as shown in the lower trace. (b) Further increase in the incident power results in a shorter driving time to reach the rf critical field.

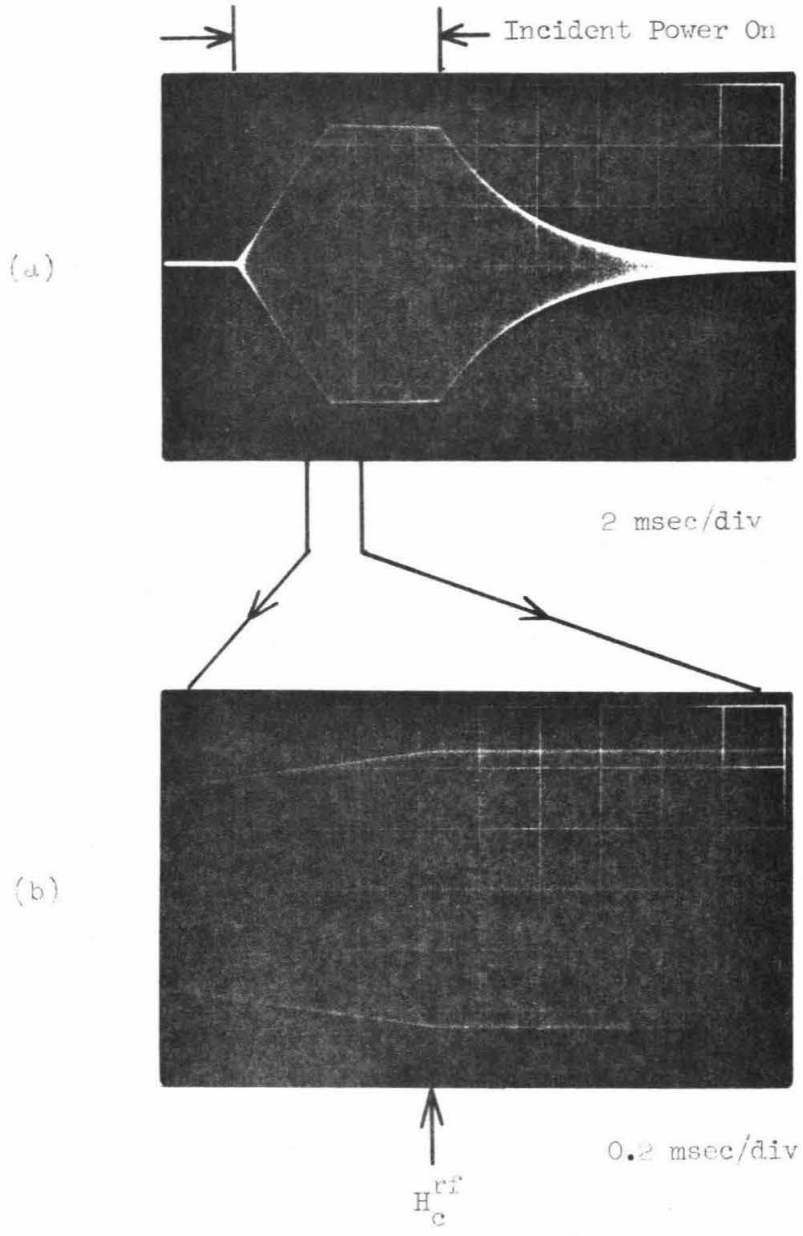

Fig. 4.7 The envelope of the rf field level contained in the resonator is shown. (a) The break in the initial slope of the resonator field level determines the rf critical field at which the sample is driven normal. (b) The entire process of breakdown can be seen to take place on a time scale much shorter than the decay time of the resonator with the sample in the normal state (the trailing edge in (a)).

the equator of the sample at the time of breakdown would be 1.5 H_c^{rf} if the sample were a perfect sphere). Since H_c^{rf} was normalized by H_c^{dc}, which was similarly defined, there was no need to determine the demagnetization factor of each sample,* thus enabling the direct comparison between H_c^{rf} and H_c^{dc} to be made.

*The orientations of samples were kept the same in both measurements.

4.3 Experimental Results and Discussion

For every sample of tin, indium and their alloys the rf critical fields were typically measured in the reduced temperature range $0.8 \leq t \leq 1.0$. It was found that the following form for the reduced rf critical field displayed the temperature dependence very clearly:

$$h_c^{rf}(t) = H_c^{rf}(T)/H_c^{dc}(T)$$

$$= \frac{H_c^{rf}(T)}{H_o^{dc}(1 - (T/T_c)^2)} \qquad (4.10)$$

H_o^{dc} and T_c values were determined for each sample* in the preceding sections.

4.3.1 RF Critical Field of Pure Tin and Indium

Before proceeding to the details of experimental results, a simple extension of the boundary energy argument (Sec. 2.2.2) is proposed for different "dimensions" of nucleation of the normal phase.

In the one-dimensional formulation of the GL theory, the superheating field defines the field at which the order parameter (the density of superconducting electrons) is driven to zero at the surface of a superconductor filling a half-space. This can be pictured as a nucleation of the normal phase in the form of a plane at the surface. In this

*For the spherical samples of pure indium, because of the difficulty of handling to be described in Sec. 4.3.1, H_o^{dc} was determined for two out of four samples used in the experiment. They agreed within 2% and their typical value was used for all four samples of indium.

case we previously obtained (in Sec. 2.2.2) the superheating field for type I superconductors by balancing the two contributions to the free energy, i.e., the diamagnetic energy, $\lambda(\frac{1}{2}\mu_o H^2)$, and the loss in condensation energy, $\xi(\frac{1}{2}\mu_o H_c^2)$, so that the boundary energy vanished at H ($\equiv H_{sh}$) such that

$$\lambda H^2 = \xi H_c^2$$

or,

$$\left.\frac{H_{sh}}{H_c}\right|_{plane} = \frac{\xi}{\lambda} = \frac{1}{\sqrt{\kappa}} \qquad (4.11)$$

This energy balance can be extended to other dimensional forms of nucleation such as a line and a point. The line nucleation can be pictured as a vortex-like nucleation where the normal phase is created in the form of a line lying at the surface. In this case the magnetic field distribution and the order parameter variation are centered about the nucleus and are semi-cylindrical with their characteristic lengths. Then the diamagnetic energy is proportional to

$$\int_0^\infty [H(r)]^2\, 2\pi\rho\, d\rho$$

$$= \int_0^\infty H^2\, e^{-2\rho/\lambda}\, 2\pi\rho\, d\rho$$

$$\propto \lambda^2 H^2$$

where the field distribution was assumed to be exponential in the

radial coordinate ρ . Similarly, the loss in condensation energy is proportional to

$$\propto \xi^2 H_c^2$$

Then balancing the above two contributions we obtain

$$\left.\frac{H_{sh}}{H_c}\right|_{line} \propto \frac{\xi}{\lambda} = \frac{1}{\kappa} \tag{4.12}$$

A similar argument applies to the case of the nucleation at a point where the magnetic field and the order parameter distributions are semi-spherical and centered about the point of nucleation so that

$$\left.\frac{H_{sh}}{H_c}\right|_{point} \propto 1/\kappa^{3/2} \tag{4.13}$$

It will be argued later that the proportionality constants in the above equations may be determined near T_c, where the effect of localized nucleation becomes weak due to the divergence of the order parameter near T_c.

In the limit of low κ (extreme type I) the result of the one-dimensional GL theory (01) for the superheating field (the plane nucleation field in the present scheme) is (Eq. (2.30))

$$\frac{H_{sh}}{H_c} = \frac{0.841}{\sqrt{\kappa}} \tag{4.14}$$

This derivation depended on the assumption of the local relation between

the current and the vector potential (Eq. (2.21)) so that it is valid only near T_c where the penetration depth, $\lambda_L(T)$, is much larger than the electrodynamic coherence length, ξ_o.* For tin and indium, empirical values of ξ_o are 2300Å and 4400Å, whereas the penetration depth at 0°K, $\lambda_L(0)$ are 510Å and 640Å, respectively (L3, p.73). Thus in most of the range of the present experiment ($0.8 \lesssim t \lesssim 1.0$) both metals are in the anomalous limit, i.e., $\xi_o >> \lambda_L(t) = \lambda_L(0)/(2(1-t))^{1/2}$ except very near T_c ($\xi_o \simeq \lambda_L(t)$ at $t \simeq 0.97$-0.99). In this situation where the non-local electrodynamics is important, the range of validity of Eq. (4.14) may be extended phenomenologically by using the penetration depth derived microscopically in the extreme anomalous limit as obtained by BCS (B1) for diffuse scattering at the surface

$$\lambda_\infty(T) = \frac{3^{1/6}}{(2\pi)^{1/3}} \left(\frac{\xi_o \lambda_L^2(T)}{J(0,T)}\right)^{1/3} \tag{4.15}$$

where $\lambda_L(T)$ is the London penetration depth and $J(0,T)$ is the function introduced by BCS varying smoothly from 1.0 at 0°K to 1.33 at T_c.

For the present temperature range $\lambda_L(T)$ can be approximated by (T4, p.113)

$$\lambda_L(T) = \lambda_L(0)/(2(1-t))^{1/2} \tag{4.16}$$

so that

---

*This condition (S10, p.27) restricts the applicability of Eq. (4.14) for tin and indium in the reduced temperature range of $(1 - t) <<$ .01-.03.

$$\lambda_\infty(T) = \frac{3^{1/6}}{(4\pi\, J(0,T))^{1/3}} \left(\frac{\xi_0\, \lambda_L^2(0)}{(1-t)}\right)^{1/3} \tag{4.17}$$

We also have the expression for the GL coherence length for a pure metal as

$$\xi(T) = 0.74\, \xi_0/(1-t)^{1/2} \tag{4.18}$$

Then using the above two equations in the definition of κ, we obtain

$$\kappa_\infty \equiv \frac{\lambda_\infty(T)}{\xi(T)} = 0.635(\lambda_L(0)/\xi_0)^{2/3}\, (1-t)^{1/6} \tag{4.19}$$

so that the superheating field in Eq. (4.14) is now given by

$$\left.\frac{H_{sh}}{H_c}\right|_{plane} \simeq 1.04\, \kappa_p^{-1/3}(1-t)^{-1/12} \tag{4.20}$$

where the expression for κ in a pure metal at T_c (G2), $\kappa_p = 0.96\lambda_L(0)/\xi_0$, was used. The same expression was obtained previously (S7) in the framework of the one-dimensional GL theory, where the numerical constant turned out to be 1.36 instead of 1.04. The above temperature dependence of the superheating field was previously observed experimentally (S7) for a collection of small spheres (1-10 microns in diameter) of tin and indium. In the same experiment the value of the numerical constant in Eq. (4.20) was found to be ~ 0.9.

For the case of line nucleation, using the expression for κ_∞ in Eq. (4.19), we obtain the temperature dependence of the superheating

field as

$$\left.\frac{H_{sh}}{H_c}\right|_{line} \propto \frac{1}{\kappa_\infty} \propto (1 - t)^{-1/6} \tag{4.21}$$

and similarly for the point nucleation

$$\left.\frac{H_{sh}}{H_c}\right|_{point} \propto \frac{1}{\kappa_\infty^{3/2}} \propto (1 - t)^{-1/4} \tag{4.22}$$

The rf critical fields were measured for several samples of pure tin and indium spheres 1.5-2 mm in diameter. It was found that their rf critical fields were much higher than their bulk critical fields by a factor of 2-3.5, depending on the temperature, and increasing toward the transition temperature. In the vicinity of T_c the observed critical fields were very close to the superheating fields predicted by the one-dimensional Ginzburg-Landau theory. From the observed temperature dependence of the rf critical field, a line nucleation is inferred for both tin and indium.

Tin

The rf critical fields were measured at 90 MHz for two spherical samples of tin. The reduced rf critical field, $h_c^{rf} = H_c^{rf}(T)/H_c^{dc}(T)$, is shown as a function of the reduced temperature, T/T_c, in Fig. 4.9. The temperature dependence of h_c^{rf} was found to be described very closely by that of the superheating field for the line nucleation (Eq. (4.21)). Thus it was inferred that the nucleation of the normal phase in the form of a line was responsible for the transition in the rf field. This type of nucleation may well be caused by inhomogeneities at the surface, such

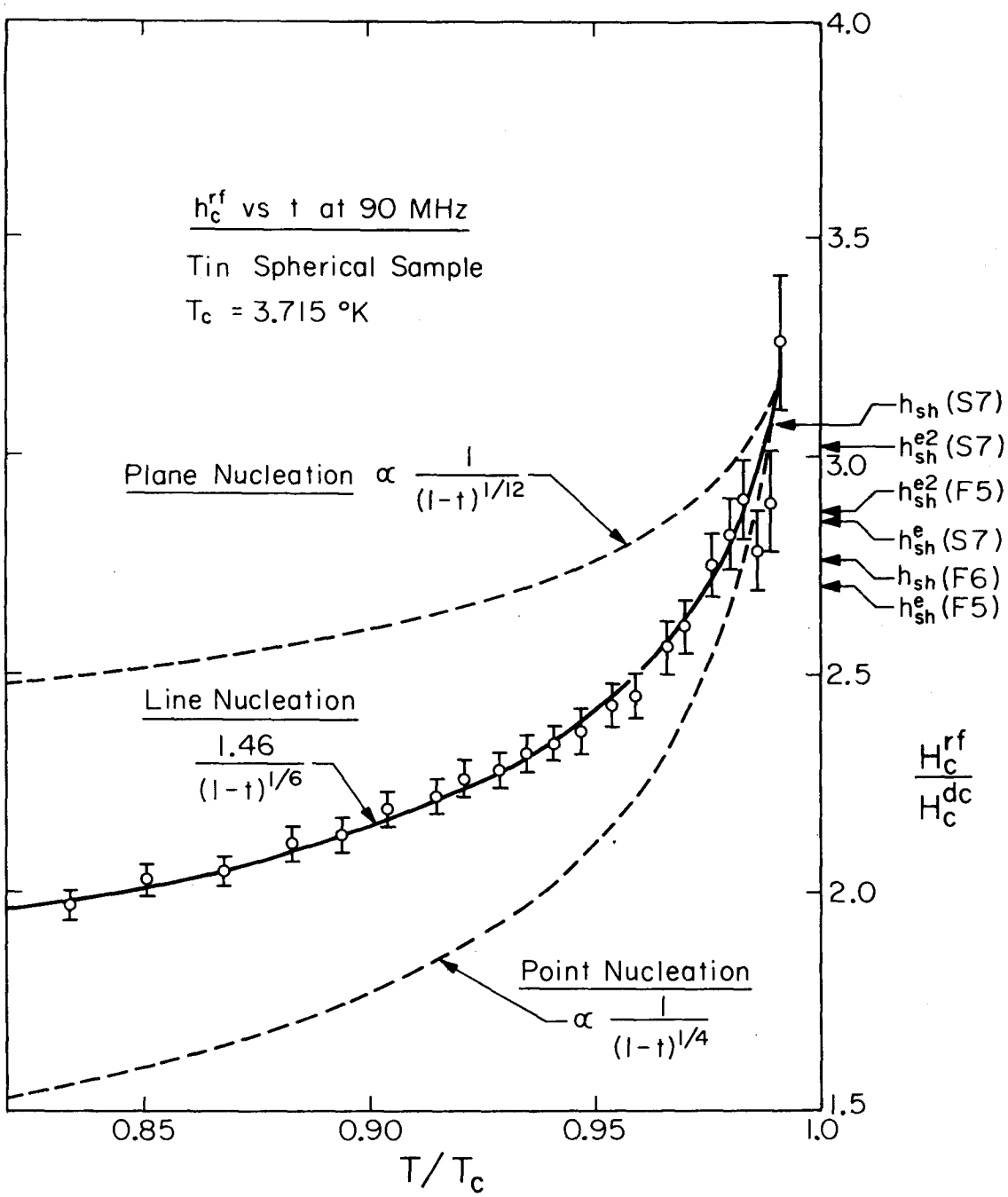

Fig. 4.9 The reduced rf critical field of tin is shown as a function of the reduced temperature. The solid line is a least-squares fit for the line nucleation model. The upper curve represents the dc superheating field (plane nucleation field) observed by Smith et al. Previously observed dc superheating fields and the expected superheating fields (see text) are shown by arrows on the right hand side.

as grain boundaries which would ease the nucleation of the normal phase.* For the present spherical samples only moderate amounts of superheating in dc field were observed (up to 1.2 H_c for tin and up to 1.6 H_c for the best indium sample), which suggested that nucleation centers were actually present in some form in these samples.

The data of h_c^{rf} as a function of the reduced temperature were fitted to the following expression for the line nucleation

$$h_c^{rf} = C/(1 - t)^{1/6} \tag{4.23}$$

with one adjustable parameter C. The result shows a good fit as can be seen in Fig. 4.9. The upper curve in the same figure represents the dc superheating field (plane nucleation field $\propto (1-t)^{-1/12}$) observed by Smith et al. (S7)** for a collection of tin spheres. The lower curve shows the temperature dependence for a point nucleation, $(1-t)^{-1/4}$, where its coefficient is adjusted, for the purpose of illustration, so that it agrees with the other two experimental curves at $t = 0.99$.

The present rf results, h_c^{rf}, can be directly compared with the previous experimental values of dc superheating fields, h_{sh} ($\equiv H_{sh}/H_c$), that have been observed. By doing so, it should be possible to determine, at least empirically, if the plane nucleation limit is reached near T_c in the present rf experiment. For a collection of tin spheres

*In fact, previous observations suggest that the ideal (the plane nucleation) superheating could be observed only for single crystal samples (G5,F5) and for spherical samples of small diameter where surface flaws are avoided (S7,F6).

**This line is the same as the fit to their data within a few percent.

of 1-10 microns in diameter, Smith et al. (S7) observed a superheating up to

$$h_{sh}(S7) = 3.07 \qquad \text{at} \qquad t \simeq 0.99$$

The temperature dependence they observed was that due to the plane nucleation. Feder and McLachlan (F6) also measured the superheating in single spheres, typically 10 microns in diameter, and found

$$h_{sh}(F6) = 2.76 \qquad \text{at} \qquad t = 1 \quad \text{by extrapolation}$$

For the purpose of comparison, the expected superheating field (for plane nucleation) may be deduced from Eq. (4.14)*

$$\frac{H_{sh}}{H_c} = 2^{-1/4}\, \kappa^{-1/2}$$

by using the GL parameter, κ_{sc}, obtained by supercooling observations. Previous supercooling observations give $\kappa_{sc} = 0.087$ (S7) for a collection of small spheres and $\kappa_{sc} = 0.097$ (F5) for cylindrical samples of single crystal so that the expected superheating fields are

$$h^e_{sh}(S7) = 2.85$$

and

$$h^e_{sh}(F5) = 2.70$$

---

*At the time of writing a preprint was made available (P13) in which an analytical expression for the superheating field correct to second order in κ was evaluated as

$$H_{sh}/H_c = 2^{-1/4}\, \kappa^{-1/2}(1 + 15\sqrt{2}\,\kappa/32) \qquad (4.26)$$

The expected superheating fields using κ_{sc} in this equation are shown as h^{e2}_{sh}(Ref.) in the figure.

All the above values are shown by arrows in Fig. 4.9 where the rf critical fields near t = 0.98-0.99 agree very closely with the previously observed superheating fields and the expected superheating fields deduced from κ_{sc}. Therefore it may be concluded that the present rf critical field reaches the plane nucleation limit at t = 0.98-0.99.* A possible explanation for this behavior (h_c^{rf} approaching the ideal h_{sh}) is that the line nucleation is made ineffective as the GL coherence length, $\xi(t)$, becomes larger than a typical size of nucleation centers ($\xi(t) \simeq 2$ microns at t = 0.99 for tin).

Under the above circumstance, we may impose a condition that the line nucleation field approaches the plane nucleation field so that equating Eqs.(4.23) and (4.20) we obtain

$$C = 1.04\ \kappa_p^{-1/3}(1 - t_i)^{1/12} \tag{4.24}$$

where t_i is the temperature at which the line nucleation becomes ineffective and is estimated to be 0.98-0.99 for the present case. Then using the value of κ_p obtained by a previous supercooling observation ($\kappa_p = 0.0926$, F6), we can evaluate C as

$$C = 1.57 - 1.66$$

which compares favorably with the value of C = 1.46 determined from the fit to the present experimental data.

---

*Above the temperature of 0.99 T_c, because of the normalization by $H_c^{dc}(T) = H_o^{dc}(1-(T/T_c)^2)$ used in obtaining h_c^{rf}, the error in h_c^{rf} rapidly increases due to the uncertainty in temperature measurement ($\sim$1 m°K) and the uncertainty in the absolute T_c determination between different low temperature experiments ($\Delta T_c \lesssim 4$ m°K due to the hydrostatic temperature variations).

Indium

Four spherical samples of indium, typically 2 mm in diameter, were used in the rf critical field measurements. The results showed essentially the same temperature dependence as for tin so that it was inferred again that the line nucleation was responsible for the phase transition in the rf field. Since indium is very similar to tin in terms of superconducting parameters such as the electrodynamic coherence length and the penetration depth, all the preceding arguments used for tin apply to indium with no significant modifications.

The results on all four samples are shown in Fig. 4.10. The temperature dependence was found to be the same for all samples. However, the absolute magnitude was somewhat dependent on the exact condition of the surface of the sample, which was not unreasonable since the normal phase would be nucleated at the "weakest" spot on the surface. Initially it was found that the surface of indium samples could be easily scratched in the process of preparation for a low temperature experiment, even though a soft camel-hair (or nylon) brush was used in their handling. For such a sample with obvious scratches on the surface, the rf critical field (the lowest line in the figure) was found to be slightly lower than that of a sample which was handled as little as possible before the low temperature experiment (the second line from the bottom).

Eventually a chemical etching solution for indium* was found to remove the scratches on the surface, leaving a shiny, very smooth surface. This process improved the critical field by about 15% on the

*A mixture of one part of H_2O_2(30%), one part of HCl and three parts of H_2O by volume.

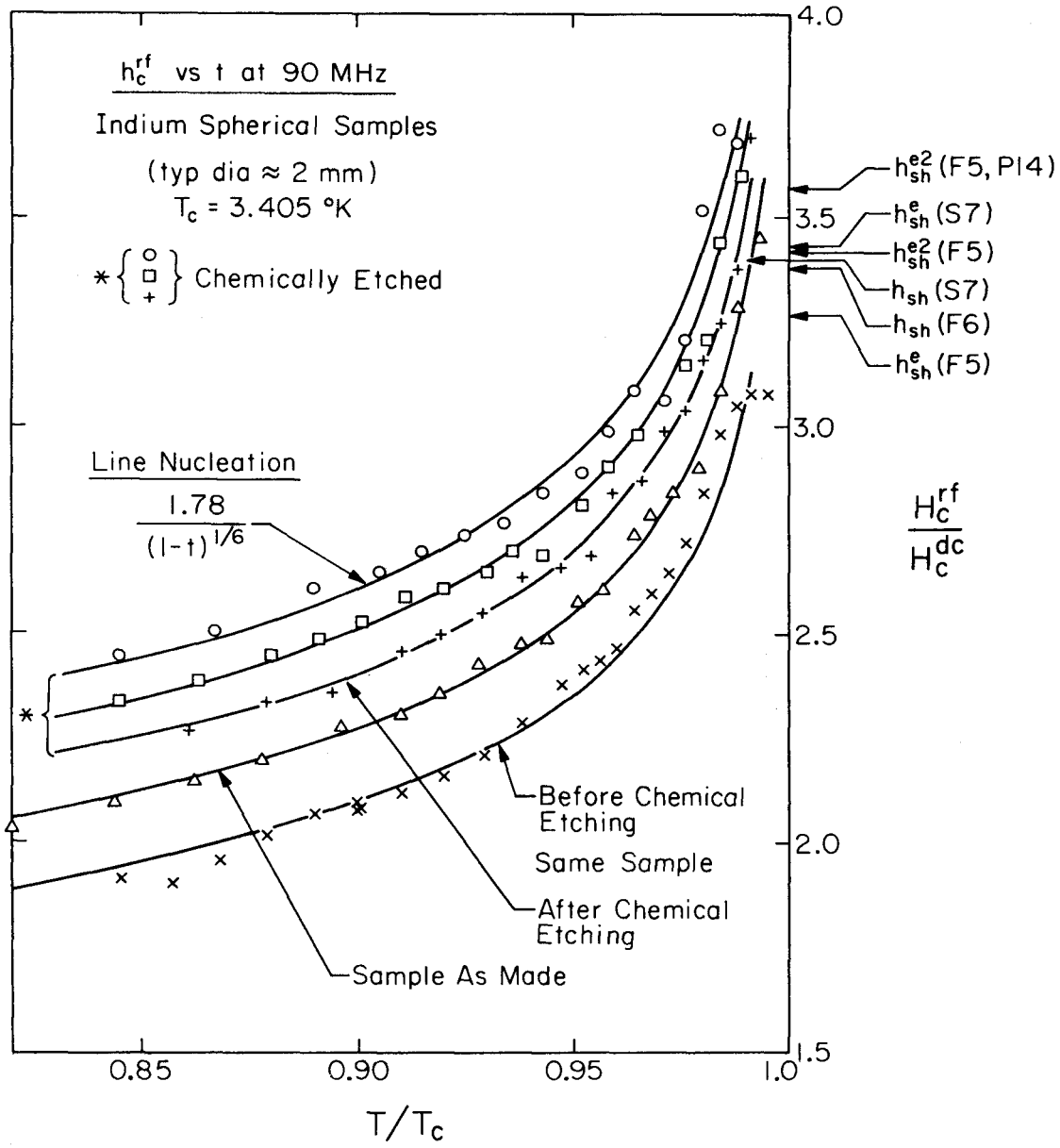

Fig. 4.10 The rf critical fields of four spherical samples of indium at 90 MHz. Upper three curves are for chemically etched samples. The solid lines are the fit to the experimental data for the line nucleation model.

same sample as shown in the same figure. Once the indium samples were prepared in this manner, their results showed that the critical fields were within ±5% of each other, as can be seen for three chemically etched samples (upper three curves).

The present results are again compared with the past measurements in exactly the same manner as for tin. Previously observed superheating fields in static magnetic field are

$$h_{sh}(S7) = 3.4 \qquad \text{at} \qquad t = 0.99$$

for a collection of small spherical samples of 1-10 microns in diameter and

$$h_{sh}(F6) = 3.38 \qquad \text{at} \qquad t = 1.0 \quad \text{by extrapolation}$$

for single spheres of typically 10 microns in diameter. Also, the expected superheating fields deduced from the supercooling data are

$$h^{e}_{sh}(S7) = 3.43$$

for a collection of small spheres ($\kappa_{sc} = 0.060$) and

$$h^{e}_{sh}(F5) = 3.27$$

for a cylindrical sample of single crystal ($\kappa_{sc} = 0.062$).

All of the above values are shown by arrows in the figure, which leads to the same conclusion as for tin, i.e., the line nucleation model explains the observed temperature dependence up to t = 0.98-0.99 where the ideal (plane) nucleation field is reached.

4.3.2 RF Critical Fields of SnIn and InBi Alloys at 90 MHz

The rf critical fields were measured at 90 MHz for 10 SnIn and 10 InBi alloys. These alloys covered both the type I and type II regimes and their GL parameter was as high as 1.75, which was well into the type II region. The results are shown* for SnIn alloys in Fig. 4.11 and for InBi alloys in Fig. 4.12, where the reduced critical fields h_c^{rf} (= H_c^{rf}/H_c^{dc}), are shown as a function of the reduced temperature, $t(= T/T_c)$, as before. As can be seen in the figures, varying amounts of superheating were observed for both types, i.e., H_c^{rf} higher than H_c for the type I and higher than H_{c1} for the type II superconductors. At a given temperature, the amount of superheating consistently decreased as the GL parameter increased (or equivalently as the alloy concentration increased). Also, a systematic tendency of the h_c^{rf} to increase toward the transition temperature was noted. However, it was found that the exact manner of this temperature dependence was somewhat different between the samples of the two alloy systems for similar κ. In particular, SnIn samples were generally found to show less temperature dependence than InBi samples of a similar κ.

Before going further into the possible causes of the above behavior, the expected superheating field and its temperature dependence in the local limit is discussed. In the preceding section it was noted that, for pure tin and indium, the ordinary GL formulation (local electrodynamics) was valid only in the vicinity of T_c. The

*A few samples were omitted because they crowd the figure.

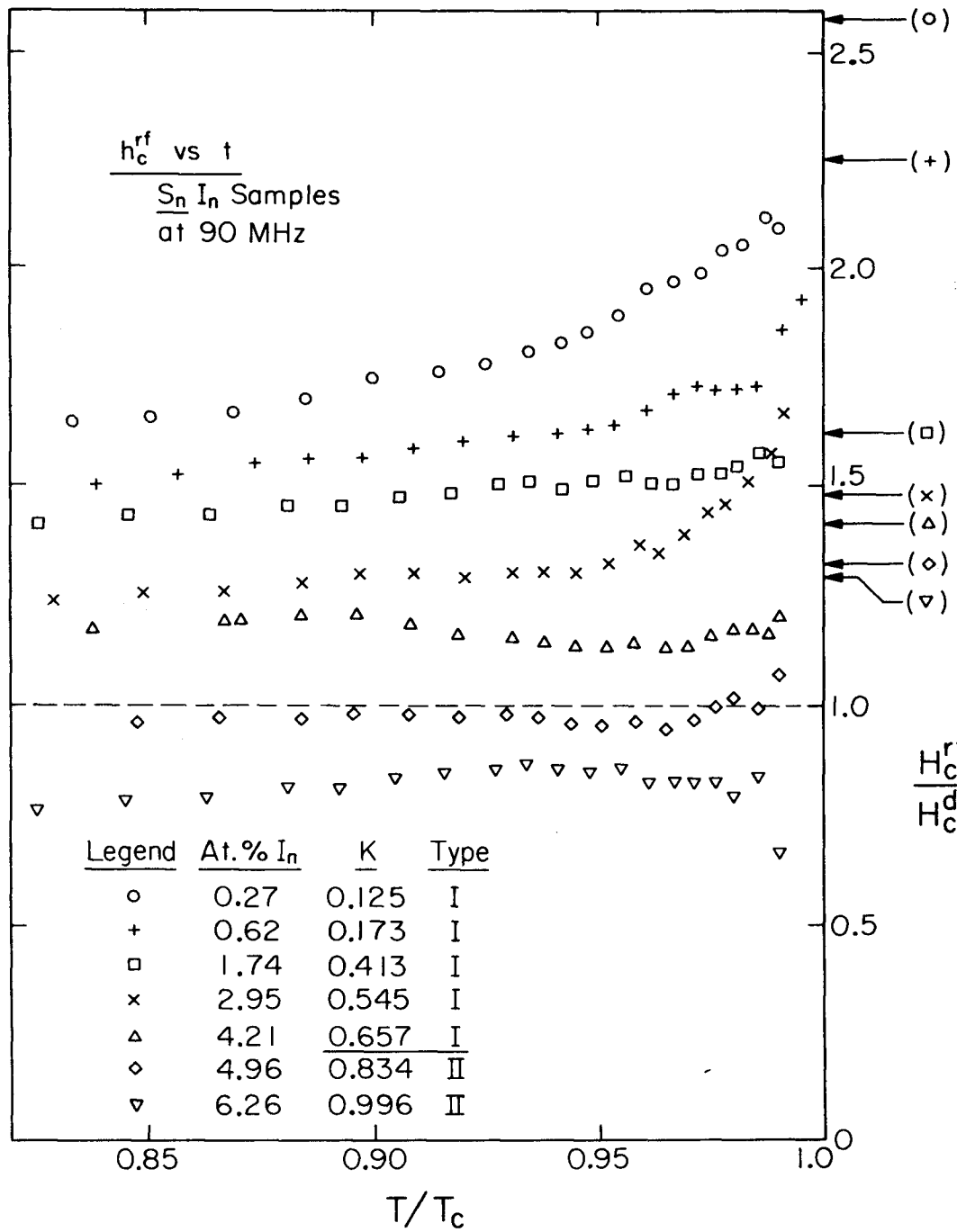

Fig. 4.11 The rf critical fields of SnIn alloys at 90 MHz are shown as a function of the reduced temperature. The superheating field of each sample expected from the one-dimensional GL theory is shown by an arrow on the right-hand side.

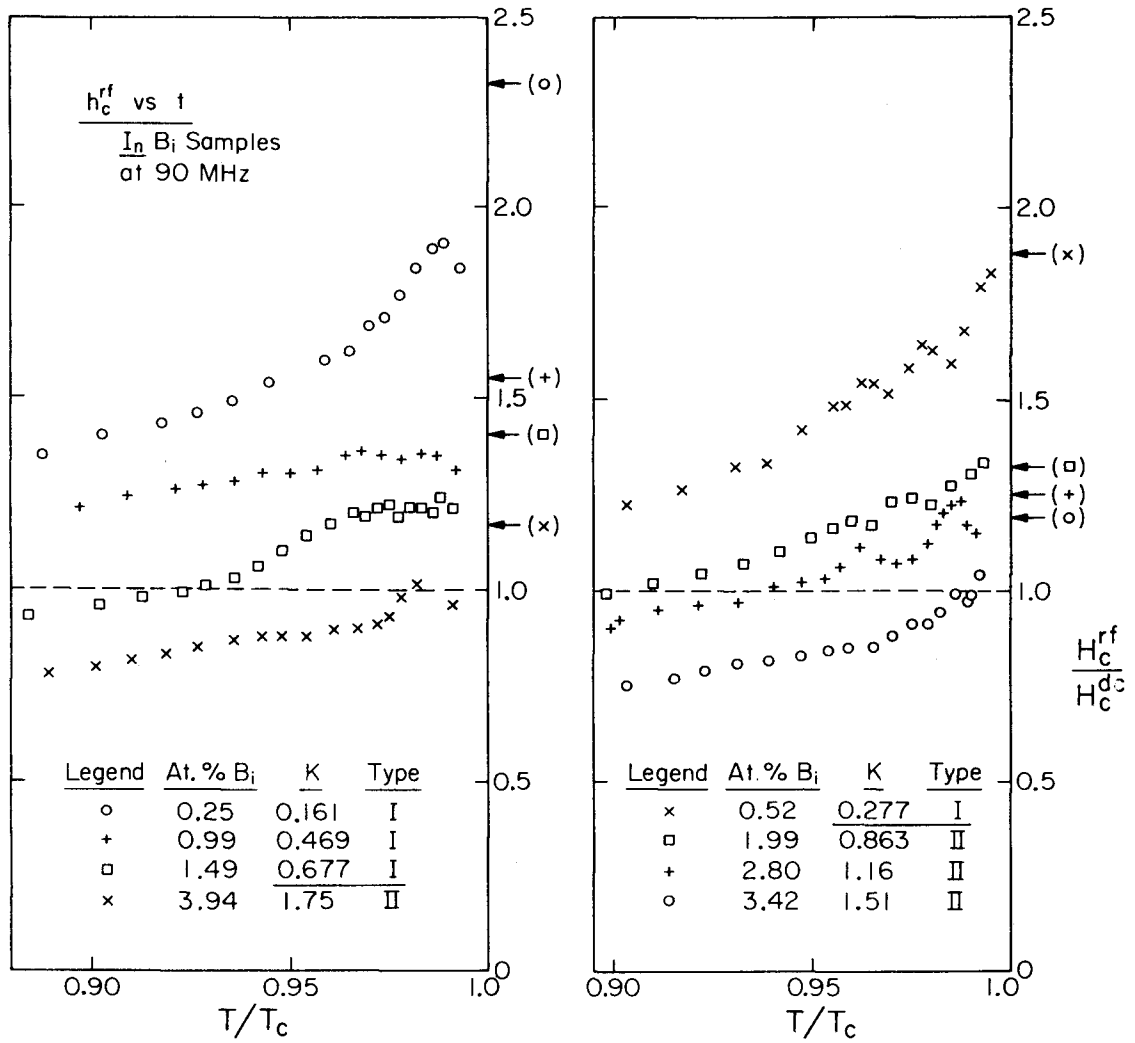

Fig. 4.12 The rf critical fields of InBi alloys at 90 MHz are shown as a function of the reduced temperature. The superheating field of each sample expected from the one-dimensional GL theory is shown by an arrow on the right-hand side.

reason for the restriction is that the local electrodynamics is valid only if the electrodynamic coherence length, ξ_0 , is much smaller than the penetration depth, $\lambda_L(t)$. However, as soon as the pure metals are alloyed, the mean free path of the electrons, ℓ , is reduced, which in turn reduces the effective electrodynamic coherence length, ξ_{eff}, and increases the effective penetration depth, λ_{eff}, at the same time.*

This means that the local electrodynamics becomes important where ℓ becomes comparable or less than the ξ_0 of pure metals, which happens with very little impurity concentration in the present case.** Then for most of the present alloy samples except the very dilute ones, the local GL equations are expected to be valid in the temperature range of the present measurement.

An approximate temperature dependence of the superheating field, H_{sh}, in the ordinary Ginzburg-Landau framework (local electrodynamics) can be obtained by expressing κ in terms of $H_c(T)$ and $\lambda_L(T)$ as (T4)

$$\kappa = 2\sqrt{2}\,\pi\, H_c(T)\, \lambda_L^2(T) / \phi_0 \qquad (4.27)$$

---

*Approximate forms of these two lengths are $\xi_{eff}^{-1} = \xi_0^{-1} + (a\ell)^{-1}$ where $a \simeq 0.8$ (P3) and $\lambda_{eff}(t) = \lambda_L(t)/\chi^{1/2}$ where χ is the function introduced by Gor'kov (G8) and can be approximated by $\chi = (1 + \xi_0/\ell)^{-1}$ (L3, p.48).

**For example, for SnIn alloys ℓ = 2,360A at 0.62 at.% In, whereas ξ_0(Sn) = 2,300A, and for InBi ℓ = 2,100A at 0.25 at.% Bi, whereas ξ_0(In) = 4,400A. ℓ is listed in Table 4.1 for the present samples.

where ϕ_0 is the flux quantum equal to hc/2e. With the empirical approximations $H_c \propto (1 - t^2)$ and $\lambda_L^2 \propto (1 - t^4)^{-1}$, we have

$$\kappa \propto 1/(1 + t^2) \tag{4.28}$$

Using the above κ in Eq. (4.14)*, the approximate temperature dependence of the superheating field for the plane nucleation is

$$\left.\frac{H_{sh}}{H_c}\right|_{plane} \propto (1 + t^2)^{1/2} \tag{4.29}$$

Similarly for the line and point nucleations we obtain, using Eq (4.12) and (4.13)

$$\left.\frac{H_{sh}}{H_c}\right|_{line} \propto (1 + t^2) \tag{4.30}$$

and

$$\left.\frac{H_{sh}}{H_c}\right|_{point} \propto (1 + t^2)^{3/2} \tag{4.31}$$

The above estimates give the variation in the superheating field between T_c and 0.9 T_c of 5%, 10% and 16% for the plane, the line, and the point nucleation, respectively. These variations are generally too small to account for the observed temperature dependence for most of the samples except for several SnIn samples (Sn + 0.62, 1.05, 1.74

---

*Since Eq. (4.14) is a limiting expression for small κ we are still restricted to type I superconductors. For higher κ the above expression will give an upper limit on the temperature variation of h_{sh} since the actual superheating field has a weaker dependence on κ than in Eq. (4.14).

and 4.96 at.% In).*

The experimental observation of superheating in a static magnetic field for alloys has been found in general to be difficult. However, very recently Parr (P14) has successfully observed the superheating field for a series of dilute InBi alloys (up to 0.6 at.% Bi) in the form of spheres typically 18 microns in diameter. According to his observation, the switch-over from the non-local type of temperature dependence ($h_{sh} \propto (1 - t)^{-1/12}$) to the local type ($h_{sh} \sim$ const. to first order in t) is complete before the concentration of Bi reaches 0.4 at.%. This means for the present InBi alloy samples (0.25-3.94 at.% Bi) that the superheating field is expected to have only a weak temperature dependence in the temperature range of the present measurements, whereas the rf critical fields for InBi samples change by as much as 50% between T_c and 0.9 T_c.

For the present alloy samples, considering the above observation as well as the discrepancy in the temperature dependence of h_c^{rf} between the two alloy systems of similar κ , it is quite probable that defective areas on the surface of the samples (or "weak" spots) are responsible for the nucleation which causes the large temperature dependence in the rf critical field. The visual observation of the samples under a microscope showed that a somewhat coarse surface involving dendritic structures tended to develop as the concentration of alloy was increased. This surface structure was particularly notable

---

*However, among them only one sample (Sn + 1.74 at.% In) shows the expected superheating field toward T_c (see Fig. 4.11).

on the hemisphere where the solidification took place last when the samples were made.

It was also noted when making the spherical samples, that the Sn-based spherical samples were much easier to make than the In-based samples in terms of their sphericity and the smoothness of the surface, probably due to the higher surface tension of tin in the molten state compared to indium. This resulted in better success rates for SnIn alloys than for InBi alloys, which might explain the smaller temperature dependence of h_c^{rf} for SnIn samples compared to InBi samples.

Also as noted in the previous sections on dc measurements, the original samples (as made) showed a broadened transition (0.1-0.2°K) indicating the presence of inhomogeneous solute concentration within the samples and possibly of different metallurgical phases. After the annealing treatment already described, the samples showed a reasonably narrow width in the transition temperature (see Table 4.2) as well as well-defined dc critical fields (entry field) in a static magnetic field, which indicated that the bulk of the samples was a homogeneous solid solution. However, there remained a possibility of localized inhomogeneities being present on the surface of the samples which would not have been detected by the susceptibility measurement, since it generally measured the average magnetic property of an entire spherical sample.

Another observation that is worthwhile noting at this point is that the surface resistance of the spherical samples in the normal state was consistent within ±6% with the classical surface resistance

deduced from the bulk resistivity of the cylindrical alloy samples (see calibration in Sec. 4.2.4). Since the skin depth in that measurement sampled a surface layer of typically between 0.5 and 15 microns, the agreement with the classical expression meant that the major portion of the surface layer within such depths was on the average of the same composition as the bulk of the sample. This again suggests that the defects, if present, are not global but localized on the surface.

Even with the presence of localized defects, it may be expected that their effects would tend to be diminished as the transition temperature is approached, since the GL coherence length diverges as $(1-t)^{-1/2}$ thus making the defects "invisible" to the superconducting electrons. Thus the following approach was used in presenting the summary result on alloys. Since the highest temperature where a reliable rf critical field measurement was made was about 0.99 T_c, the observed h_c^{rf} around 0.99 T_c would give a lower bound on the attainable field. Thus these points, h_c^{rf} $(t=0.99)$, are taken as the basic experimental points* and shown as a function of the GL parameter in Fig. 4.13. Furthermore, whenever there was a systematic trend in h_c^{rf} below $\sim$0.99 T_c it was extrapolated to T_c and shown at the tip of an arrow originating from the t = 0.99 experimental point.

---

*The absolute errors in h_c^{rf} (shown in the figure) were estimated to be less than 20% where the error in the absolute determination of H_c^{rf} (10%) and the estimated errors in H_o^{dc} and T_c were combined.

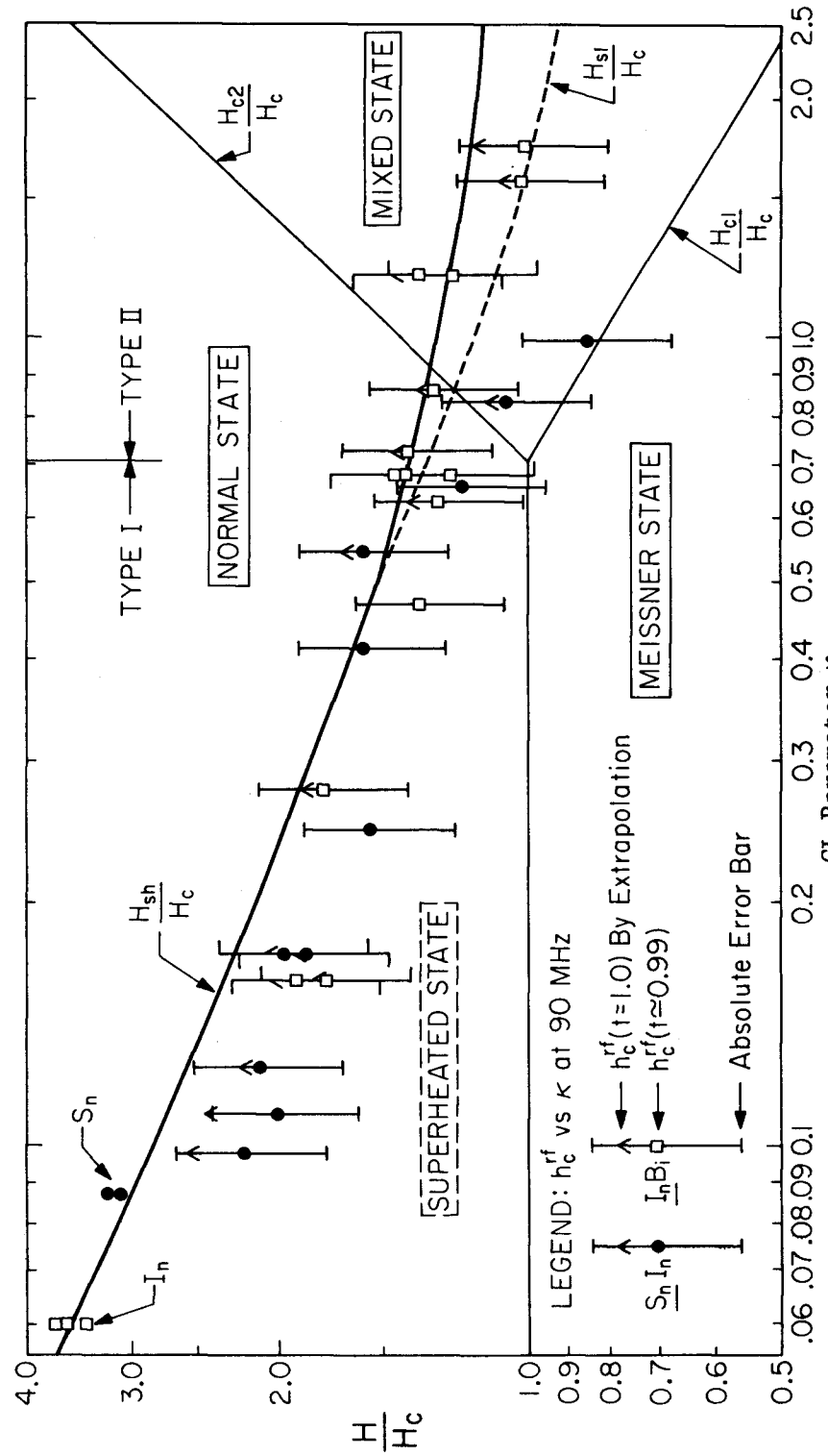

Fig. 4.13 The rf critical fields that were actually measured (near $t = 0.99$) for all SnIn and InBi alloy samples are shown as a function of the GL parameter κ. Also, the values extrapolated to T_c, when possible, are shown by arrows originating from the data points.

Figure 4.13 shows the phase diagram of critical fields versus the Ginzburg-Landau parameter κ plotted on a log-log scale (this is the same phase diagram as Fig. 2.1). Also shown in the same figure are the superheating field predicted by the one-dimensional GL theory, $h_{sh}(\equiv H_{sh}/H_c)$* and the fluctuation-limited superheating field estimated by Kramer (K3, see Sec. 2.2.4), H_{s1}/H_c. As can be seen, the present results on both alloys show a fair agreement with the superheating field in both type I and type II regimes where the following conclusions are obtained.

Type I

In this region the rf critical field is not limited by the thermodynamic critical field but rather by the superheating field determined from the one-dimensional GL theory. The results from lead discussed in Chapter 3 give more support for this conclusion. This is the first time**, to the author's knowledge, that rf critical fields approaching the superheating field have been systematically observed in experiments involving type I superconductors.

Transition Region from Type I to Type II

The rf critical fields that can be attained show no significant discontinuity at $\kappa = 1/\sqrt{2} = 0.707$ where the transition from type I to type II superconductivity takes place. This is unlike the situation

---

*The numerical values of h_{sh} were obtained by reading the graph given in M5 for $\kappa \gtrsim 0.25$ and by the analytic expression for small κ given in P13 for $\kappa \lesssim 0.25$.

**Except for the single instance where an rf superheating in lead (by 25%) was reported at 4.2°K (F3).

in the static field where the two critical fields H_{c1} and H_{c2} separate the three possible phases, and it is again consistent with the superheating field which is continuous across the boundary.

Type II

In this regime a total of 7 alloy samples (2 SnIn and 5 InBi samples) were used in the rf measurements. All of the samples showed rf critical fields higher than the first critical field H_{c1} and all of them, except one, showed h_c^{rf} equal to or higher than the thermodynamic critical field. Thus it is concluded that the lower critical field does not limit the attainable rf fields. This is consistent with the previous measurements made on niobium (S4) and the alloys such as Nb_3Sn (P10) and $Nb_{0.4}Ti_{0.6}$ (G7).

The cause for this behavior (h_c^{rf} above h_{c1}) was previously attributed (H10) to the time it takes to nucleate a flux line at H_{c1} in type II superconductors. The nucleation time of a flux line was measured (F7) to be on the order of 10^{-6}sec which is long compared with the present rf period ($\sim 10^{-8}$sec for this study).

The uppermost limit of the rf critical field for the present type II superconductors is placed by the superheating field rather than the thermodynamic critical field, although the results are somewhat on the borderline of the absolute experimental error. This is again the first observation of h_c^{rf} equal to or higher than h_c for type II superconductors. The difference between the one-dimensional superheating field, h_{sh}, and the fluctuation-limited superheating field (h_{sl} shown by a dashed line in the figure) is too small to be distinguished, based on the present experimental results. Also, the time scale in which h_{sl}

becomes effective is not established so that the comparison of h_{sl} to h_c^{rf} is somewhat ambiguous. Therefore this point is an open question at this stage.

4.3.3 Frequency Dependence of RF Critical Field

The rf critical fields were also measured at 300 MHz by exciting the fourth mode of the helical resonator where the rf magnetic field was reasonably uniform over the dimension of the sample. The results obtained at 300 MHz are compared with those obtained at 90 MHz in Fig. 4.14 for four samples. It can be seen that the rf critical field is generally insensitive to the frequency in this range, varying by up to 10% over the frequency change of a factor of 3.*

This relative insensitivity of h_c^{rf} to the frequency of the magnetic field suggests that the nucleation time of the normal phase, once the critical field is reached, is much shorter than the typical rf period used in the experiment. There has been a very limited amount of work with regard to the nucleation time of the normal phase, particularly in the superheated state as found in the present experiment. According to one recent experiment (V2) on small spheres of mercury in the superheated state, the nucleation time was estimated to be 4×10^{-11}-10^{-12}sec which is much smaller than the present rf period of 10^{-8} - 3×10^{-9}sec.

*The lower h_c^{rf} at 300 MHz may be due to a localized heating at the site of nucleation, as the superconducting surface resistance varies as $\sim f^2$. However, the magnitude of the effect (0-10%) and the relative uncertainties in the determination of the rf magnetic fields at two different frequencies ($\sim$ 12%) do not warrant any definite conclusion in this regard.

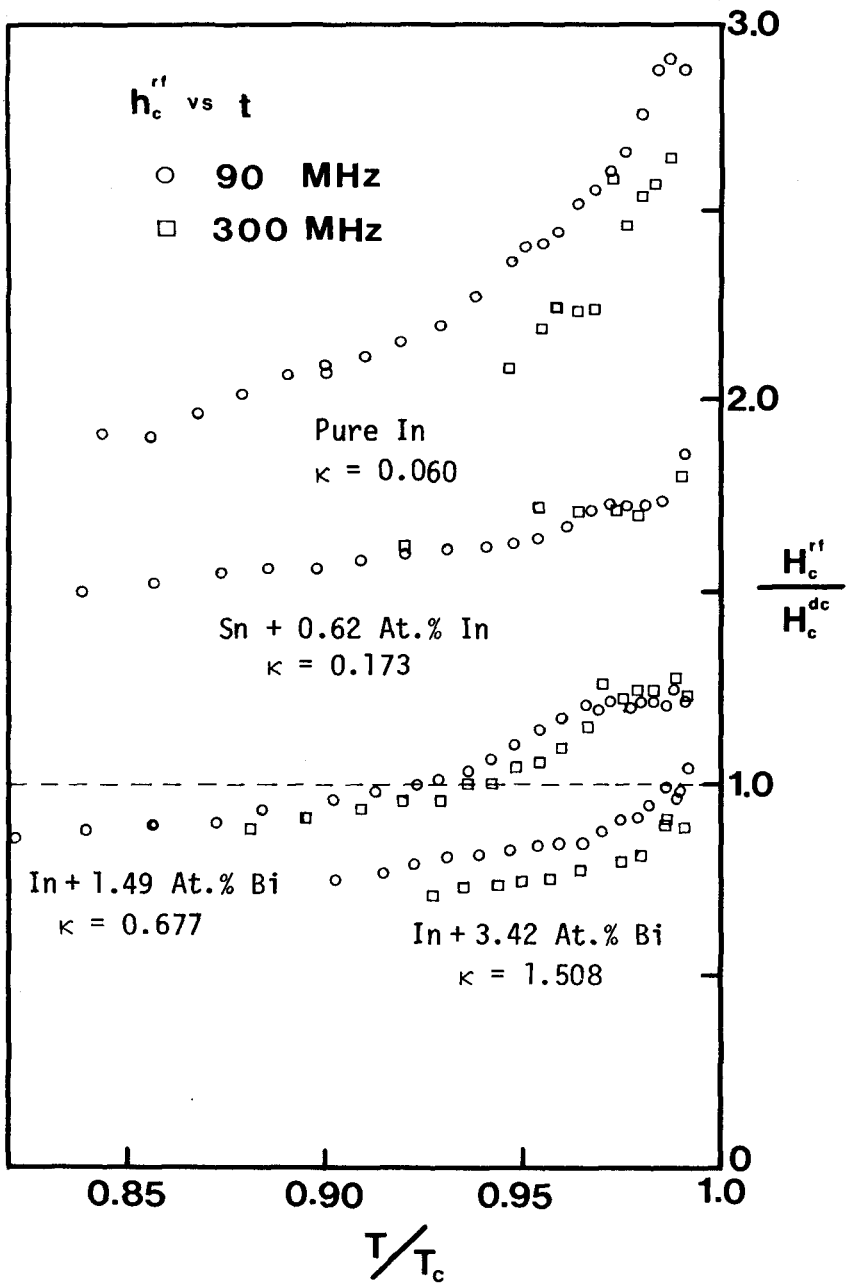

Fig. 4.14 The rf critical fields measured at two frequencies, 90 and 300 MHz are shown for four samples.

Theoretically the situation is even more uncertain. Nevertheless an order of magnitude estimate can be obtained from the characteristic time for the variation of the order parameter, τ_{GL}, which appears in the time-dependent Ginzburg-Landau theory (A4, and Y2, p.22) as

$$\tau_{GL} = \frac{\pi \hbar}{8kT_c(1-t)} \tag{4.34}$$

This gives for the present temperature range of $0.8 \lesssim t \lesssim 0.99$

$$5 \times 10^{-12} \lesssim \tau_{GL} \lesssim 10^{-10}$$

which again is much smaller than the present rf period of measurement.

These estimates, incidentally, justify the use of the ordinary (time-independent) GL theory in the frequency range used in the present experiment and at the same time may account for a generally good agreement between the present rf results and the prediction of the GL superheating theory.

4.4 Conclusions

The rf critical magnetic fields were measured at 90 MHz for pure tin and indium, and for a series of SnIn and InBi alloys spanning both type I and type II superconductivity. The results of pure samples of tin and indium showed that a vortex-like nucleation of the normal phase was responsible for the superconducting-to-normal phase transition in the rf field at temperatures up to about 0.98-0.99 T_c, where the ideal superheating limit was being reached. The results of the alloy samples

showed that the attainable rf critical fields near T_c were well described by the superheating field predicted by the one-dimensional Ginzburg-Landau theory in both the type I and type II regimes. The measurement was also made at 300 MHz resulting in no significant change in the rf critical field. Thus it was inferred that the nucleation time of the normal phase, once the critical field was reached, was small compared with the rf period in this frequency range.

Appendix A

THE RESIDUAL LOSS DUE TO TRAPPED FLUX

If a resonator is cooled through its transition temperature in the presence of a static magnetic field, the walls of the resonator tend to trap magnetic flux. Since the cores of the trapped flux are normal-conducting, they will dissipate energy when an rf current flows on the surface of the resonator. This loss mechanism can be characterized by an effective surface resistance, R_H , which is a function of the applied magnetic field, H_{dc}, and temperature, T , when measured at low rf field level. Since the shielding of the earth's magnetic field is not always complete in a low temperature dewar apparatus, it is of practical interest to determine the magnitude of R_H and its dependence on the applied field and temperature.

The effect of a static magnetic field on the residual surface resistance was investigated by slowly cooling the cavity through the transition temperature of lead while a constant magnetic field was present. The dc magnetic field was applied horizontally (perpendicular to the axis of the coaxial resonator) by a pair of Helmholtz coils while the vertical component of the earth's magnetic field was cancelled down to about 15 milligauss by another pair of Helmholtz coils. The uniformity of the applied field above 0.2 gauss was within 10% over the entire region of the cavity.

The temperature dependence of cavity Q was measured for the applied field ranging from 0 up to 8 Gauss. Assuming that all the applied magnetic flux which intercepts the cavity surface is trapped, the

partial geometrical factor,* Γ_H , may be calculated using the known current distribution as discussed in Sec. 3.2.1. It was found to be $Q_o R_H = \Gamma_H = 13$ ohms. Then the effective surface resistance is given by

$$R_H(H_{dc},T) = \Gamma_H[Q_o^{-1}(H_{dc},T) - Q_o^{-1}(0,T)] \qquad (A.1)$$

where $Q_o^{-1}(0,T)$ is the result in a zero applied field.

The dependence of R_H on temperature was found to be

$$R_H(T) = \frac{R_H(0)}{(1 - t^2)^{3/2}} \qquad (A.2)$$

where $t = T/T_c$ with $T_c = 7.18°K$ for lead. This temperature dependence holds for the entire H_{dc} range studied as shown in Fig. A.1. This is distinguishably different from the functional form observed for the same loss mechanism by Victor and Hartwig (V1) which is

$$R_H = \frac{R_H(0)}{(1 - t^4)^{1/2}\,(1 - t^2)} = \frac{R_H(0)}{(1 - t^2)^{3/2}\,(1+t^2)^{1/2}} \qquad (A.3)$$

in the same frequency range for a rolled foil resonant circuit.

The presently observed temperature dependence may be explained by a simple model where the dissipation is proportional to the effective volume of the normal region through which a current can flow. The conservation of flux requires that the fraction of the normal surface

---

*The partial geometrical factor, Γ_H, is defined in an analogous manner as the geometrical factor Γ in Eq. (3.7) except the surface integral is now over the effective surface area instead of the entire area.

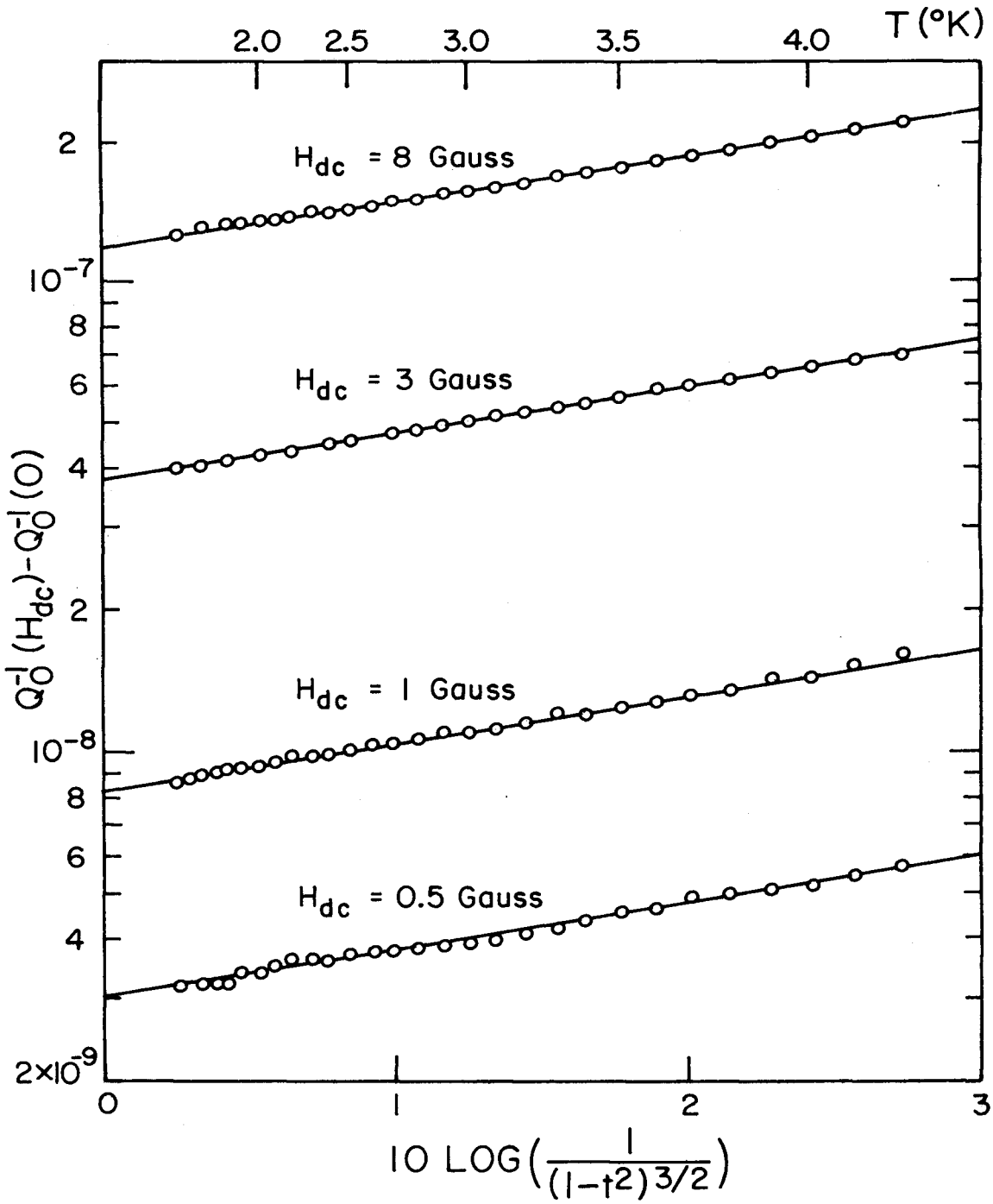

Fig. A.1 The quantity, $Q_o^{-1}(H_{dc}) - Q_o^{-1}(0)$, which is proportional to the effective surface resistance induced by the presence of trapped flux is shown as a function of the characteristic temperature quantity of the present trapped flux model.

area is proportional to $H_{dc}/H_c(T)$ at all temperatures. If we assume that the depth to which the current can flow is limited by the typical dimension of each flux tube, then the volume, V_{eff}, in which the dissipation is effective is proportional to

$$V_{eff} \propto \text{normal area} \times \text{depth}$$

$$\propto \pi r^2 \times r = \pi r^3$$

where r is the radius of a typical flux tube. Since $\pi r^2 \propto H_{dc}/H_c(T)$ we have

$$R_H \propto V_{eff} \propto (H_{dc}/H_c(T))^{3/2}$$

$$\propto (H_{dc}/H_c(0))^{3/2} (1 - t^2)^{-3/2} \qquad (A.4)$$

where the usual parabolic law for the critical field is used. Below H_{dc} of 1 gauss, R_H was seen to depend on $H_{dc}^{3/2}$ as shown in Fig. A.2. Also the above expression gives the observed temperature dependence.

However, in order to obtain the proportionality constant in the above equation we need a detailed knowledge of the intermediate state (e.g., the size of a typical flux tube) which cannot be uniquely calculated with the present experimental configuration. We can nevertheless determine the proportionality constant empirically in the above model from the experimental data. For the 10μ surface studied it was found to be

$$R_H = 1.13 \times 10^{-7} \left(\frac{H_{dc}}{1 - t^2}\right)^{3/2} \Omega \qquad (A.5)$$

where H_{dc} is expressed in gauss. Thus, for example, in the earth's

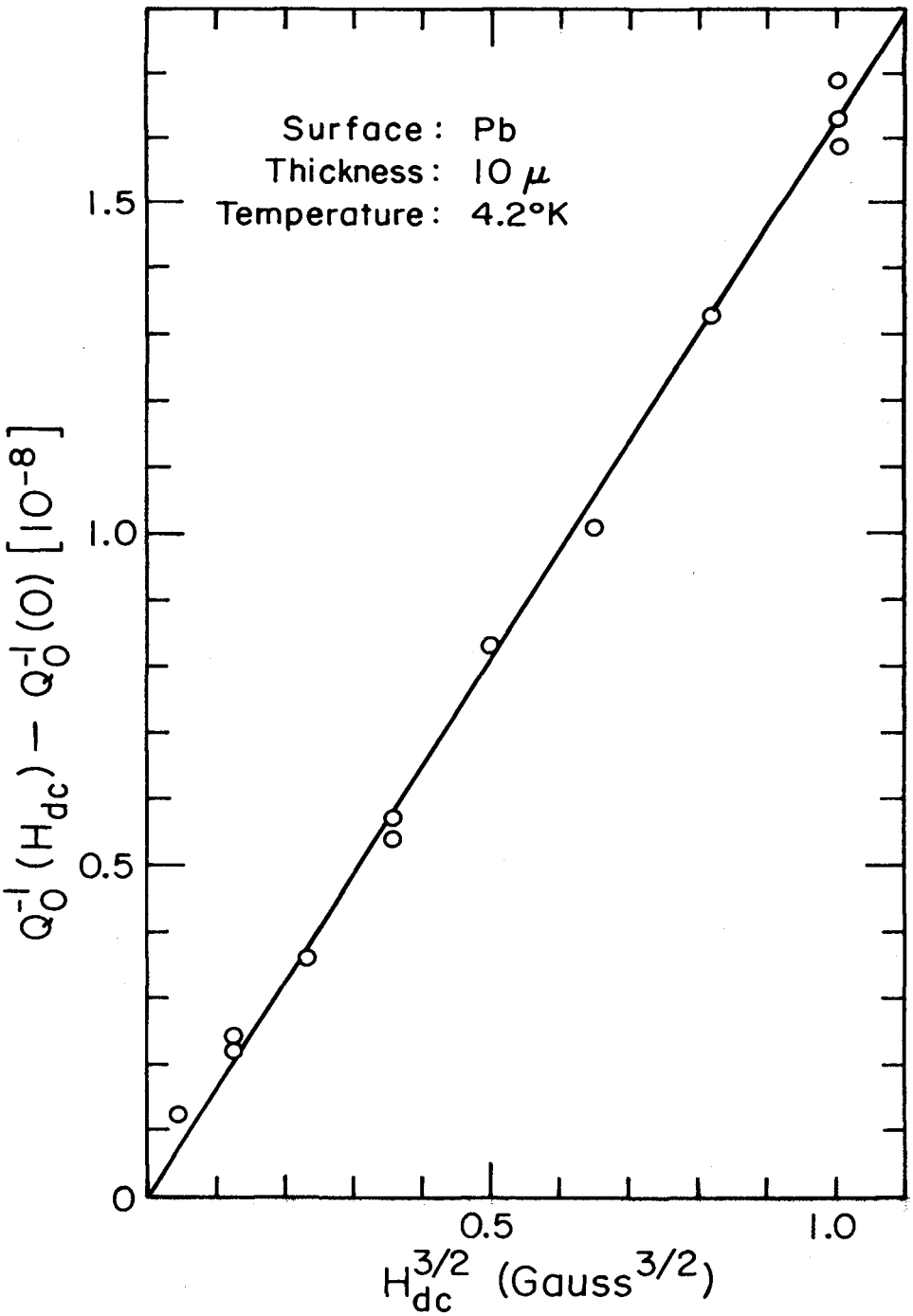

Fig. A.2 $Q_o^{-1}(H_{dc} - Q_o^{-1}(0)$ (proportional to the effective surface resistance due to trapped flux) is shown as a function of $H_{dc}^{3/2}$ where H_{dc} is the static field present when the resonator was cooled through its transition temperature.

magnetic field of 0.5 gauss, we have

$$R_H(T = 0\ °K) = 4.0 \times 10^{-8}\Omega \tag{A.6}$$

which is approximately the same as the BCS surface resistance at 4.2°K. In a typical dewar apparatus with a mu-metal magnetic shield the remnant magnetic field is below 10 milligauss so that

$$R_H(T = 0\ °K) \leq 1.13 \times 10^{-10}\Omega \tag{A.7}$$

which is totally negligible compared with R_{BCS} (4.2°K).

Aside from the remnant magnetic field there is a possibility of a thermoelectrically generated magnetic field (P11) which may be trapped during the cooling process. In the worst case of this process Pierce suggested a field up to 100 milligauss. Even in this case

$$R_H(T = 0\ °K) = 3.6 \times 10^{-9}\Omega \tag{A.8}$$

and this is about an order of magnitude smaller than the observed residual resistance in this experiment (R_{res} = 2-5 $\times 10^{-8}\Omega$).

The dependence of R_H on H_{dc} above 2 gauss was found to be approximately linear as shown in Fig. A.3. However, the temperature dependence remains essentially the same as for the lower fields. This discrepancy cannot be explained in the present model. The exact cause of this behavior is difficult to determine due to several possible complications such as (1) the demagnetizing effect of the complicated surface geometry of the present resonator, (2) the size effect due to surface roughness as previously advanced by Pierce (P11), and (3) the

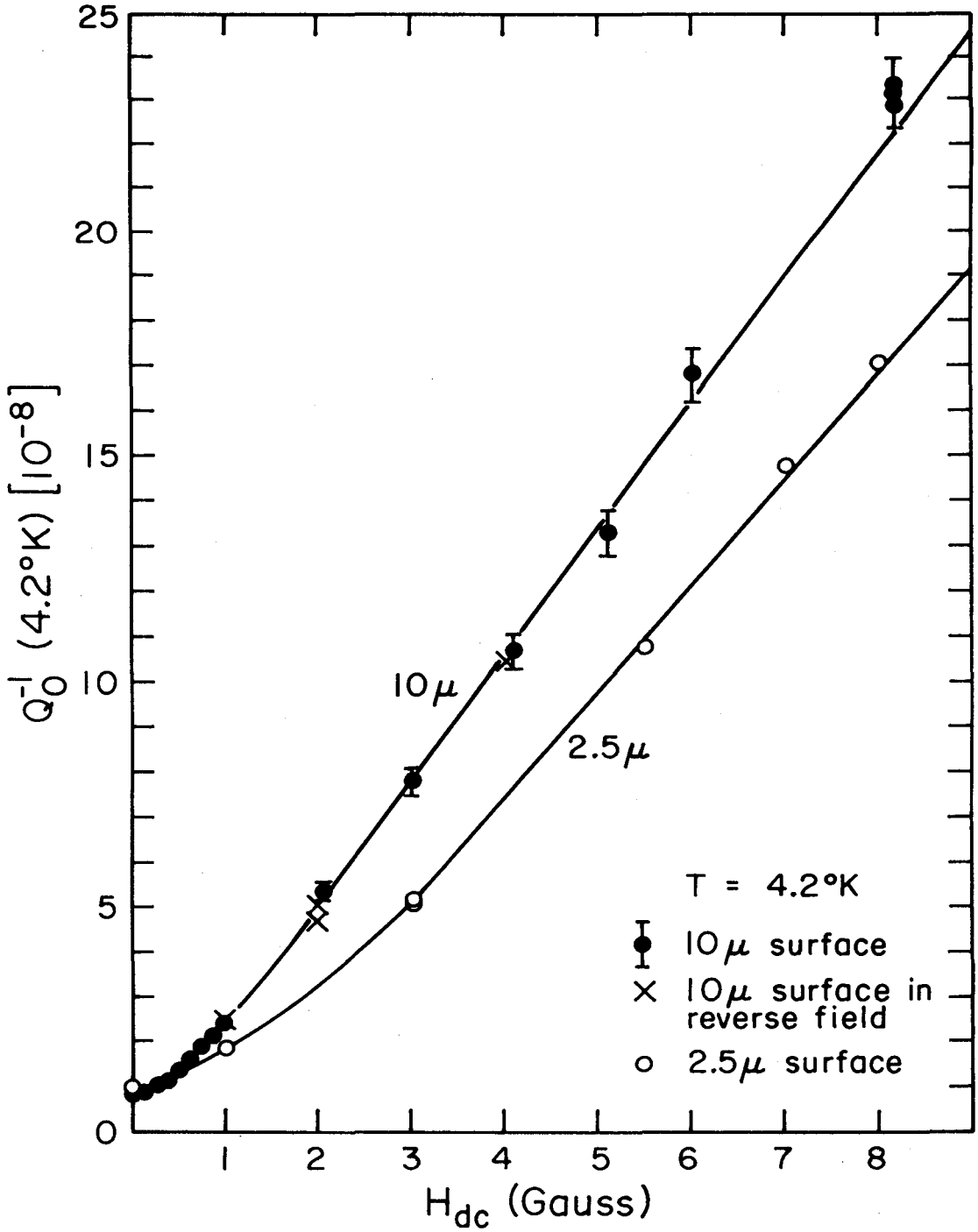

Fig. A.3 The reciprocal of Q_o measured at 4.2°K is shown for two surfaces examined as a function of the static magnetic field, H_{dc}, which was present during the cooling process.

intermediate state structure which is not known a priori. Thus in order to obtain a more definitive answer, it is necessary to design an experiment for this purpose only, where the intermediate state can be observed directly.

Finally, it should be pointed out that the loss due to trapped flux is not well understood in low frequency resonators (order of 100 MHz) as reported by Piosczyk et al. for niobium helical resonators (P9). They report a complicated dependence of R_H on temperature as well as on the rf magnetic field, which is in contrast to the loss due to the same mechanism in GHz region where the loss is well described by the dissipation in the "quasi-normal cores" of fluxoids.

Appendix B

SURFACE RESISTANCE OF LEAD AT HIGH RF MAGNETIC FIELD LEVEL

The surface resistance of superconducting lead of various thicknesses was investigated at rf magnetic field levels comparable to the thermodynamic critical field. The thicknesses of 0.3, 1.45, 6 and 14 microns were obtained by varying the deposition time at constant current density in the electroplating. For each thickness the resonator quality factor, Q_o, was measured as a function of the rf magnetic field at two temperatures (4.2 and 2.2°K). The surface resistance was observed to increase with rf field level for all the surfaces examined. A typical manner of this increase is shown in Fig. B.1, where the reciprocal of Q_o (proportional to the surface resistance) is shown as a function of the rf magnetic field, H_{max}, at the midsection of the center conductor. The general features are characterized by an initial slow increase followed by a rapid increase near H_c.

In analyzing this behavior ($Q_o^{-1}(H_{max},T)$ versus H_{max}), it was found that the expression

$$Q_o^{-1}(H_{max},T) = Q_o^{-1}(0,T)\left(1 + a\left(\frac{H_{max}}{H_c(T)}\right)^n\right) \quad \text{below } H_{tr} \qquad (B.1)$$

with $n \simeq 2.0$ described the behavior below a certain field H_{tr} well. Here $H_c(T)$ is the thermodynamic critical field of lead, and a and n are the parameters to be determined for every surface. The justification of this form will be given later, and the meaning of H_{tr} will soon become clear. The parameters a and n were found by plotting

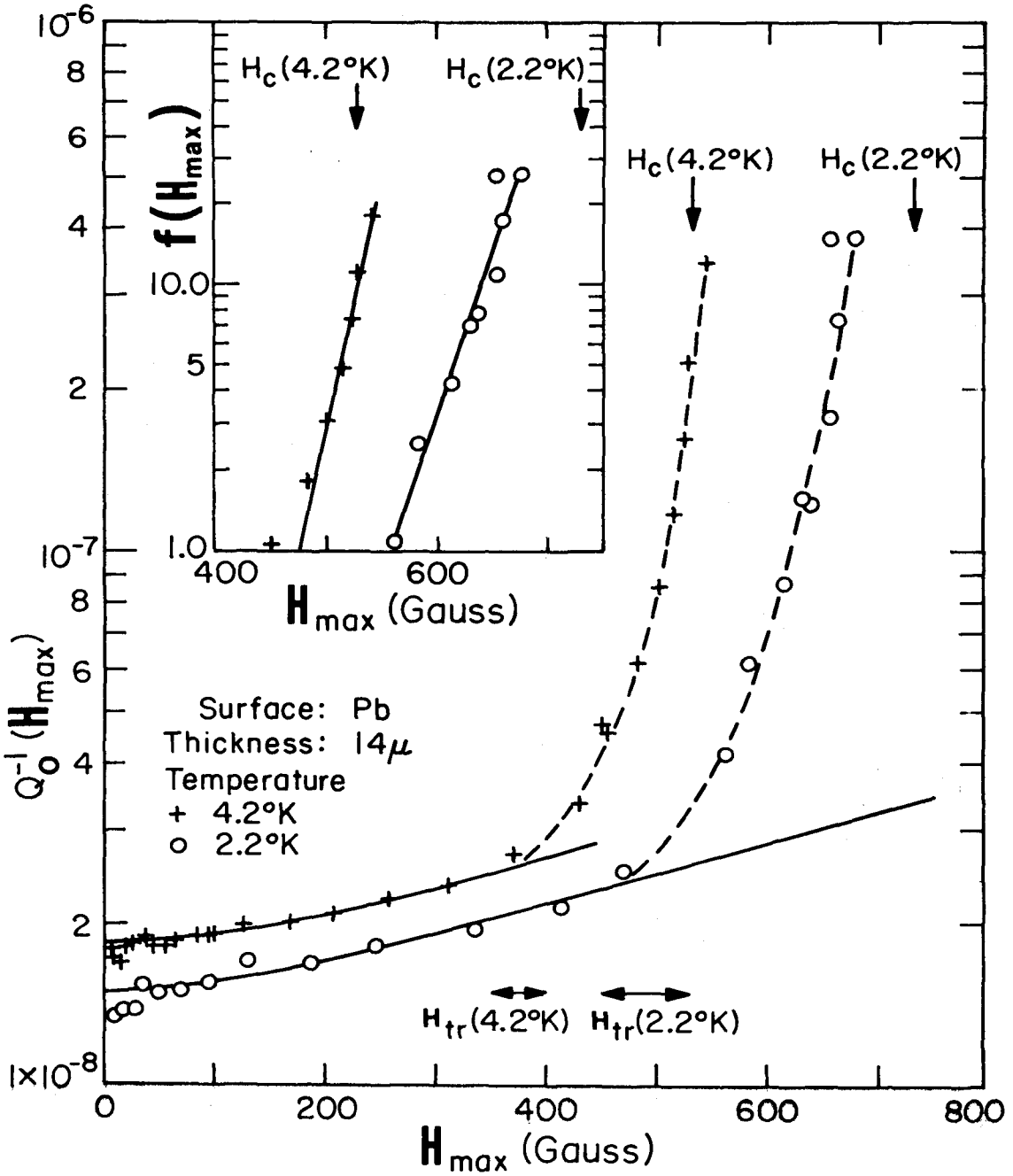

Fig. B.1 The reciprocal of Q_o (proportional to the surface resistance is shown as a function of the magnetic field, H_{max}, at the midsection of the center conductor. The solid lines are the power-law fit to the experimental data below H_{tr}. The inset shows the additional dissipation above H_{tr}.

$$\frac{Q_o^{-1}(H_{max},T) - Q_o^{-1}(0,T)}{Q_o^{-1}(0,T)} \quad \text{versus} \quad H_{max}$$

on a log-log plot and drawing a straight line in the portion where the slope was constant. Examples of the term thus determined are shown as solid curves, together with experimental points in Fig. B.1, where H_{tr} can be seen as the field at which the experimental points start deviating from this simple power law term (i.e., transition from one behavior to another). Above H_{tr} the increase in Q_o^{-1} is much more rapid than the H_{max}^2 term. Taking the difference between the experimental points and the extrapolated values of H_{max}^n term above H_{tr}, we define $f(H_{max})$ by

$$f(H_{max}) \equiv \frac{Q_o^{-1}(H_{max},T)}{Q_o^{-1}(0,T)} - \left(1 + a\left(\frac{H_{max}}{H_c(T)}\right)^n\right) \quad \text{above } H_{tr} \qquad (B.2)$$

which is a measure of the additional loss above H_{tr}.

With the above procedure, a, n, H_{tr} and $f(H_{max})$ were found for every surface examined. The values of a, n, and H_{tr} are listed in Table B.1.

Before discussing the significance of these parameters we need to look at the real surfaces of lead for different thicknesses. Direct observation under a microscope shows that there are at least two kinds of surface imperfections:

(1) The first kind is the imperfect plating at the grain boundaries of the copper substrate. This is particularly pronounced for large-grained substrate as shown in Fig. B.2a, which shows a discontinuity in surface

Table B.1 The parameters, a, n, and H_{tr}, determined by the present analysis are shown for all surfaces studied at two temperatures.

Temp. °K	$H_c(T)$ gauss	Thickness or Pb Layer μ	$Q_o^{-1}(0,T)$ 10^{-8}	a	n	H_{tr} gauss	H_c^{rf} gauss
4.20	528	0.3	2.04	3.83	1.84 ± 0.21	580 ± 20	627
		1.45	2.08	2.07	2.61 ± 0.46	510 ± 20	600
		6.0	1.36	1.77	1.96 ± 0.26	400 ± 20	580
		14	1.77	0.76	1.77 ± 0.15	375 ± 25	566
2.20	728	0.3	1.02	4.42	1.88 ± 0.21	740 ± 20	791
		1.45	1.18	4.46	2.25 ± 0.28	690 ± 20	734
		6.0	0.80	3.83	2.05 ± 0.32	575 ± 25	717
		14	1.36	1.38	1.66 ± 0.39	490 ± 40	681

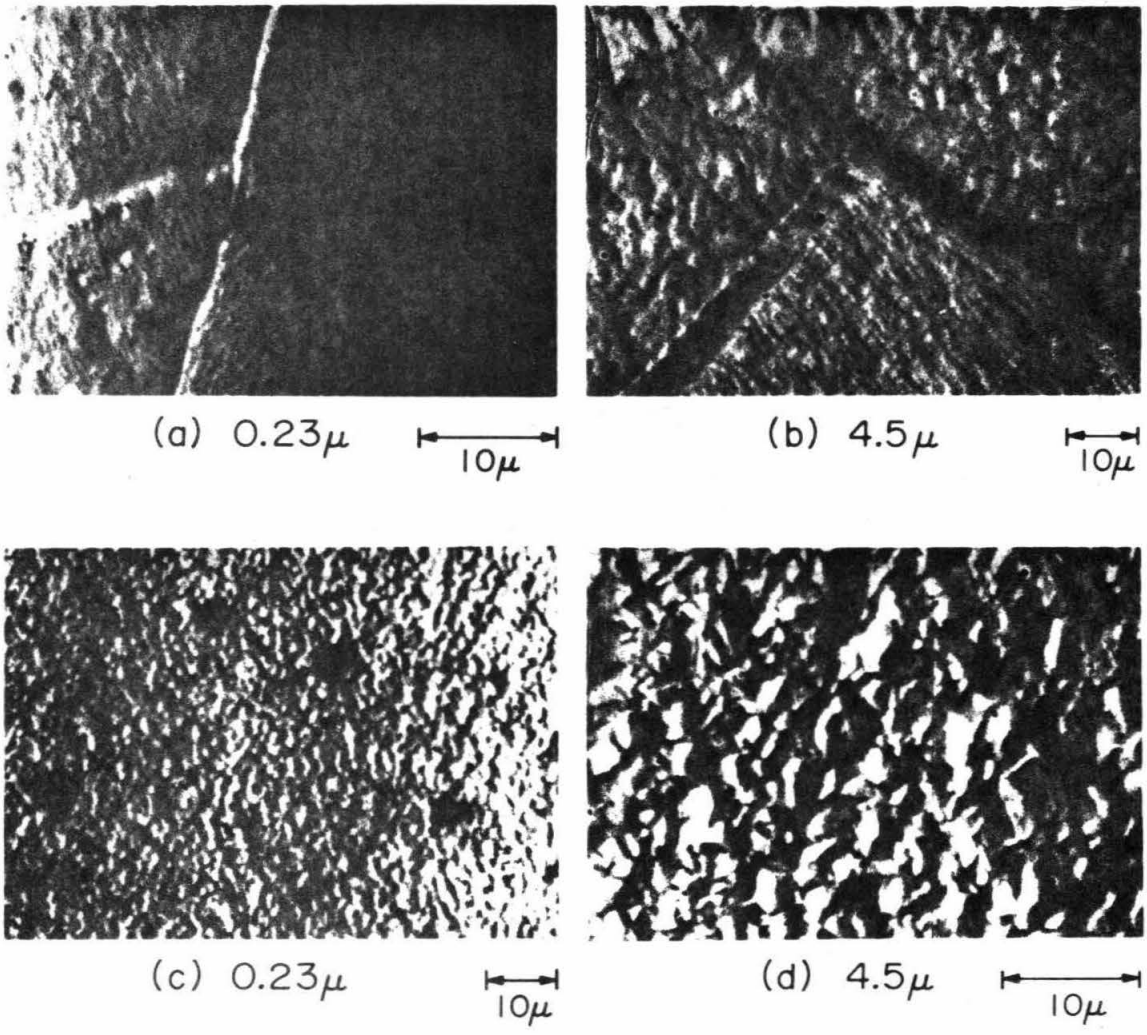

Fig. B.2 The surface of electroplated lead is shown for a large-grained copper substrate (a,b) and for a fine-grained copper substrate (c,d). For both types of substrates, the thin lead film replicates the substrate, whereas the thicker lead film tends to develop its own surface structures.

texture. Also distinct edges develop as the thickness of the plated layer increases as shown in Fig. B.2b.

(2) The second kind is the rough surface features that tend to develop as the thickness increases. At low coverage the surface of lead tends to replicate the substrate (see Fig. B.2a and c). As the thickness of the plated layer increases, the lead surface develops its own structure such as protrusions and sharp corners as can be seen in Fig. B.2b and d. Once these observations are noted we can proceed to discuss the increase in surface resistance at high field levels. This can best be done in two separate field ranges.

Below H_{tr}

We have noted that the observed increase in surface resistance is given by

$$\frac{Q_o^{-1}(H_{max},T) - Q_o^{-1}(0,T)}{Q_o^{-1}(0,T)} = a\left(\frac{H_{max}}{H_c(T)}\right)^n \qquad (B.3)$$

For all the surfaces examined it was found that n was very close to 2.0 ($1.66 \leq n \leq 2.61$, see Table B.1).

It is proposed that this portion of the additional loss is associated with localized defective areas or weakly superconducting regions that are located at or near the grain boundaries of the substrate. The proportionality to H^2 can be seen in the following simplified argument.

The power dissipated in a localized defect is given by

$$P_{diss} = \frac{1}{2} \int_{defect} R_d H^2 \, dA = \frac{1}{2} R_d H^2 A_d \qquad (B.4)$$

where R_d and A_d are, respectively, the effective surface resistance and the area of the defect. Now this dissipation raises the temperature T of the surrounding area above the bath temperature T_b by an amount

$$\Delta T = T - T_b = P_{diss}/K$$

where K is the effective thermal conductivity between the lead film and the substrate. Then the surface resistance of the surrounding area is given by

$$\begin{aligned} R(T) &= R(T_b) + \frac{dR}{dT}\Big|_{T_b} \Delta T \\ &= R(T_b) + \frac{1}{2}\frac{dR}{dT}\Big|_{T_b} \frac{R_d A_d}{K} H^2 \end{aligned}$$

or
$$R(T) - R(T_b) = \left(\frac{1}{2K} R_d A_d \frac{dR}{dT}\Big|_{T_b}\right) H^2 \qquad (B.5)$$

Since Q_o^{-1} is proportional to the surface resistance R we have

$$\frac{Q_o^{-1}(H,T) - Q_o^{-1}(0,T)}{Q_o^{-1}(0,T)} \propto H^2 \qquad (B.6)$$

where it is assumed that the area at the elevated temperature remains constant.

The coefficient, a, in front of H_{max}^n in this picture will be proportional to the density of defect sites which is expected to decrease as the thickness increases, since smaller defects will be covered as the lead layer builds up. The coefficient, a, was indeed observed to decrease with thickness as shown in Table B.1 .

Another support for the above interpretation in terms of localized heating comes from the fact that heating of the entire surface cannot account for the observed increase in the dissipation. The global heating is another possible mechanism (H8) in which the total power dissipated within the resonator raises the overall temperature of the resonator with a resultant increase in surface resistance, which is also proportional to H^2. The temperature rise of the cavity surface in this scheme was calculated using the measured power dissipation in the cavity and the known thermal conductivity of the copper substrate. The expected increase in Q_o^{-1} thus calculated was smaller than the observed increase by typically more than two orders of magnitude which clearly indicated that the global heating was not the cause of the increase in surface resistance.

Above H_{tr}

At the transition field H_{tr} an additional loss mechanism enters that enhances the surface resistance or, equivalently, increases Q_o^{-1}. This additional mechanism can be characterized by Eq. (B.2) for $f(H_{max})$ which was found to be almost exponential in H_{max} as shown in the inset of Fig. B.1. In this figure $f(H_{max})$ is shown for two temperatures, 4.2 and 2.2°K and the arrows show the thermodynamic critical fields of lead at the respective temperatures. Their approximate correlations suggest that this additional loss mechanism is related to the critical magnetic field. A plausible phenomenological explanation for this mechanism is as follows. Since the surface magnetic field is enhanced by surface structures such as protrusions and sharp corners (see photographs in

Fig. B.2), it is possible to reach the rf critical magnetic field of lead locally at these structures. Once this field is reached locally it will give rise to "quasi-normal" regions (HlO) which contribute to the increase in surface dissipation.

This explanation, although extremely qualitative in nature, is supported by the observation that H_{tr} (Table B.1) is lower for thicker films, i.e., this additional loss mechanism comes into effect at lower field for thicker films, since there are more surface structures in these films that enhance the surface magnetic field locally. Exactly the same argument applies for the upward trend in $f(H_{max})$ as the film thickness increases as shown in Fig. B.3.

All the above features are summarized in the diagram shown in Fig. B.4 where the transition field, H_{tr}, and the rf critical field, H_c^{rf}, are plotted as a function of the thickness of the lead film. The area below H_{tr} is characterized by the fact that the additional surface resistance is proportional to H^2. All the observations made suggest that this is due to a localized heating at defect sites such as at grain boundaries of the substrate. In the region between H_{tr} and H_c^{rf} the additional surface resistance is dominated by the surface structures of the lead surface. As a reference the thermodynamic critical field of lead is shown by a dashed line. It clearly shows that the superconducting state can persist above the thermodynamic critical field at this frequency.

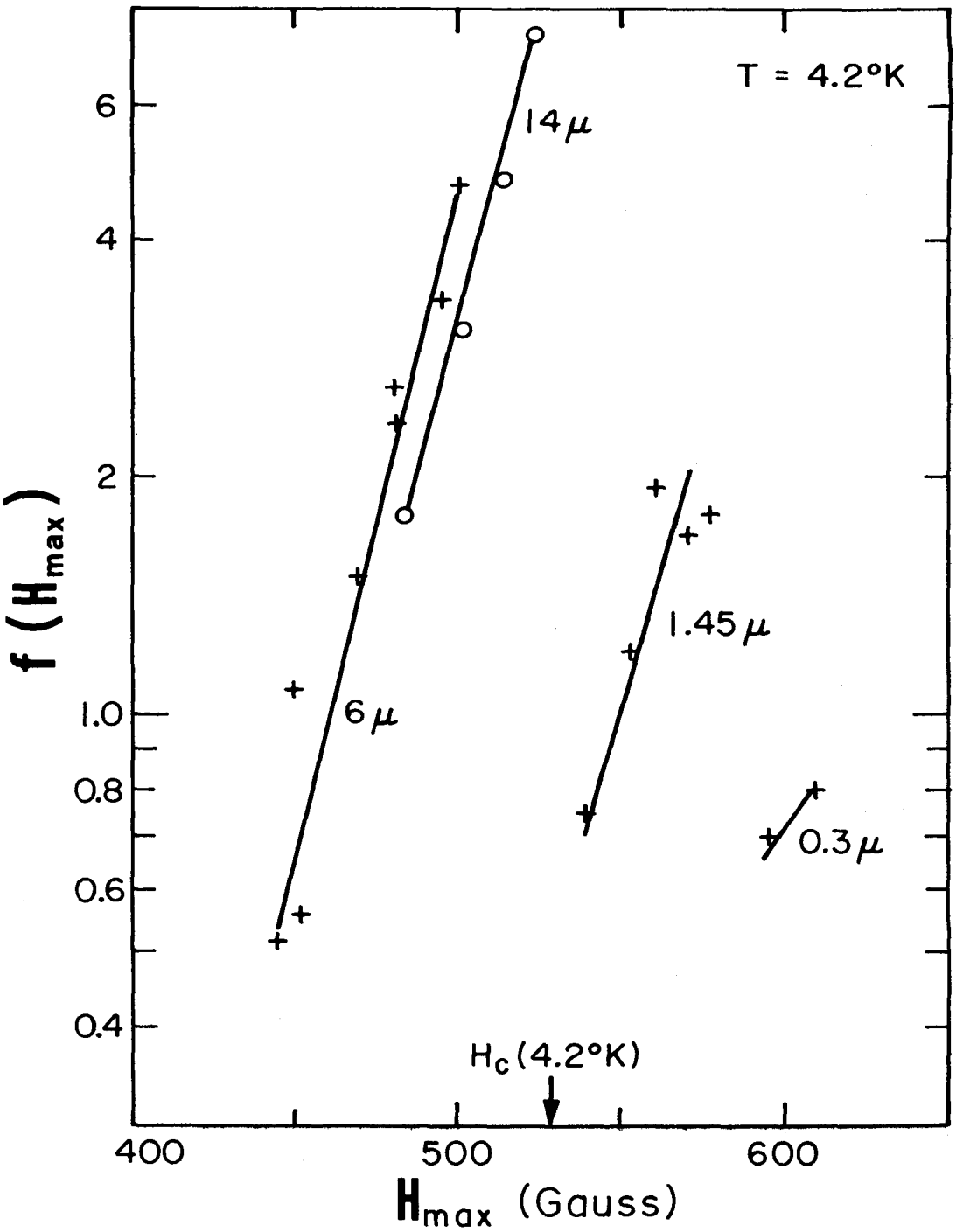

Fig. B.3 The quantity f (Eq. (B.2)) is shown as a function of H_{max} for different surfaces at 4.2°K. This quantity is a measure of the additional loss mechanism above H_{tr}.

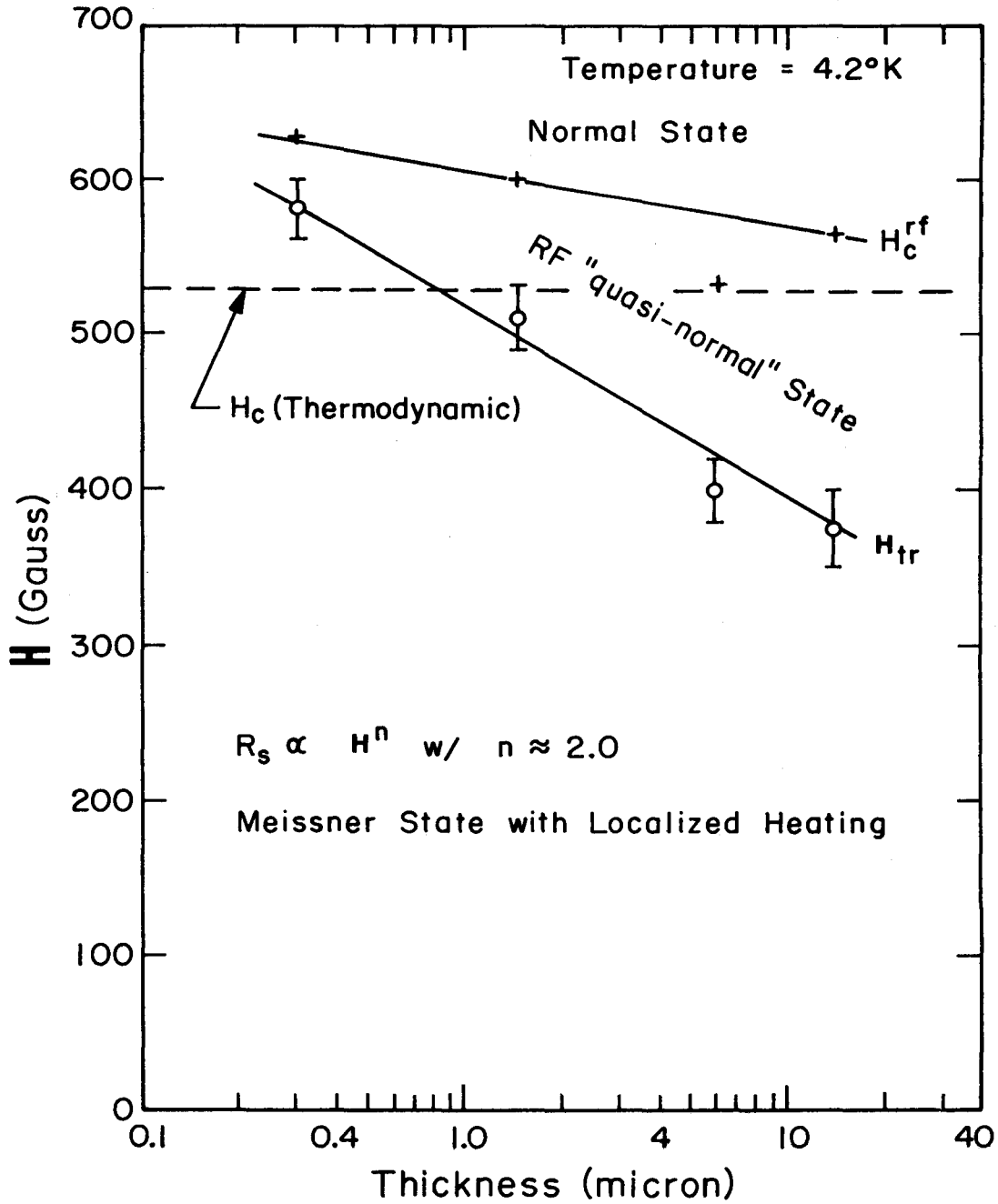

Fig. B.4 The transition field, H_{tr}, and the rf critical field, H_c^{rf}, are shown as a function of the film thickness.

BIBLIOGRAPHY

DeGennes, P. G., Superconductivity in Metals and Alloys, W. A. Benjamin, Inc., New York, 1966.

Goodstein, D. L., States of Matter, Prentice-Hall, Inc., New Jersey, 1975.

London, F., Superfluids, Vol. 1, John Wiley and Sons, Inc., New York, 1950.

Lynton, E. A., Superconductivity, 3d ed., Methuen and Co., Ltd., London, 1969.

Newhouse, V. L., Applied Superconductivity, John Wiley and Sons, Inc., New York, 1964.

Parks, R. D. (ed.), Superconductivity, Vols. I and II, Marcel Dekker, Inc., New York, 1969.

Rickayzen, G., Theory of Superconductivity, John Wiley and Sons, Inc., New York, 1965.

Rose-Innes, A. C., and F. H. Rhoderick, Introduction to Superconductivity, Pergamon Press, New York, 1969.

Saint-James, D., G. Sarma, and E. J. Thomas, Type II Superconductivity, Pergamon Press, New York, 1969.

Shoenberg, D., Superconductivity, Cambridge University Press, New York, 1952.

Tinkham, M., Introduction to Superconductivity, McGraw-Hill, Inc., New York, 1975.

REFERENCES

A1 A. A. Abrikosov, L. P. Gor'kov and I. M. Khalatnikov, Sov. Phys. JETP 10, 132-134 (1960).

A2 A. A. Abrikosov, L. P. Gor'kov and I. M. Khalatnikov, Sov. Phys. JETP 8 , 182-189 (1959).

A3 A. A. Abrikosov, Sov. Phys. JETP 5, 1174-1182 (1957).

A4 Elihu Abrahams and Toshihiko Tsumeto, Phys. Rev. 152, 416-432 (1966).

B1 J. Bardeen, L. N. Cooper and J. R. Schrieffer, Phys. Rev. 108, 1175-1204 (1957).

B2 F. E. Borgnis and C. H. Papas, Handbuch der Physik, Vol. XVI, Springer-Verlag, Berlin (1958), "Electric Fields and Waves", pp. 285-422.

B3 A. P. Banford, Adv. Cryog Eng. 10, 80-87 (1965).

B4 Y. Bruynseraede, D. Gorle, D. Leroy and P. Morignot, Physica 54, 137-159 (1971).

B5 J. C. Blade and E. C. Ellwood, J. Inst. Metals 85, 30-32 (1956-1957).

B6 C. A. Bryant and P. H. Keesom, Phys. Rev. 123, 491-499 (1961).

B7 C. P. Bean and J. D. Livingston, Phys. Rev. Lett. 12, 14-16 (1964).

C1 R. G. Chambers, Proc. Roy. Soc. (London) A215, 481-497 (1952).

C2 E. DiCrescenzo, P. L. Indovina, S. Onori and A. Rogani, Phys. Rev. B7, 3058-3065 (1973).

D1 J. R. Delayen, H. C. Yen, G. J. Dick, K. W. Sheppard and J. E. Mercereau, IEEE Trans. Mag. MAG-11, 408-410 (1975).

D2 J. R. Delayen and G. J. Dick, Internal Report HPS-1, Low Temp. Physics, Caltech (1973).

D3 H. van Dijk, M. Durieux, J. R. Clement, and J. K. Logan, NBS Monograph 10, June 17, 1960.

F1 T. E. Faber and A. B. Pippard, Proc. Roy Soc. A231, 336-352 (1955).

F2 H. J. Fink and A. G. Presson, Phys. Rev. 182, 498-503 (1969).

F3 P. Flécher et al., IEEE Trans. Nucl. Sci. NS-16, 1018-1022 (1969).

F4 D. K. Finnemore and D. E. Mapother, Phys. Rev. 140, A508-A518 (1965).

F5 T. E. Faber, Proc. Roy. Soc. A241, 531-546 (1957).

F6 J. Feder and D. S. McLachlan, Phys. Rev. 177, 763-776 (1969).

F7 R. B. Flippen, Phys. Lett. 17, 193 (1965).

G1 V. L. Ginzburg and L. D. Landau, Zh. Eksperim. i. Theor. Fiz. 20, 1064-1082 (1950).

G2 L. P. Gor'kov, Sov. Phys. JETP 36(9), 1364-1367 (1959).

G3 D. L. Goodstein, States of Matter, Prentice-Hall, Inc., New Jersey, 1975.

G4 V. L. Ginzburg, Sov. Phys. JETP 34, 78-87 (1958).

G5 M. P. Garfunkel and B. Serin, Phys. Rev. 85, 834-840 (1952).

G6 A. Kenneth Graham (ed.), Electroplating Engineering Handbook, Reinhold Book Corp., New York, 1962.

G7 S. Giordano, H. Hahn, H. J. Halama, T. S. Luhman and W. Bauer, IEEE Trans. Mag. MAG-11, 437-440 (1975).

G8 L. P. Gor'kov, Sov. Phys. JETP 10, 998-1004 (1960).

G9 B. B. Goodman, IBM Jour. 6, 63-67 (1962).

H1 J. Halbritter, Z. Phys. 266, 209-217 (1974).

H2 J. Halbritter, Externer Bericht 3/70-6 (1970).

H3 J. Halbritter, J. Appl. Phys. 42, 82-87 (1971).

H4 C. R. Haden and W. H. Hartwig, Phys. Rev. 148, 313-317 (1966).

H5 J. Halbritter, Z. Phys. 238, 466-476 (1970).

H6 J. Halbritter, IEEE Trans. Mag. MAG-11, 427-430 (1975).

H7 W. H. Hartwig and C. Passow, Vol. II, Chap. 8, Applied Superconductivity, ed. by V. L. Newhouse, Academic Press, New York, 1975.

H8 J. Halbritter, J. Appl. Phys. 41, 4581-4588 (1970).

H9 B. Hillenbrand, H. Martens, H. Pfister, K. Schnitzke and G. Ziegler, IEEE Trans. Mag. MAG-11, 420-422 (1975).

H10 J. Halbritter, in Proceedings of the 1972 Applied Superconductivity Conference, Annapolis, Md. IEEE Publ. No. 72CH0682-5-TABSC, IEEE, New York, 1972), p. 662-666.

H11 J. I. Harden and V. Arp, Cryogenics 3, 105-108 (1963).

H12 O. H. Henry and E. L. Badwick, Trans. Amer. Inst. Min. Met. Eng. 171, 389-395 (1947).

K1 E. P. Kartheuser and Sergio Rodriguez, Appl. Phys. Lett. 24, 338-340 (1974).

K2 L. Kramer, Z. Physik 259, 333-346 (1973).

K3 L. Kramer, Phys. Rev. 170, 475-480 (1968).

K4 T. Kinsel, E. A. Lynton and B. Serin, Rev. Mod. Phys. 36, 105-109 (1964).

K5 T. Kinsel, E. A. Lynton and B. Serin, Phys. Lett. 3, 30-32 (1962).

K6 I. Kirschner, J. Bankuti, Gy. Kiss, I. Kovacs, I. Laszloffy, Gy. Remenyi and K. Sajo, Sov. Phys. JETP 39, 1054-1058 (1974).

L1 H. London, Proc. Roy. Soc. A176, 522-533 (1940).

L2 H. London, Nature 133, 497-498 (1934).

L3 E. A. Lynton, Superconductivity, Methuen and Co., Ltd., London, 1969.

L4 F. and H. London, Proc. Roy. Soc. (London) A149, 71-88 (1935).

L5 F. London, Superfluids, Vol. I, Dover Publications, Inc., New York, 1961.

M1 E. Maxwell, P. M. Marcus and J. C. Slater, Phys. Rev. 76, 1332-1347 (1949).

M2 P. B. Miller, Phys. Rev. 118, 928-934 (1960).

M3 D. C. Mattis and J. Bardeen, Phys. Rev. 111, 412-417 (1958).

M4 W. Meissner and R. Ochsenfeld, Naturwissenschaften 21, 787-788 (1933).

M5 J. Matricon and D. St. James, Phys. Lett. 24A, 241-242 (1967).

M6 M. F. Merriam and M. Von Herzen, Phys. Rev. 131, 637-643 (1963).

O1 Orsay Group on Superconductivity, PP26-67 in Quantum Fluids ed. by Brewer, North-Holland Pub. Co., Amsterdam (1966).

O2 H. K. Onnes, Leiden Comm. 1206, 1226, 124C (1911).

P1 A. B. Pippard, Proc. Roy. Soc. (London) A191, 385-399 (1947).

P2 A. B. Pippard, Proc. Roy. Soc. A191, 370-384 (1947).

P3 A. B. Pippard, Proc. Roy. Soc. A216, 547-568 (1953).

P4 A. B. Pippard, Proc. Roy. Soc. A203, 98-118 (1950).

P5 A. B. Pippard, Proc. Roy. Soc. A191, 399-415 (1947).

P6 J. M. Pierce, H. A. Schwettman, W. M. Fairbank and P. B. Wilson, 396-399 (Part A), Proceedings of the IXth International Conf. on Low Temperature Physics, Plenum Press, New York, 1965.

P7 J. M. Pierce, J. Appl. Phys. 44, 1342-1347 (1973).

P8 C. Passow, Phys. Rev. Lett. 28, 427-431 (1972).

P9 B. Piosczyk, P. Kneisel, O. Stoltz and J. Halbritter, IEEE NS-20, 108-112 (1973).

P10 H. Pfister, Cryogenics 16, 17-24 (1976).

P11 J. M. Pierce, PhD Thesis, Stanford University, June 1967.

P12 H. Parr, Phys. Rev. B12, 4886-4898 (1975).

P13 H. Parr, Preprint, "Superconductive Superheating Field for Finite κ".

P14 H. Parr, Preprint, "Ideal Superheating and Supercooling Limits in Superconducting In and Dilute InBi Alloys".

R1 B. Rosenblum and M. Cardoma, Phys. Lett. 13, 33-34 (1964).

R2 G.E.H. Reuter and E. H. Sondheimer, Proc. Roy. Soc. A195, 336-364 (1948).

R3 M. Rabinowitz, J. Appl. Phys. 42, 88-96 (1971).

S1 L. Szécsi, Z. Physik 241, 36-44 (1971).

S2 T. P. Sheahen, Phys. Rev. 149, 368-370 (1966).

S3 H. A. Schwettman, P. B. Wilson, J. H. Pierce and W. M. Fairbank, Adv. Cryog. Eng. 10, 88-97 (1965).

S4 K. Schnitzke, H. Martens, B. Hillenbrand and H. Diepers, Phys. Lett. 45A, 241-242 (1973).

S5 H. A. Schwettman, IEEE Trans. Nucl. Sci. NS-22, 1118-1124 (1975).

S6 F. W. Smith and M. Cardona, Solid State Commun. 6, 37-43 (1968).

S7 F. W. Smith, A. Baratoff and M. Cardona, Phys. Kondens. Materie. 12, 145-192 (1970).

S8 D. Saint-James and P. G. Gennes, Phys. Lett. 7, 306-308 (1963).

S9 A. J. Sierk, C. J. Hamer and T. A. Tombrello, Part. Accel. 2, 149-167 (1971).

S10 D. Saint-James, E. J. Thomas and G. Sarma, Type II Superconductivity, Pergamon Press, New York, 1969.

T1 T. A. Tombrello and D. A. Leich, IEEE Trans. Nucl. Sc. NS-18, 164-165 (1971).

T2 J. P. Turneaure and N. T. Viet, Appl. Phys. Lett. 16, 333-335 (1970).

T3 J. P. Turneaure, PhD Thesis, Stanford University (1967).

T4 M. Tinkham, Introduction to Superconductivity, McGraw-Hill, Inc., New York, 1975.

V1 J. M. Victor and W. H. Hartwig, J. Appl. Phys. 39, 2539-2546 (1968).

V2 C. Vallete and G. Waysand, Proceedings of 14th International Conf. on Low Temperature Physics, American Elsevier Pub. Co., Inc., New York, 1975, pp. 183-186 (Vol. 2).

Y1 T. Yogi, Cryogenics 13, 369-370 (1973).

Y2 M. L. Yu, PhD Thesis, Caltech (1973).